Disorder-induced vortex phase transition in high-temperature superconductors

Dmitry Giller

Department of Physics

Ph.D. Thesis

Submitted to the Senate of Bar-Ilan University

Ramat-Gan, Israel March 2002

This work was carried out under the supervision of

Professor Yosef Yeshurun

Department of Physics, Bar-Ilan University

Acknowledgements

I would like to extend my deep and grateful thanks to *Professor Yosef Yeshurun*, who contributed greatly to the success of my work, who taught me a lot, and who supported me in all my endeavors. His concern and care were very important to me in both good and bad times.

Professor Avner Shaulov has my special thanks for his contribution of long discussions. These discussions cannot be overestimated.

I thank the *Clore Foundation*, for awarding me their prestigious scholarship.

Additional thanks are extended to the laboratory members for their cooperation: *Shuki Wolfus, Ruslan Prozorov, Yosi Abulafia, Eran Sheriff, Yael Radzyner, Beena Kalisky, Alex Friedman and Noam Shaked.*

The experimental systems worked continuously, because of the unconditional help I received from the technical staff: *Avi Szanto*, *Menahem Katz, Semion Nathliashvili, Eli Perl and Itamar Fadel.*

Thanks to *Michael Baziljevich* and *Lev Dorosinskii*, who helped me build the magneto-optic system. I thank them for numerous "tips" they gave me, which helped overcome experimental problems, which often seemed unsolvable.

I thank my collaborators both at Bar-Ilan and other institutions: *Boris and Irina Shapiro, Leonid Burlachkov, Eli Zeldov, Tom Johansen, Valerii Vinokur, Mike McElfresh, and Tsuyoshi Tamegai.*

During numerous conferences and visits, I was fortunate to have interesting conversations about physics with many people. I would like to thank those people, including *Vitalii Vlasko-Vlasov, Alex Gurevich, Vadim Geshkenbein, E. H. Brandt*, and *Alex Koshelev*.

Table of Contents

List of Figures

List of Tables

Abstract

This work describes experimental and theoretical investigations of the vortex matter in high-temperature superconductors, focusing on the vortex phase transition from a quasi-ordered lattice to a highly disordered vortex solid. Novel local magnetic techniques - miniature Hall-probe arrays and high-temporal resolution magneto-optics - were employed to characterize the equilibrium solid vortex phases, the transition between them, and the kinetics of this phase transition. We measured the temperature dependence of the vortex order-disorder transition field in different materials with different parameters, such as anisotropy, critical temperature, coherence length, penetration depth and interlayer distance. The diverse results obtained were successfully analyzed on the basis of a recent model that views this transition as driven by disorder-induced fluctuations. In analyzing the kinetics of the vortex phase transition, we developed a novel approach, based on the Landau-Khalatnikov dynamic equation.

Measurements of magnetization versus temperature, field, and time were performed in the vicinity of the second magnetization peak of $Nd_{1.85}Ce_{0.15}CuO_{4-\delta}$, detwinned $YBa_2Cu_3O_{7-\delta}$, and $Bi_{1.6}Pb_{0.4}Sr_2CaCu_2O_{8+\delta}$ to identify the order-disorder phase transition in these materials and to construct the vortex solid-solid transition line, $B_{ss}(T)$. Our measurements revealed qualitatively different temperature dependences of the vortex order-disorder transition lines, $B_{ss}(T)$, in the different materials. In interpreting these results on the basis of the disorder-induced phase transition model, we ascribed these differences to different pinning mechanisms and different material parameters. In particular, in the 3D pinning regime, δl-pinning causes B_{ss} to increase with temperature, and δT_c-pinning causes B_{ss} to decrease. A

non-monotonous behavior of B_{ss} may be caused by thermal fluctuations above the single vortex depinning temperature T_{dp}.

A high temporal resolution magneto-optical system was built and used to trace the time evolution of the vortex structure in a $Bi_2Sr_2CaCu_2O_{8+\delta}$ crystal after a sudden application of a magnetic field. For fields much smaller than the transition field B_{ss}, we were able, for the first time, to trace the whole process of formation of the equilibrium phase by imaging the process of partial flux penetration, formation of Bean profiles, and the approach to equilibrium, characterized by a dome-shape profile. For fields in the close vicinity of B_{ss}, the magneto-optical images revealed dynamic coexistence of two vortex phases: a quasi-ordered phase in the sample interior and a transient-disordered phase near the sample edges. The border between these two phases, marked by an abrupt change in the gradient of the local induction, changes its position with time. This motion enables tracing the decay of the transient state and the concurrent growth of the thermodynamic vortex phases. The growth rate at which this process evolves was found to be sensitive to the exact location in the field-temperature phase diagram.

The above results stimulated a development of a theoretical analysis, based on the Landau-Khalatnikov dynamic equation. The objectives of this analysis were to find conditions for the appearance and stability of the front, to describe the nucleation process – its location, time and spatial scales, and to describe the growth process – front velocity and front width. The Landau-Khalatnikov equation was solved analytically assuming a constant field gradient. It was shown that the ordered phase nucleates locally, and the front appears, provided the ratio between the gradient of the magnetic induction and the transition field is large enough. We also showed that reduction of the sample size should cause a crossover from a front-like to

homogeneous growth of the ordered phase. The model was solved numerically for the general case of relaxing magnetic induction. Our theoretical predictions were found to be in accordance with the experimental results. Specifically, the velocity of the interface was found to be dependent only on the value of the induction at the interface, B_f, decreasing to zero as B_f approaches B_{ss}. In addition, we succeeded in explaining the intriguing phenomenon of the dynamic "fishtail".

Our combined experimental and theoretical studies of the vortex matter near the solid-solid phase transition revealed new aspects of the vortex behavior in this region, deepening our understanding of the vortex matter and the vortex phase diagram.

I Introduction

The field of superconductivity had been considered as almost completely understood. However, after the exciting discovery of high-temperature superconductors (HTS) by Bednorz and Müller [1] and their followers [2-4], the field was opened once again. One of the most exciting developments in this reborn field is the discovery of new vortex phases, resulting in a rich phase diagram of the vortex matter.

In 1957, Abrikosov [5] predicted that above the "lower critical field", H_{c1}, magnetic field penetrates a type-II superconductor in a form of magnetic flux lines (or vortices), each carrying a quantum $\Phi_0 = h/2e$ of magnetic flux. The superconducting order parameter is suppressed in this flux line, producing an "island" of a normal state surrounded by superconducting shielding currents flowing inside a superconducting "sea." Abrikosov's calculations showed that the vortices should be arranged in a hexagonal lattice, the so-called "Abrikosov lattice," with a lattice constant $a_0 \approx (\Phi_0 / H)^{1/2}$, where H is the applied field. This prediction was later confirmed experimentally by neutron diffraction on superconducting Nb [6] and magnetic decoration [7]. However, it soon became clear that the vortex lattice structure might be disturbed in the presence of defects in the atomic lattice. These defects pin magnetic flux lines and may cause distortions in the vortex lattice. Moreover, pinning does not allow the system to reach equilibrium immediately after the application of the magnetic field, which thus causes the experimental results of various measurements to be time dependent.

In conventional, low-temperature superconductors (LTS), the Abrikosov lattice phase occupies most of the magnetic phase diagram, between the lower critical

field $H_{c1}(T)$ and the upper critical field $H_{c2}(T)$. Compared with LTS, HTS are characterized by much smaller coherence length, ξ, larger London penetration depth, λ, higher anisotropy ($1/\varepsilon$) of the electron mobility, and much higher transition temperature T_c [8, 9]. The combination of these parameters gives rise to a softer vortex structure and, consequently, to a rich field-temperature (B-T) magnetic phase diagram. This is illustrated in Figure I-1 that exhibits the vortex phase diagram for $Bi_2Sr_2CaCu_2O_{8+\delta}$ (BSCCO), which is deduced from small angle neutron scattering experiments (SANS) [10] and magnetic measurements [11]. SANS experiments reveal pronounced Bragg peaks at low fields and temperatures, signifying the presence of an ordered (or quasi-ordered) vortex phase. These peaks disappear as the field or temperature is raised above some characteristic value, signifying the disordering of the vortex structure.

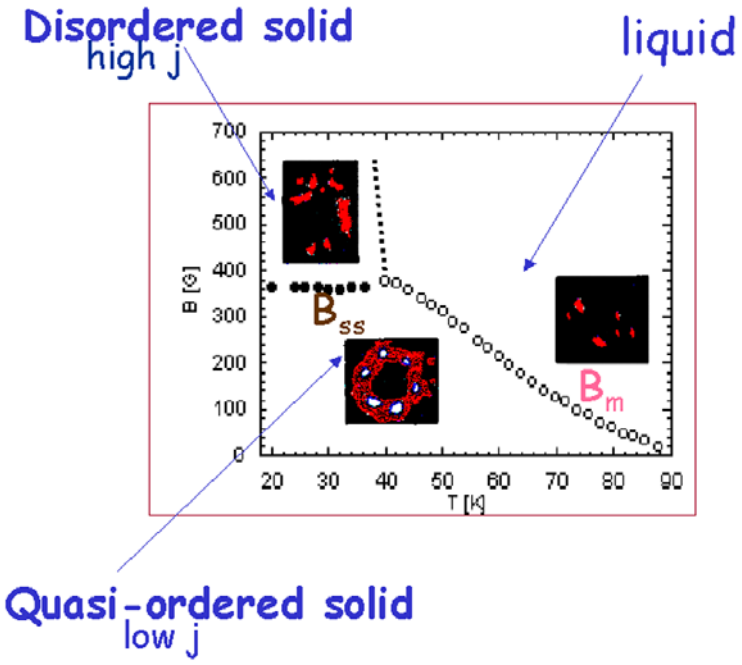

Figure I-1. Phase diagram of the vortex matter in BSCCO, based on Ref. [11]. Insets: SANS data from Ref. [10].

This disordering is manifested in magnetic measurements as (a) either a sharp anomalous increase (referred to as the "second peak" or "fishtail") in the width of the

magnetic hysteresis loop at lower temperatures (Figure I-2) or (b) a sharp step in the reversible magnetization at higher temperatures. The line $B_{ss}(T)$ was interpreted as a vortex solid-solid transition line, separating between a quasi-ordered lattice (or Bragg Glass) and a disordered solid (or glass). The line $B_m(T)$ at high temperatures was interpreted as a melting line, separating between a vortex lattice and a vortex liquid state. Solid-liquid transitions, identified by a step in the reversible magnetization, were also measured in other HTS materials, for example, in YBCO [12]. The first order nature of this transition was established from specific heat data [13]. In contrast, no signs were obtained for a solid-solid phase transition in specific heat measurements. Following these observations, theoretical models were developed [14-19]. These models ascribe the solid-liquid transition to thermal fluctuations and the solid-solid transition to the disordered-induced fluctuations.

Although the vortex phase diagram in BSCCO (Figure I-1) is established, it remained unclear whether other HTS systems exhibit a similar vortex phase diagram and phase transitions. In this thesis, we address this issue comprehensively, focusing on the vortex phase diagram in the field and temperature range of the fishtail.

A fishtail, or a second magnetization peak, was observed in a variety of HTS crystals, such as $YBa_2Cu_3O_{7-\delta}$ (YBCO) [20-22], $(La_{1-x}Sr_x)_2CuO_4$ (LSCO) [23], Tl-based compounds [24, 25], and Hg-based compounds (HBCO) [26], and also in LTS crystals, such as $CeRu_2$ [27] and $NbSe_2$ [28]. However, in these materials the onset of the second peak was not as sharp as in BSCCO. In addition, the second peak in these materials was much broader and appeared in different field ranges. Thus, in materials other than BSCCO, the association of the second peak with a vortex solid-solid phase transition was questionable.

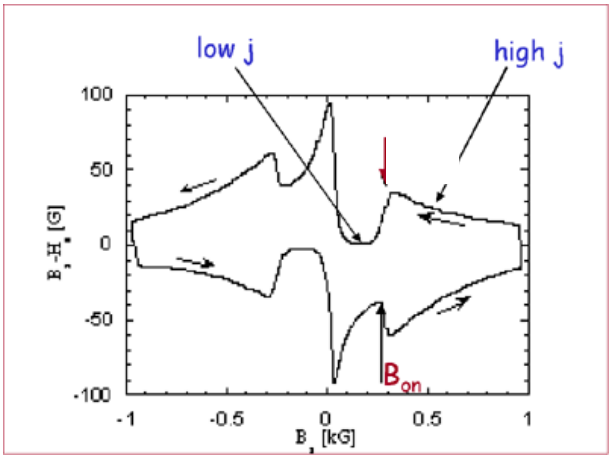

Figure I-2. Local magnetic hysteresis loop measured in BSCCO [11] using miniature Hall probe. The fishtail onset field B_{on}, separating low-*j* and high-*j* regions, is associated with the solid-solid transition field B_{ss}.

Different mechanisms, for example, inhomogeneity of the sample ([20, 21]), matching effects [29], surface barriers [24], geometrical effects [23], dynamic effects [22, 30], structural phase transition in the vortex lattice [31], and vortex decoupling [32], were invoked as possible mechanisms for the appearance of the second peak in different materials.

In this thesis, we present new data in $Nd_{1.85}Ce_{0.15}CuO_{4-\delta}$, detwinned $YBa_2Cu_3O_7$, and $Bi_{1.6}Pb_{0.4}Sr_2CaCu_2O_{8+\delta}$ and demonstrate that the fishtail in these materials can be associated well with a solid-solid phase transition, as in $Bi_2Sr_2CaCu_2O_{8+\delta}$ [16, 17]. We find, in these systems, markedly different temperature dependence of B_{ss} and succeed in quantitatively explaining these behaviors in the framework of the disorder-induced transition model developed by Ertas and Nelson [15] and Vinokur *et al.* [16].

Another major topic of this thesis concerns the process of formation of the solid vortex phases. The thesis describes a pioneering work, in which the nucleation and growth of the vortex solid phases in BSCCO are revealed and studied, both

experimentally and theoretically. These results also shed light on the nature of the solid phases and the transition between them.

In our experimental studies, we utilized unique local magnetic methods (namely, miniature Hall-probe arrays [32-38] and magneto-optics [39-45]) to image the magnetic induction on a specimen surface with spatial resolution on the order of micrometers and time resolution on the order of 40 milliseconds. The use of these methods is of special advantage for measurements performed in the irreversible state of superconductors in which the magnetic induction is highly non-homogeneous.

This thesis is organized as follows. In the next Chapter, we describe the Hall-probe array [46] and magneto-optic setups; the latter was specially designed and built as a part of this thesis. In Chapter III we describe a study of the vortex solid-solid transition in different superconducting crystals ($Nd_{1.85}Ce_{0.15}CuO_{4-\delta}$, detwinned $YBa_2Cu_3O_{7-\delta}$ and $Bi_{1.6}Pb_{0.4}Sr_2CaCu_2O_{8+\delta}$), using the Hall-Probe array system. We explain the markedly different transition lines obtained in these materials in the framework of the disorder-induced transition model [15, 16]. The main results of this chapter were published in Refs. DG3, DG4, DG8, DG10, DG13, DG14, DG17, listed in the Appendix. Our pioneering work on the process of the nucleation and growth of the vortex solid phases is described in Chapter IV. The main results of this Chapter were published in Refs. DG12, DG15, DG18, DG19. In Chapter V we analyze the experimental results of Chapter IV, employing the Landau-Khalatnikov dynamic equation. The main results of this chapter were published in Ref. DG20. Chapter VI summarizes the main achievements of this work and suggests directions for future experiments. The appendix lists the publications emanated from this work.

II Experimental

Magnetic measurements can be classified into three major categories: global, local, and microscopic. Global techniques characterize the sample as a whole, yielding information on physical quantities averaged over the sample volume. In many cases, this information is not enough to characterize the state of the superconductor sufficiently. In particular, the information obtained in such measurements is incomplete in the irreversible regime, in which the magnetic induction inside the superconducting sample is non-uniform [47-50]. Similarly, such measurements are unable to reveal or characterize a coexistence of two different phases in a sample (as we do in Chapter IV using a *local* magneto-optic technique).

Microscopic measurements, such as scanning tunneling microscopy or magnetic force magnetometry, are used for the study of individual vortices, but these measurements may not provide sufficient information about the vortex order on sufficiently large spatial scales. Moreover, these techniques mostly require ideal work conditions, which often cannot be provided when working with various materials.

Local magnetic techniques are most suitable - in terms of their spatial and time resolution - for the experiments described in this thesis. In this research, we utilize two complementary local magnetic measurement techniques: Micro-Hall-probes array (HPA) and magneto-optics (MO). HPAs manufactured by E. Zeldov at the Weizmann Institute were incorporated in a system built at our laboratory by Y. Abulafia [46]. A high-temporal resolution MO system was designed and built as a part of this thesis. In the following sections, we elaborate on each of these techniques.

II.1 Hall-probes array (HPA)

The first step in overcoming the limitations of global magnetic measurements was taken in the early 1990s, when miniature single Hall-probes made of InSb were used [33, 51-53]. In addition, single probes of Bi films [35] GaAs/AlGaAs [34, 54, 55] and doped GaAs [32] as well as arrays of doped GaAs sensors [56] were used in static and scanning modes. The technique was improved substantially by E. Zeldov *et al.*, who developed (at the Weizmann Institute) arrays of Hall sensors based on the properties of a two-dimensional electron gas (2DEG) formed at a hetero-interface of GaAs/AlGaAs [57-59]. The GaAs 2DEG has a mobility of about 10^5 cm^2/V sec at 80 K and a carrier concentration of about 6.25 x 10^{11} cm^{-2}, resulting in sensitivity of about 0.1Ω/G. These sensors have the advantage of a quick response to the magnetic field, large field and temperature working ranges, weak temperature dependence, and high sensitivity. The sensors are manufactured using well-established photolithographic and etching techniques. Figure II-1 shows a photograph of the Hall-probe array, manufactured at the Weizmann Institute.

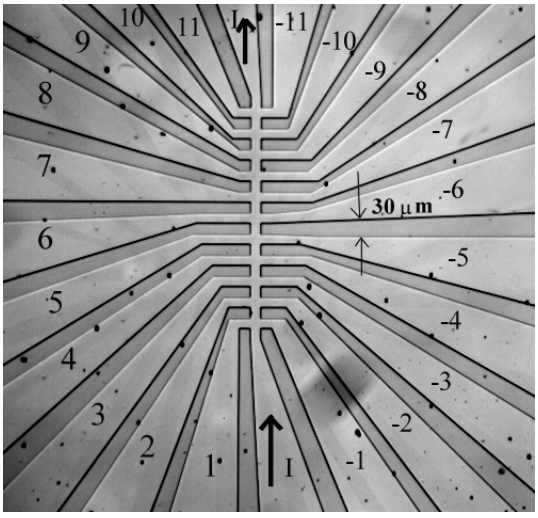

Figure II-1. A photograph of the 11-element Hall-probe array, manufactured at the Weizmann Institute. The vertical line is a current channel; 11 horizontal lines are channels for Hall-voltage measurement.

Figure II-2 shows a schematic configuration of a Hall-probes array mounted on a sample. In practice, the sample is adhered to the surface of the GaAs using a low-melting-temperature wax. The sensors measure the component of the magnetic induction perpendicular to the sample surface.

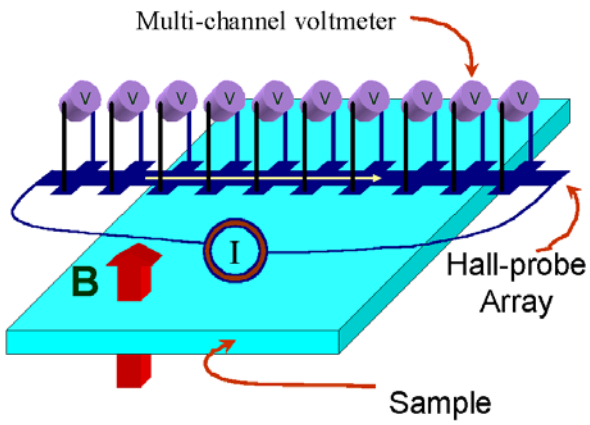

Figure II-2. Schematic description of the micro Hall-probe array experiment.

A photograph of a superconducting sample glued on an array is shown in Figure II-3.

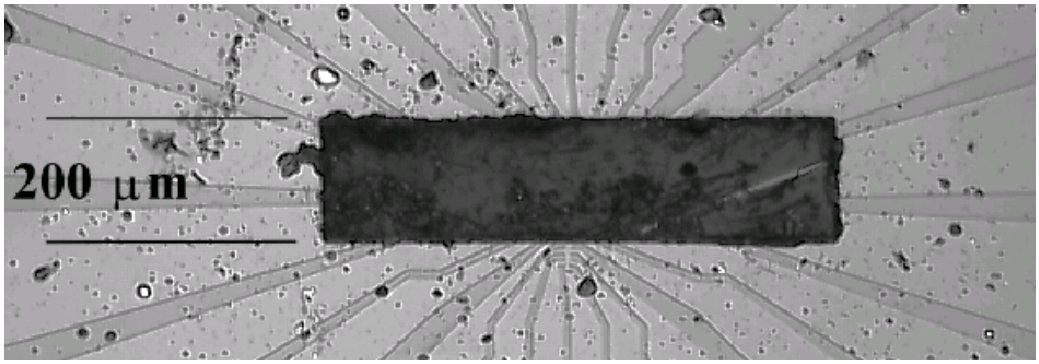

Figure II-3. Photograph of a superconducting sample glued on an array.

Figure II-4 shows a block-diagram of the system constructed by Y. Abulafia in our laboratory [46]. This system was used for the measurements presented in Chapter III. The field range of the measurements is –6.5 to 6.5 T. The temperature range is 4 K to 300 K. The time-resolution (in the mode in which all probes are active) is about 30 s. The basic software was written by M. Katz and modified by Y. Abulafia and D.

Giller to support advanced modes of measurements. For an extensive description of this system see Ref. [46].

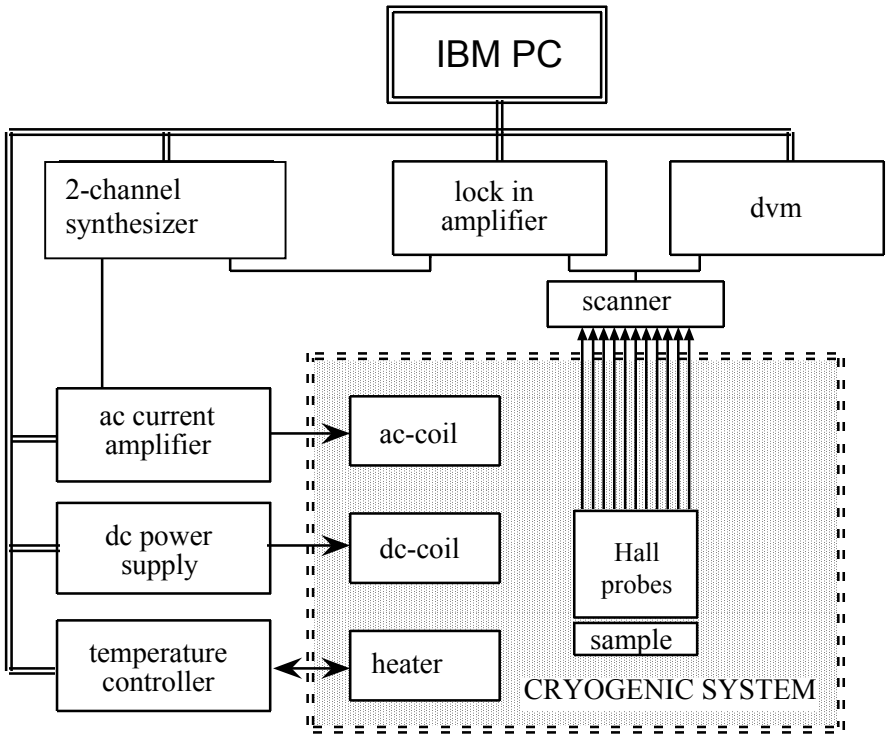

Figure II-4. Block diagram of the Hall-probe array setup (from [46]).

Hall-probe arrays allow direct detection of the magnetic induction distribution within a superconductor. Utilization of these miniature Hall-probe arrays enables a direct, model-independent derivation of some of the fundamental physical parameters of HTS, such as the position and time dependence of the apparent current ***j****(x,t)*, the magnetic induction *vector* ***B*****,** the position and time dependence of the electric field ***E****(x,t)*, flux-line velocity ***v****(x,t)*, and the position and time dependence of the effective activation energy *U(x,t)*. [36, 38, 60, 61].

II.2 Magneto-optic (MO) technique

II.2.1 MO indicators

Magneto-optical method for local measurements of magnetic induction on the surface of superconductor [62, 63] was introduced in early 1960s [64]. This method

utilized the Faraday effect - the ability of certain transparent materials to rotate the polarization plane of the light passing through them in the presence of a magnetic field. The angle of rotation is proportional to a component of local magnetic induction B_z, parallel to a direction of light propagation:

$$\alpha_F = VB_z d \tag{2.1}$$

where V is Verdet constant (a material property), and d is a length of light-path in the material. Such materials are called magneto-optically active.

In the early magneto-optic experiments, thin (0.1 – 0.2 μm thick) magneto-optically active EuS or EuF_2 films were used. These materials have large Verdet constants (i.e., high sensitivity) only at temperatures as low as 10-15 K, thus allowing measurements only of conventional superconductors. In addition, these films must be deposited in a vacuum directly on a top surface of the superconductor, which is a complicated technique that often produces irregular indicator film properties.

A breakthrough in advancing the magneto-optic characterization was achieved in 1989, when Bi-substituted ferrimagnetic iron garnet thin films were suggested for indicator layers [65]. The main advantage of this material is a very large Verdet constant (several orders of magnitude larger than previous indicators), which persists up to very high temperatures (> 500 K). However, the resolution of such films with out-of-plane magnetization is limited by the width (2-10 μm) of the labyrinthine domains. Later, the spatial resolution and the sensitivity of this technique was significantly improved by the use of ferrimagnetic garnet films with in-plane anisotropy. Figure II-5 shows the geometry of using such an iron-garnet film for magnetic flux visualization. Polarized light arriving normally to the surface first passes through a transparent substrate, and then enters also transparent magneto-

optically active layer. In this layer, the component of the local induction is $B_z = 4\pi M_z(H) + H_z$, where M_Z is a magnetization of the indicator film induced by the external magnetic field H_z. In turn, H_z is a field induced inside the indicator by the presence of a measured superconductor. The induction B_z causes the polarization plane of light to rotate according to equation (2.1). The light is then reflected from a thin gold or aluminium layer on the bottom of the indicator and experiences additional polarization rotation.

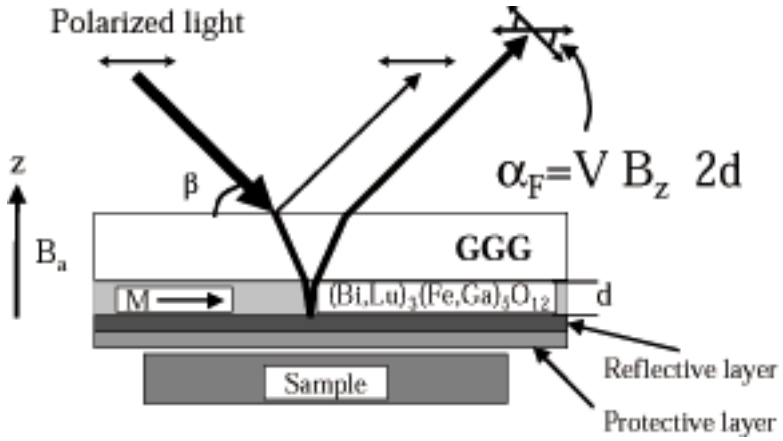

Figure II-5. Diagram of in-plane indicator film geometry [62].

The experimental setup for detecting the local distribution of the magnetic induction that we built is presented in Figure II-6.

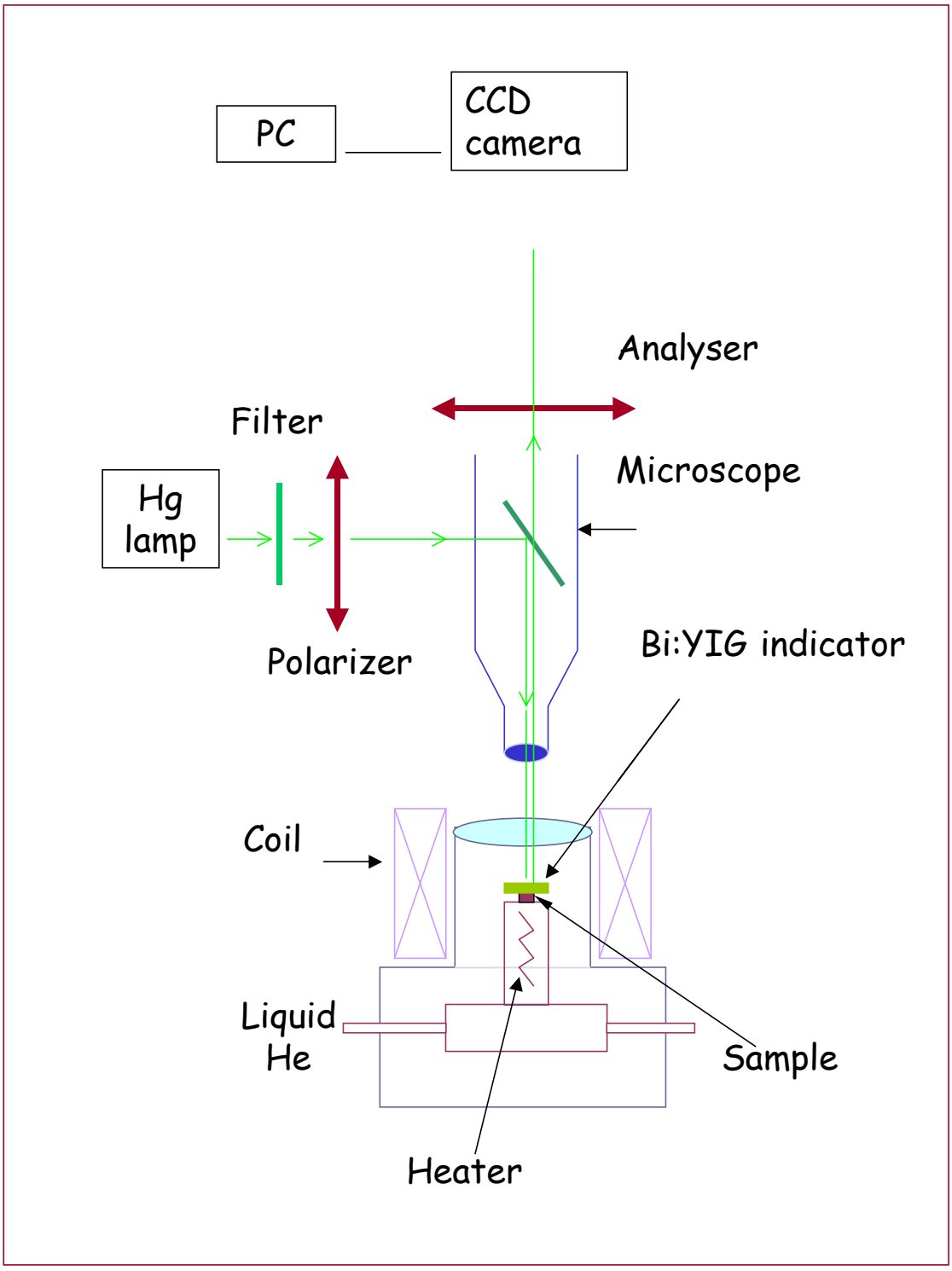

Figure II-6. Experimental setup for the magneto-optical system (adapted from Ref. [66]).

This setup includes a "Leica" polarizing microscope, in which low-strain objectives x2.5, x5 and x10 for polarized light are installed and in which it is possible

to switch between the magnifications. Polarizer and a 360°-rotating analyzer are parts of this microscope as well. The magneto-optic indicator (specially purchased in Russia) is lying on the superconducting sample glued on the cold finger of a helium-flow cryostat. The temperature is controlled using a resistive heater and AlGaAs-diode temperature sensor, connected to a "Lakeshore-330" temperature controller. The magnetic field is produced by a "*Lip*-LPS-2306D" (dual 0-30V, 0-6A) power supply in a coil lying on the cryostat, around a pillar in a manner such that the sample is located exactly in the middle of the coil. This assures maximal homogeneity of the applied field. The light generated by a halogen/mercury lamp passes through a green filter[1] to avoid dispersion of the indicator response. The light then meets a polarizer, where the light obtains linear polarization. After being converged by one of the special low-strain microscope objectives (x2.5, x5, x10) designed for work with polarized light, the light enters the cryostat through a low-strain quartz window of the cryostat. Then, while passing through the indicator film, the polarization of the light is rotated *locally* as a function of the local magnetic induction. After being reflected from the reflective layer on the bottom of the indicator, the light exits the cryostat and passes through the analyzer, about 90° angled relative to the polarizer. The resulting image arrives at a cooled low-noise "Hamamatsu 4880-80" digital CCD camera transferring the digital images to a PC. This camera is capable of capturing 25 full (656 x 494) frames per second. The distance between neighboring pixels in the resulting image is defined by the objective magnification and is 1.98 μm for the largest magnification of x10. This, however, usually does not limit the overall

[1] The MO activity *vs.* wavelength curve has a peak in the vicinity of 530 nm.

resolution of the system, which is limited mostly by the finite thickness of the indicator (up to 5 μm thick).

The exposure time is regulated by an electronic shutter and varies from as low as 0.1 ms to as high as several minutes, thus allowing imaging of both a rapidly changing scene and a static, low-illuminated scene.

A typical magneto-optical image obtained using an in-plane anisotropy indicator is shown in Figure II-7.

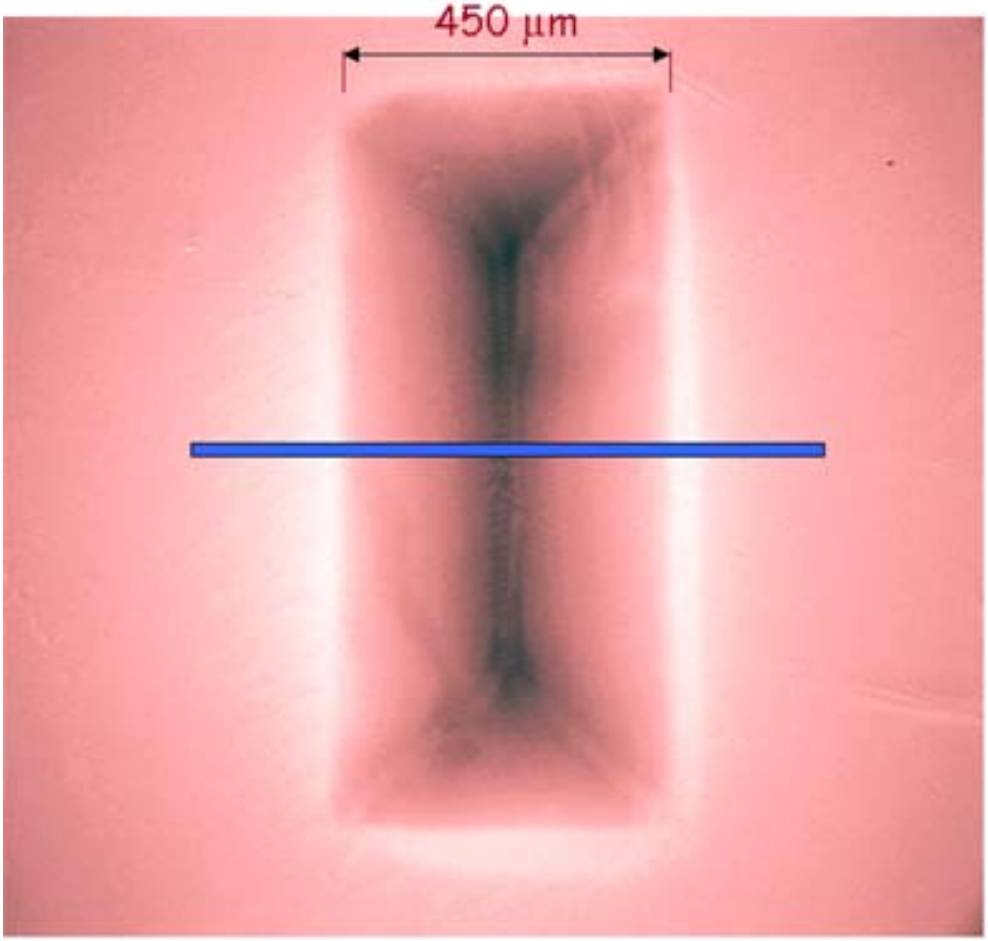

Figure II-7. Magneto-optic image of BSCCO thin strip 0.2 s after application of an external magnetic field of 350 Oe. Brighter and darker areas correspond to higher and lower induction, respectively. One-dimensional profiles are taken along the drawn horizontal line.

The teeth-like magnetic domain walls seen in the middle of the indicator disturb the image. The larger the sample, the less disturbed are the domain walls. Our

setup allows measurements in magnetic fields of up to approximately 300 Oe without time limit (the coil is not heated up), 500 Oe up to 2 min, 1000 Oe up to 20 sec. It supports either time-resolved (minimum of 40 ms time resolution) or static measurements with varying fields or temperatures.

II.2.2 Data processing

Images obtained from the CCD camera are, of course, not calibrated, and truly reflect the variation in polarization of the incoming light. The calibration curve depends on magneto-optic parameters (Verdet constant and $M(H)$ curve) of the specific indicator at the specific temperature.

In our measurement protocol, a calibration procedure is performed before each set of measurements. It includes capturing (a) a "dark" image (*DI*), which is taken when the aperture of the camera is covered; (b) zero-field image (*ZFI*), taken after zero-field cooling the sample (*DI* and *ZFI* are usually averaged from approximately 100 frames captured, one after another, to minimize noise induced by calibration); and (c) a sequence of images taken after the applied field is activated and raised gradually with small steps, while capturing images at any applied field value. A table of calibration is then prepared, based on the intensity measured at a point p located far away from the sample, assuming that the value of the magnetic field (H_z) at this point equals the value of the external field. (In practice, the intensity at p is averaged over $n \times n$ pixels (usually $n = 3$)). We define a calibration curve F:

$$F = \frac{I_p(H_z) - ZFI_p}{ZFI_p - DI_p}, \tag{2.2}$$

where $I_p(H_z)$ is the measured intensity when the field is H_z, and $ZFI_p = I_p(H_z=0)$. The denominator in Eq. (2.2) is expected to be proportional to the illumination intensity Il_p at the point p. If the magneto-optical activity $A(H_z)$ is uniform across the indicator

film, then the numerator in Eq. (2.2) is proportional to $A(H_z)Il_p$. We thus obtain from Eq. (2.2) that $F \propto A(H_z)$, leading to the conclusion that F is defined unequivocally by the local magnetic field H_z. Any measured image can now be translated to a 2D H_z distribution. This is done in two steps. First, the measured intensity distribution is converted to a F-distribution: $F = (I - ZFI)/(ZFI - DI)$. Then, the F-image is converted to a H_z-image by using the $F(H_z)$ table defined by (2.2).

II.3 Geometry of samples

In all the experiments described in this thesis, the samples measured had a thin strip geometry ($t << d << l$) as in Figure II-8.

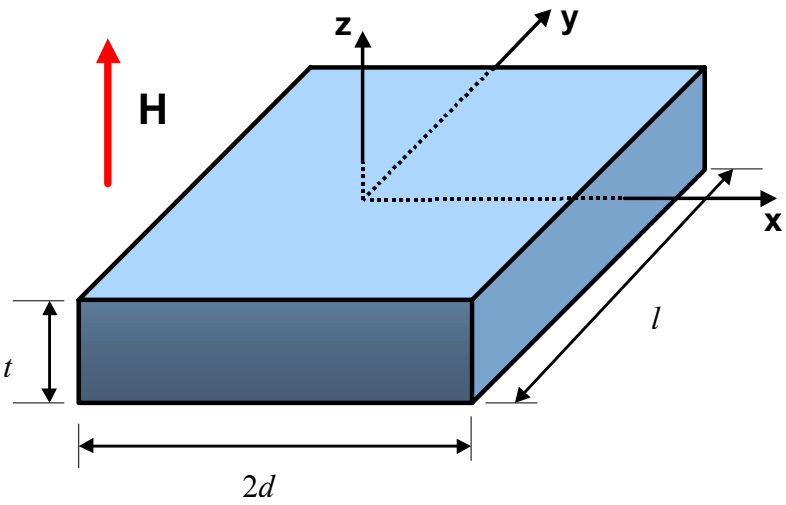

Figure II-8. Sketch of a thin strip geometry used in this research.

This geometry has the advantage of the possibility of making relatively simple and comprehensive analyses, based on one-dimensional profiles only, taken across the sample width. In our analyses, we assume that the persistent current density j, together with the electric field E, have only y-components, which are uniform across the z-dimension.

III Disorder-induced vortex phase transition

The width of the magnetic hysteresis loop is expected to decrease with the external field (for fields larger than the full penetration field) [67]. Such "normal" loops are usually observed in samples, that have many intrinsic defects, for example, thin films and polycrystalline materials. An anomalous behavior in the magnetization curve was reported in crystals of various materials (see Chapter I). In these materials, the width of the magnetization loop first decreases as expected. Then, at some field B_{on}, the width starts to increase up to a field B_p and decreases again above this field. This anomaly was called a "second peak" or, because of its shape, a "fishtail." This fishtail has different characteristics in different materials. For example, in $YBa_2Cu_3O_{7-\delta}$ the peak is broad and appears in the Tesla range, whereas in $Bi_2Sr_2CaCu_2O_{8+\delta}$ the peak is sharp and is found in the range of hundreds Gauss.

During the last decade, several explanations for this anomaly were proposed [20-24, 29-32]. However, the observed different characteristics questioned the possibility of a common physical origin for different HTS materials.

Experimental observations of an extremely sharp second peak in BSCCO [11, 68] motivated a new approach, suggesting that the fishtail is associated with a vortex phase transition from quasi-ordered to a disordered solid vortex state. Indeed, evidence for two distinct solid vortex phases in BSCCO was obtained in neutron diffraction [10] and μSR [69] experiments. Following these observations, a theoretical model was developed [14-19] describing a mechanism for a disordered induced transition.

The essence of this model is that the vortex phase diagram is determined by the interplay among three energy scales: the vortex elastic energy E_{el}, the energy of

thermal fluctuations E_{th}, and the pinning energy E_{pin}. The competition between the first two determines the melting [57], and the competition between the last two determines the irreversibility line. The competition between the elastic energy and the pinning energy determines the order-disorder solid-solid transition field B_{ss}: At low fields the elastic interactions govern the structure of the vortex solid, forming a quasi-ordered lattice [19]. Above B_{ss}, however, disorder dominates and vortex interactions with pinning centers result in an entangled solid in which cells of the vortex lattice are twisted and dislocations proliferate. [14-19]

This disorder-induced transition model was successfully applied in Refs. [16, 70] to explain the temperature-independent solid-solid transition line in BSCCO and its value at zero-temperature. In this chapter we present results of local magnetization measurements in variety of high-temperature superconducting crystals as a function of temperature, field and time. We exploit these measurements for the identification of the vortex solid-solid phase transition in these crystals. We find that the transition field exhibits qualitatively different temperature dependence in different materials. We show, however, that despite these differences, the behavior of the transition field can be explained *quantitatively* on the basis of the disorder-induced transition model mentioned above.

This Chapter is organized as follows. In Section III.2 we present the raw data of Hall-probe array measurements in different HTS crystals, identify the phase-transition field, and plot the transition line $B_{ss}(T)$ in the B-T phase diagram. In Section III.2 we analyze these data on the basis of the *disorder-induced transition* model and demonstrate that the different behaviors of the transition lines are associated with the different characteristics of vortex-pinning and vortex-vortex interactions in the various crystals.

III.1 Identification of vortex phase transitions in different materials

In this section we present results of local magnetization *vs* field (*m vs. H*), magnetization *vs.* temperature (*m vs. T*), and magnetization *vs.* time (*m vs. t*) for three different HTS materials. Table III-1 lists these materials and summarizes their properties. For comparison, we also include the properties of BSCCO.

	T_c, K	ε	s, nm	ξ, nm	λ, nm
$Bi_2Sr_2CaCu_2O_{8+\delta}$	90	~1/100	1.5	2-4	140-200
$Nd_{1.85}Ce_{0.15}CuO_{4-\delta}$	23	~1/30	0.6	8	100
$YBa_2Cu_3O_{7-\delta}$	93	1/12	1.2	1.2 – 1.8	140
$Bi_{1.6}Pb_{0.4}Sr_2CaCu_2O_{8+\delta}$	95	1/68	1.54	1 - 10	100-200

Table III-1. Critical temperature T_c, anisotropy ε, interlayer distance *s*, coherence length ξ, and London penetration depth λ, for $Bi_2Sr_2CaCu_2O_{8+\delta}$, $Nd_{1.85}Ce_{0.15}CuO_4$, $YBa_2Cu_3O_{7-\delta}$, and $Bi_{1.6}Pb_{0.4}Sr_2CaCu_2O_{8+\delta}$.

The results presented below indicate a vortex solid-solid phase transition in all these materials. We identify the phase transition field and measure its temperature dependence. The results reveal markedly different behaviors.

III.1.1 $Nd_{1.85}Ce_{0.15}CuO_{4-\delta}$

The first material studied was $Nd_{1.85}Ce_{0.15}CuO_{4-\delta}$ (NCCO), a layered HTS with a relatively large anisotropy (ε ~ 1/30 [71, 72]), but which has, however, a relatively low transition temperature (T_c ~ 23 K). As we see below, this choice ensured a lack of thermal fluctuations interference. Thus, if the second peak is due to a disorder-induced transition, it must be determined by a pure competition between elastic and pinning energy in this material.

III.1.1.1 Local magnetization curves in NCCO

Figure III-1 displays three typical local magnetization hysteresis loops measured by HPA technique (see Chapter II) at different temperatures. As expected, the width of the loops decreases with temperature. As clearly observed, the onset of the second peak at H_{on} is a decreasing function of temperature.

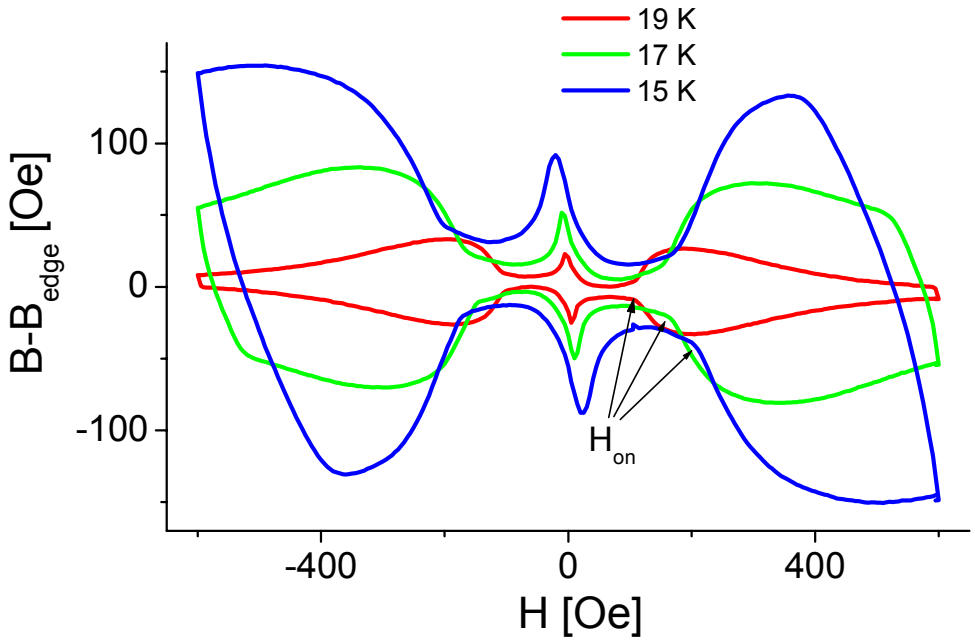

Figure III-1. Local magnetization *vs* applied (external) field *H* in NCCO at the indicated temperatures. The onset fields H_{on} are marked with arrows.

The onset of the second magnetization peak at H_{on} for NCCO (marked by arrows in Figure III-1) is almost as sharp as in BSCCO (see Figure I-2) and occurs at the *same* induction field *B* ([2]) for all the probes. This is illustrated in Figure III-2, which shows partial magnetization curves measured at different locations on the sample surface.

[2] Here, and further in this work, the "induction *B*" refers to the component of *B* normal to the sample surface, as detected by our local magnetization techniques.

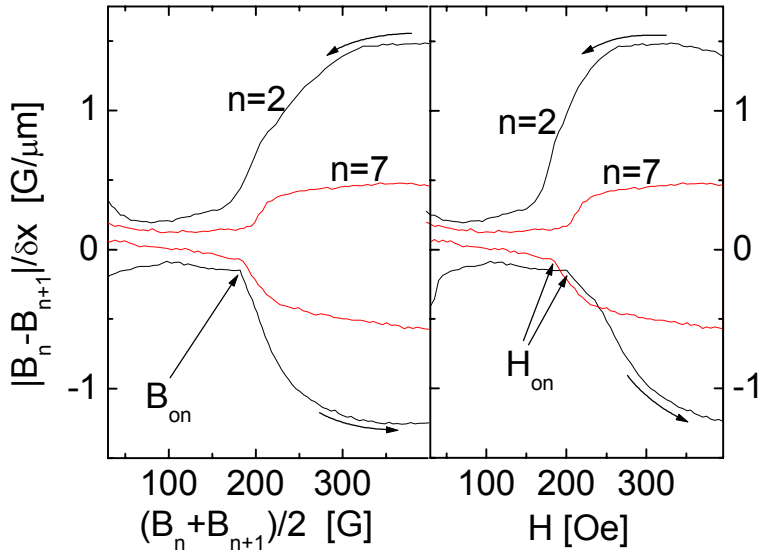

Figure III-2. Comparison between local gradient dependence on local induction (left-hand plot) and external magnetic field (right-hand plot) for two locations on the sample surface (T = 16 K). The onset of the second peak occurs at the same local induction, but at different external fields.

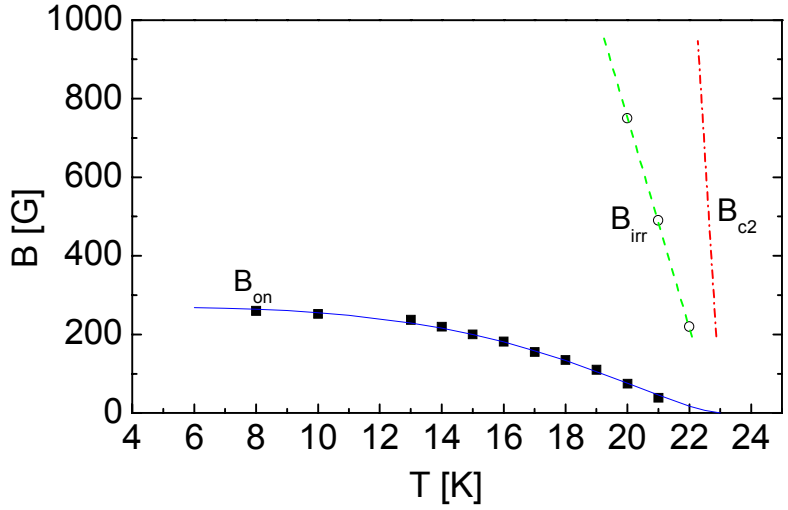

Figure III-3. Temperature dependence of the onset of the second peak B_{on} (squares) and the irreversible field B_{irr} (circles). The dashed line is a guide to the eye. The solid line is a fit of the experimental data as discussed in section III.2.2. The dotted line illustrates the upper critical field B_{c2}.

Figure III-2 exhibits *dB/dx vs. B* (left), and *dB/dx vs* external magnetic field *H*. The onset of the second peak occurs at B_{on} =180 G for all the probes.

The squares in Figure III-3 describe the temperature dependence of B_{on}. Note that B_{on} is a continuous function of temperature all the way up to T_c – 1.5 K, above which the anomaly is difficult to resolve. Also shown in Figure III-3 is the irreversibility field B_{irr} (circles), measured as the field, above which the ascending and descending branches of the hysteresis loop coincide. There is no indication in our data for a "jump" of the magnetization in the reversible state - a jump that would indicate a first-order melting transition [57]. In the following, we show that B_{on} also marks a change in the magnetic induction profiles. We also show a crossover in the creep mechanism around the fishtail peak.

III.1.1.2 Induction profiles

Figure III-4 shows typical magnetic induction profiles measured at 16 *K*.

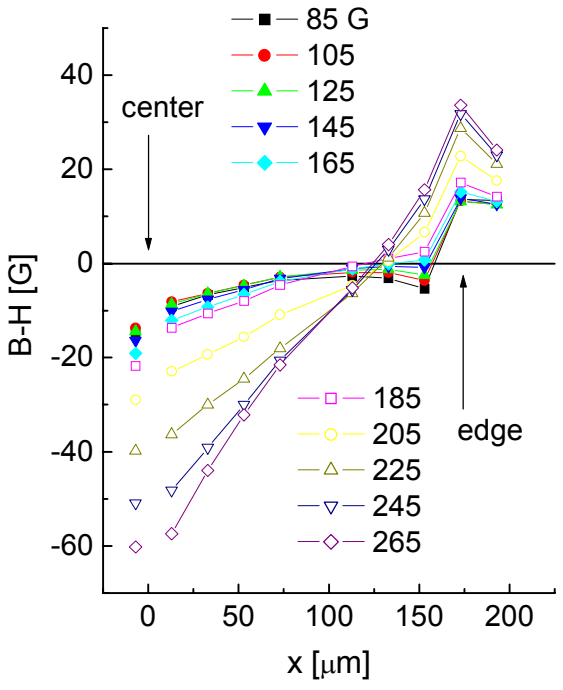

Figure III-4. Typical induction profiles at 16 K across the NCCO sample for indicated fields *H*. For inductions in the bulk below $B_{on} \approx 180$ G, the profiles exhibit a maximum (around 120 μm) typical of surface and geometrical barriers in presence of weak bulk pinning. For inductions above B_{on}, the profiles are Bean-like with much larger gradients, indicating the onset of strong pinning.

For fields below B_{on} the profiles have a shape characteristic of geometrical barriers with weak bulk pinning [73], exhibiting maxima around 120 μm from the center. For fields above B_{on}, the profiles are Bean-like with much larger gradients, indicating the onset of strong pinning. The figure demonstrates that a small change, < 20 G around 200 G causes the transition between the two types of profiles.

III.1.1.3 Local relaxation measurements in NCCO

To complete the picture in NCCO, we performed local magnetic relaxation measurements, from which we were able to determine a creep mechanism, utilizing the technique described in Refs. [36, 38, 60] for calculation of the activation energy U as a function of electric current density j for various fields. The analysis is based on the calculation of the electric field E [36, 38, 60, 61], using the Maxwell equation:

$$E_y(x,t) = -\frac{1}{c}\int_0^x \frac{\partial B_z(\xi,t)}{\partial t} d\xi \qquad \text{(III.1)}$$

where c is the velocity of light, assuming infinitely long strip geometry (see section II.3). The electric field is induced by flux motion. Flux velocity is determined from:

$$\vec{E} = \frac{1}{c}\vec{v} \times \vec{B} \qquad \text{(III.2)}$$

For a thermally activated creep

$$v = v_0 \exp\left(-U / kT\right) \qquad \text{(III.3)}$$

where U is the activation energy, and the velocity v_0 corresponds to the flux-flow equation [36]:

$$v_0 = -A\frac{\Phi_0}{c\eta} j \qquad \text{(III.4)}$$

where A is constant of order 1, and η is Bardeen-Stephen viscosity[3]. Finally one gets a relation between activation energy U and current density j:

$$U = -kT \ln\left(\frac{c\eta E}{\Phi_0 ABj}\right) \qquad \text{(III.5)}$$

Typical results are shown in Figure III-5 for T=13 K. The figure demonstrates a clear crossover in the slope of $U(j)$ around $B \approx 900$ G.

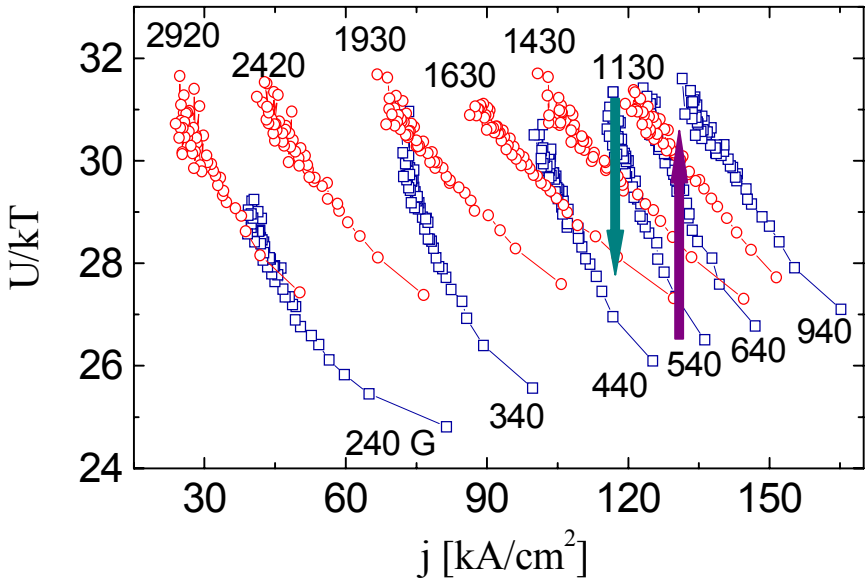

Figure III-5. Activation energy *U* for flux creep as a function of current density *j* at *T*=13 *K*, for various fields. The squares and the circles refer to fields below and above the peak, respectively. A crossover in the slope of *U*(*j*) near *B*=900 G is evident. The right arrow indicates the increase of *U* as *B* increases from 540 to 640 and 940 G. The left arrow indicates the decrease of *U* as *B* increases from 1130 to 1430 and 1630 G.

It further demonstrates a non-monotonous dependence of U on B; U increases with B for fields below 900 G and decreases with B above this field, as indicated by the right

[3] $\eta = \frac{H_{c2}\Phi_0}{\rho_n c^2}$, where ρ_n is a normal state resistivity. The calculated value of η for NCCO at T

and left vertical arrows in Figure III-5, respectively. Although the increase of U with B is consistent with elastic creep, the decrease of U with B is evidence of plastic vortex creep associated with the motion of dislocations in the vortex lattice [74]. It should be noted that, although dislocations may start to form immediately above $B_{on} \approx$ 200 G, plastic creep cannot dominate the dynamics until the activation energy U_{pl} for plastic creep drops below the activation energy U_{el}, for the collective (elastic) creep. In the case shown in Figure III-5, this crossover occurs around B = 900 G.

Appearance of dislocations at high fields indicates that the nature of the high-field phase is disordered; therefore, one may conclude that an order-disorder phase transition occurs at B_{on}.

III.1.1.4 Local magnetization *vs.* temperature measurements in NCCO

The scenario of a vortex phase transition was further examined by measurements of magnetization *vs.* temperature. If the second peak is a dynamic phenomenon, resulting from a competition between a decreasing $j_c(B)$ and increasing $U_c(B)$ ([4]) [22], then no feature in $m(T)$ is expected in the framework of the collective creep theory, because both $j_c(T)$ and $U_c(T)$ are decreasing functions of T. If, on the other hand, the "fishtail" originates from a transition corresponding to a definite value of magnetic induction at any temperature, then some feature corresponding to this transition must be observed in a temperature sweep as well when crossing a transition line.

= 13 K is $3.5 \cdot 10^{-9} \frac{g}{\sec \cdot cm}$.

[4] In the collective creep theory: $U = U_c(B) f(j/j_c)$.

In the following, we compare the results of two kinds of magnetic measurements: $m_T(H)$, in which the local magnetization is measured *vs* H at constant temperature (examples of results of such measurements are shown in Figure III-1 and Figure III-2), and $m_H(T)$, in which the local magnetization is measured *vs* T at constant field. Figure III-6 shows typical $m_H(T)$ data for NCCO.

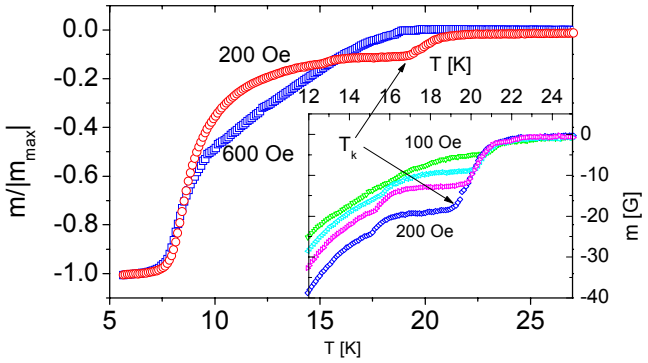

Figure III-6. Magnetization *vs.* temperature ($m_H(T)$) curves for external fields H = 600 Oe and H = 200 Oe, obtained after zero-field cooling. For fields $H > B_{on}(0)$ = 270 Oe, no special feature is observed, and for $H < B_{on}(0)$ sharp kink at T_k is found. Inset: development of the kink in $m_H(T)$ curves (H = 200, 175, 150, and 100 Oe) for different $H < B_{on}(0)$.

In Figure III-6 we exhibit several curves at the indicated fields. Note the abrupt increase in the local magnetization at field-dependent temperatures $T_k(B)$, which are marked by arrows. These anomalies are observed in a limited field range: H < 270 Oe for NCCO. The temperatures $T_k(B)$ are plotted (note that $B \sim H$ in the range of T_k - in any event, the difference between B and H cannot explain the shown phenomenon) in Figure III-7 (open symbols), together with $B_{on}(T)$. Apparently, these lines are markedly different for NCCO and, yet, we maintain that the discrepancy between these lines is not inconsistent with the transition scenario, as we explain below.

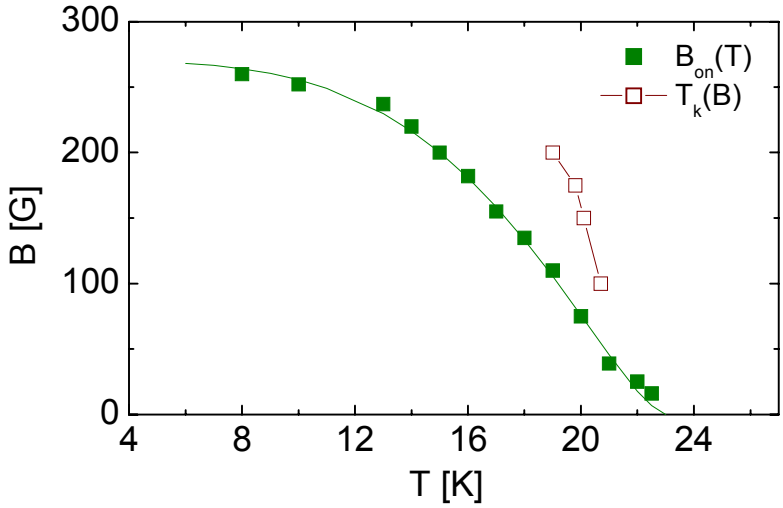

Figure III-7. $B_{on}(T)$ and $T_k(B)$ curves in the phase diagram of NCCO.

In NCCO, B_{on} decreases with temperature. Thus, crossing the $B_{on}(T)$ line by raising the temperature at a constant field corresponds to a phase transition from a quasi-ordered state with low persistent current, to a disordered vortex state with relatively high current. In this case, flux should be expelled from the sample, that is, should move in a direction opposite to the Lorentz force. Inasmuch as this process is inhibited, the induction profile within the sample, and consequently the persistent current j, are ”frozen”, and the magnetization $m_H(T)$ is constant, similar to what is obtained in standard field-cooled measurements. Only when a high enough temperature is reached, at which the persistent current $j_T(H)$ is smaller than the frozen value of $j_H(T)$, can flux enter the sample. This is manifested by a change in the slope of $m_H(T)$. This explanation is further illustrated in Figure III-8, in which $m_T(H)$ curves (solid circles) are mapped onto the $m_H(T)$ curve (open squares) in NCCO.

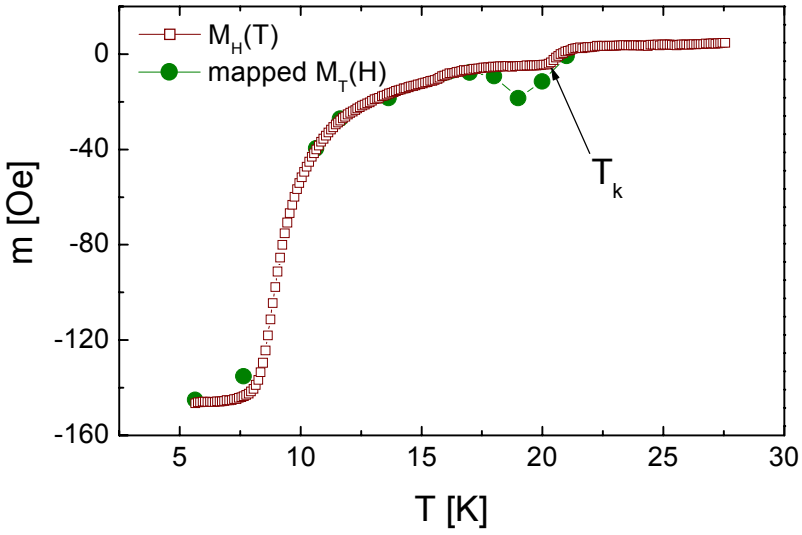

Figure III-8. $m_H(T)$ and "mapped" data points for $m_T(H)$, demonstrating "freezing".

The two curves coincide up to the solid-solid transition temperature, after which $m_H(T)$ freezes and lies above the data mapped from $m_T(H)$. Only when $m_H(T) = m_T(H)$ can flux enter and the two data sets again coincide. We conclude that although the anomalies in $m_H(T)$ are associated with the vortex solid-solid phase transition, the location of the anomalies does not necessarily indicate the location of the transition.

III.1.1.5 Summary of the experimental results in NCCO

Magnetization *vs.* field (*m vs. H*) in NCCO crystal reveals as sharp onset of the second peak, as in BSCCO at local induction B_{on}. Relaxation measurements in NCCO demonstrate a crossover in the creep mechanism in the vicinity of the second peak field B_p, from elastic to plastic creep, thus indicating a disordering (related to dislocations proliferation) of the vortex matter induced by field increase. The induction profiles exhibit sharp crossover near B_{on} from the structure typical of surface and geometrical barriers in the presence of weak bulk pinning to Bean-like profile-structure: This crossover results from the onset of the strong pinning at B_{on}. In

addition, a kink in *m vs. T* of NCCO is observed in the range of fields where B_{on} is found. However, the location of this kink in the (*B,T*) phase diagram does not coincide with the location of B_{on}. This is explained as a consequence of the decreasing $B_{on}(T)$ line in NCCO, resulting in freezing of flux when the $B_{on}(T)$ line is crossed through a temperature increase.

All these measurements point to a vortex solid-solid phase transition.

III.1.2 $YBa_2Cu_3O_{7-\delta}$

In twinned $YBa_2Cu_3O_{7-\delta}$, the usually observed smeared peak with unresolved onset was difficult to associate with a vortex phase transition. Only recently, measurements in untwinned $YBa_2Cu_3O_{7-\delta}$ revealed a well-resolved second magnetization peak [75, 76], similar to that observed in $Bi_2Sr_2CaCu_2O_{8+\delta}$ and $Nd_{1.85}Ce_{0.15}CuO_{4-\delta}$ crystals. However, the peak is still broad and the identification of a specific feature that would possibly mark a phase transition remains unclear. As we shall clarify below, this identification becomes critical in YBCO, because values and temperature dependences of various features differ greatly.

In this section, we present local magnetic measurements in an untwinned $YBa_2Cu_3O_{7-\delta}$ crystal as a function of temperature, field and time, revealing anomalies occurring along the *same* line $B_k(T)$ in the field-temperature plane. These include: (1) an abrupt increase in the local magnetization *vs*. temperature; (2) a pronounced time-independent kink in the magnetization *vs.* field curves; (3) a marked change in the behavior of the magnetic relaxation rate with field; and (4) change in the scaling behavior.

III.1.2.1 Samples

Untwinned $YBa_2Cu_3O_{7-\delta}$ crystals ($T_c \approx 93$ K) were grown by quenching the tetragonal phase during flux growth. Two of them from the same batch were measured in the framework of this work: E1 sample with dimensions 0.5 x 0.3 x 0.02 mm^3 and Y1 sample with dimensions 0.6 x 0.35 x 0.02 mm^3. [77] Although we mostly concentrate in this thesis on results obtained for sample E1 (the results for the two samples are qualitatively the same), we perform quantitative comparison between the results for these two samples in Sections III.1.2.7 and III.2.3.1. This comparison is a powerful tool for testing a theory.

III.1.2.2 Local mgnetization curves in YBCO

The local magnetization of the E1 sample was measured as a function of field at a constant temperature, in the range 40 to 90 K. Typical results, for $T = 60$ K, are shown in Figure III-9.

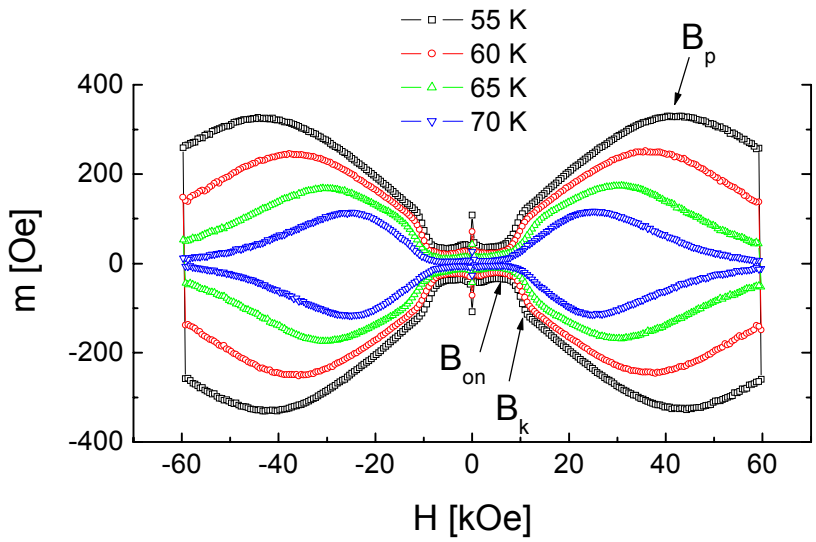

Figure III-9. Local magnetization $m=B-B_{edge}$ in YBCO at the indicated temperatures.

A well-resolved onset of the second peak, similar to that reported for $Bi_2Sr_2CaCu_2O_{8+\delta}$ [11] and $Nd_{1.85}Ce_{0.15}CuO_{4-\delta}$ (see section III.1.1.1), is observed here. We call attention to the pronounced kink at a field B_k in between the onset-field B_{on} and the peak-field B_p as indicated in Figure III-9. The temperature dependence of B_k is shown by open circles in the magnetic phase diagram of Figure III-10, together with the irreversibility line (crosses - determined from the coincidence of the ascending and descending branches of the magnetization curves), and the melting line (diamonds - determined by a discontinuity in $\Delta m($T) in the *reversible* regime: noisy data in the reversible regime was averaged to reveal the jump in the magnetization associated with the melting. This process yielded results consistent with curves obtained in other works [78-81]. No jump could be revealed above 20 kG.)

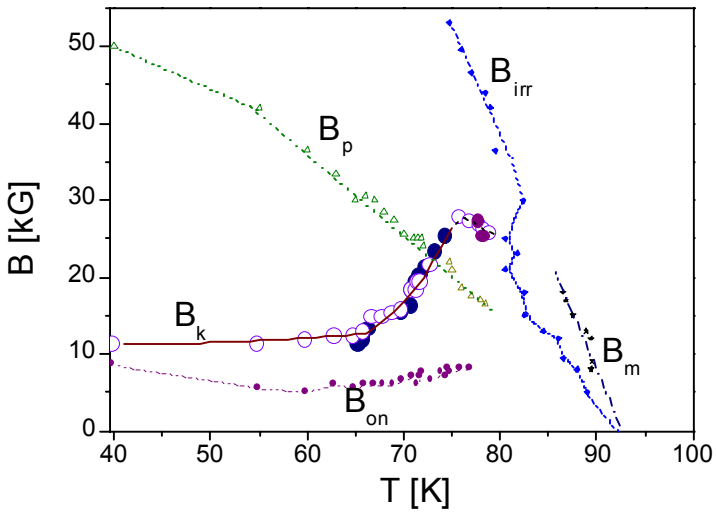

Figure III-10. Magnetic phase diagram for the $YBa_2Cu_3O_{7-\delta}$ crystal showing the temperature T_k of the abrupt increase in $m(T)$ (solid circles), the kink-fields B_k in $m(H)$ curves (open circles), the peak-field (triangles), the onset-field (dots), the irreversibility line (crosses), and the melting line (diamonds). Solid lines are theoretical fits (as discussed in section III.2.3).

III.1.2.3 Local magnetization *vs.* temperature measurements in YBCO

The local zero-field-cooled magnetization, m_{zfc}, and the field-cooled magnetization, m_{fc}, of the same $YBa_2Cu_3O_{7-\delta}$ sample were measured as a function of temperature at a constant field, in the range 1 kG to 55 kG. To compensate for the temperature dependence of the sensors' background, we subtract m_{fc} from m_{zfc}. Figure III-11 presents $\Delta m = m_{zfc} - m_{fc}$ for three representative fields: 8, 16 and 40 kG applied parallel to the c axis.

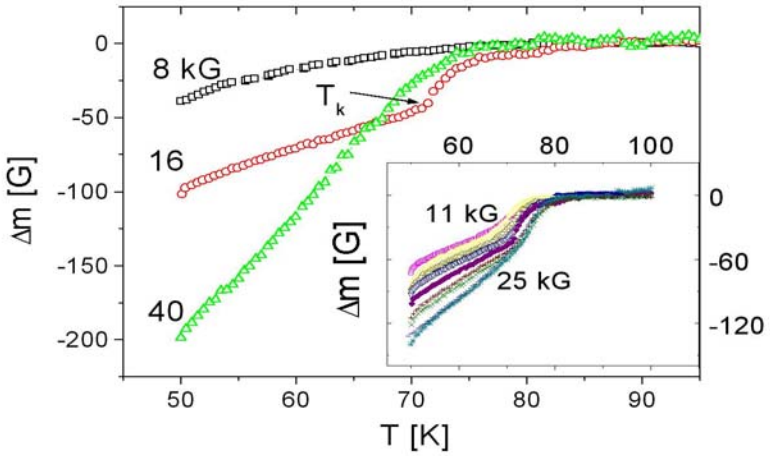

Figure III-11. Difference between the zero-field-cooled and the field-cooled local magnetization in untwinned $YBa_2Cu_3O_{7-\delta}$ plotted *vs.* temperature for 8, 16 and 40 kG fields applied parallel to the c axis. The abrupt increase at $T_k \approx 71$ K for the 16 kG curve is marked by an arrow. The inset shows data for several fields between 11 and 25 kG.

The 16 kG curve exhibits an abrupt increase at $T_k \approx 71$ K, as indicated in the figure. A similar feature is observed for all fields between 11 and 25 kG, see inset to Figure III-11. The temperature T_k increases with the field, as described in Figure III-10 (solid circles).

This feature disappears below 11 kG and above 25 kG where a smooth curve is observed, as represented in Figure III-11 by the 8 and 40 kG curves, respectively.

Note, however, the change in the shape of these two curves. The 40 kG curve exhibits a linear increase over a wide temperature range, and the 8 kG curve is nonlinear.

A central result here is that the line defined by B_k (open circles) coincides with the line defined by T_k (solid circles), suggesting a phase transition in the vortex system across this line. Evidently, the line defined by B_k(T) divides the *irreversible* phase into two regions, suggesting that B_k is a transition line between two *solid* phases of the vortex system. We note here that, in contrast to BSCCO, in which all the features of the second peak are located in a relatively dense manner and have qualitatively similar behavior, in YBCO the choice of the feature signifying phase transition is highly important, because the temperature dependences are qualitatively different for different features (see Figure III-10).

III.1.2.4 Local relaxation measurements in YBCO

We show, in Figure III-12, the evolution of the second peak with time in the time range 10 to 3000 sec (solid squares) and the relaxation rate dm/dlnt *vs.* field (triangles). It is evident from Figure III-12 that, in contrast to the peak-field, which drifts with time to lower fields, the kink-field B_k is time independent. As indicated in the figure, the relaxation rate dm/dlnt (triangles) exhibits a minimum at B_k, a behavior consistent with the observation of time-independent B_k.

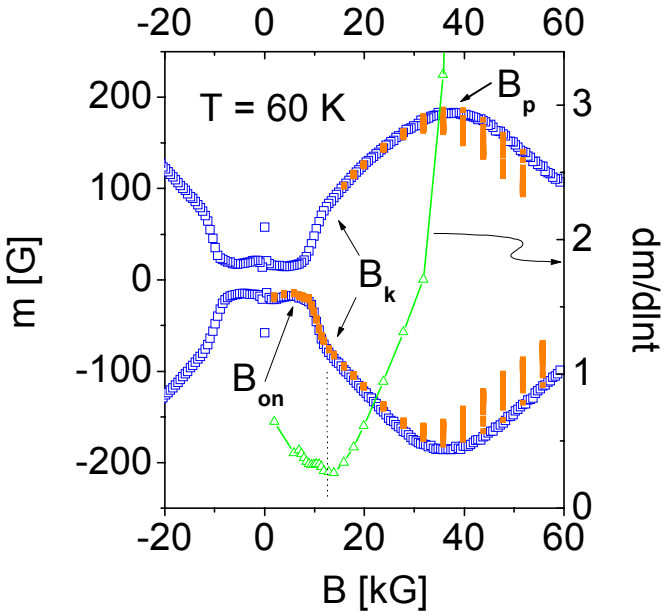

Figure III-12. Local magnetization of the $YBa_2Cu_3O_{7-\delta}$ sample as a function of field as measured at T = 60 K. The solid squares describe the evolution of m(B) with time between 10 and 3000 sec. The relaxation rate (right-hand ordinate) is indicated by triangles.

The temperature dependence of the peak-field B_p, in the short time limit, is also included in Figure III-10 (triangles). As mentioned above, the peak-field drifts with time to lower fields, indicating that $B_p(T)$ cannot be a phase transition line; it signifies a crossover in the dynamics, from elastic to plastic flux creep (see [74] and DG5). Note that the temperature dependence of B_p is qualitatively different from that of the phase transition line B_k. The lines $B_k(T)$ and $B_p(T)$ meet at approximately 73 K, above which the anomalous second peak splits into two peaks, as previously reported by Deligiannis *et al.* [75]. A kink in the magnetization curve is now observed in between the two peaks. The B_p and the B_k data of Figure III-10, above the crossing point T = 73 K, represent the location of the lower peak and the kink that appears above it, respectively.

III.1.2.5 "Scaling" of the magnetization curves in YBCO

More evidence for a phase transition at B_k is illustrated in Figure III-13: Scaling of the magnetization curves at different temperatures in a field range, which includes B_k is unsuccessful.

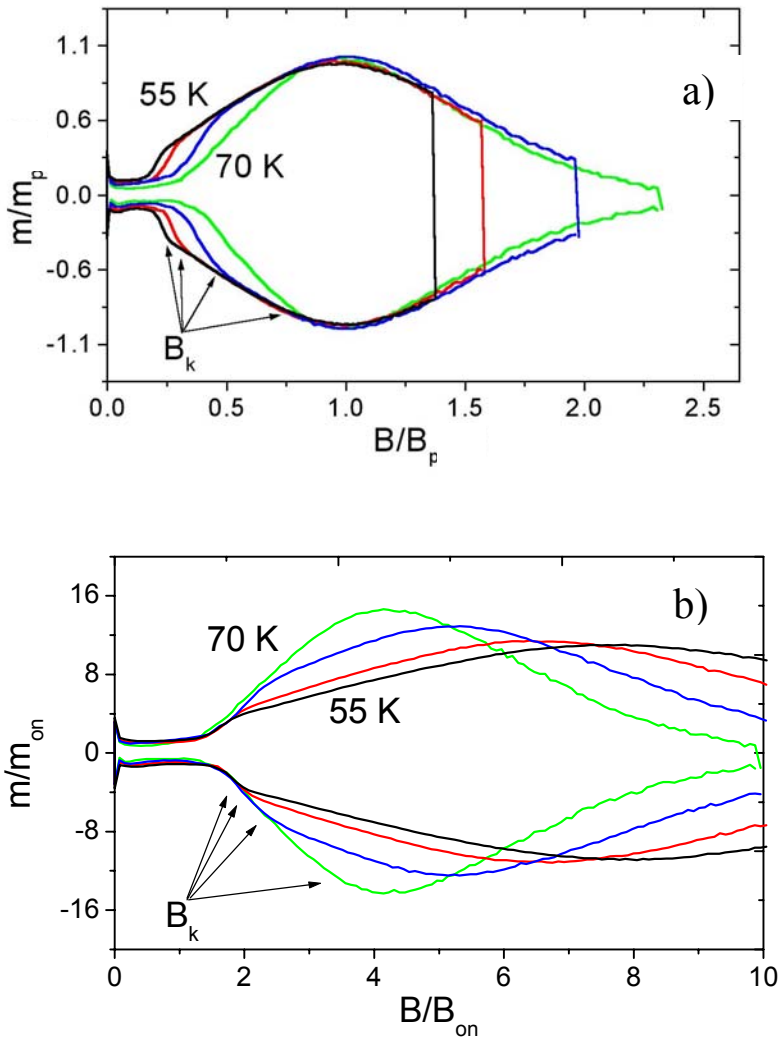

Figure III-13. Scaled magnetization curves for YBCO between 55 and 70 K. Attempts to scale the curves in the whole field range are unsuccessful. However, separate scaling can be obtained for fields (a) larger and (b) smaller than B_k.

However, as demonstrated in Figure III-13a, the magnetization curves can be perfectly scaled above and below B_k separately. Above B_k (Figure III-13a), the

magnetization curves are scaled by the peak field B_p and the magnetization peak value m_p. Below B_k (Figure III-13b), the scaling parameters are the onset field B_{on} and the magnetization m_{on} at that field. The perfect scaling above and below B_k suggest the different nature of the vortex matter states above and below this field. This result, together with the accumulated results mentioned above, indicate that the kink field marks the vortex solid-solid phase transition.

III.1.2.6 Identification of B_k as the field of phase transition in YBCO

As we have shown, local magnetic measurements in an untwinned $YBa_2Cu_3O_{7-\delta}$ crystal (as a function of temperature, field and time) exhibit anomalies along the *same* line $B_k(T)$, which is identified as a transition field between two vortex solid phases.

As is clear from Figure III-11 and Figure III-10, the local magnetization *vs.* temperature exhibits an abrupt increase in a limited field range only, corresponding to the increasing branch of $B_k(T)$. Crossing this branch by raising temperature at a constant field corresponds to a phase transition from a state with relatively high persistent current to a state with low current. This phase transition is accompanied by a burst of flux lines penetrating the sample, manifested by an abrupt increase in the magnetization. This feature is absent when further raising the temperature to cross the $B_k(T)$ line along its decreasing branch. This is because the system crosses from a high-current to a low-current state, that is, flux should be expelled from the sample, a process that is impeded by the presence of an external field (similarly to the phenomenon observed in NCCO, see III.1.1.4). The transition in this case is manifested by a slight decrease in dm/dT at the transition. For fields larger than 25 kG and smaller than 11 kG, raising the temperature does not lead to crossing of the $B_k(T)$ line and, thus, no sign of a phase transition is observed in $m(T)$ measurements.

As we mentioned, the three fields indicated in Figure III-10, B_{on}, B_k, and B_p, characterize the anomalous second peak in the untwinned $YBa_2Cu_3O_{7-\delta}$. We identified B_k as a transition field between two vortex solid phases and B_p as related to a dynamic crossover from elastic (collective) to plastic flux creep. The increase of the persistent current at onset field B_{on} probably originates from the transient phenomena described in Chapter IV.

III.1.2.7 Quantitative comparison of different YBCO samples

In this section, we compare data measured in two YBCO samples, denoted as Y1 and E1 (see III.1.2.1). This comparison will enable us to extract relationships between important pinning characteristics, such as disorder parameter γ and single vortex depinning temperature T_{dp}, for the two samples and a similar relationship between $B_k(T\rightarrow 0)$. These relationships will help us test the disorder-induced transition model in the theoretical section III.2.3.1.

The width of the magnetization loop at low and high magnetic fields far from the transition was extracted at the same temperature for both samples, as well as the value of the transition field $B_k(T\rightarrow 0)$ (see Table III-2). The results of comparison are presented in the following table:

	Sample Y1	***Sample E1***
$B_k(0)$, kG	7	11
Δm_{low}, G	182	113
Δm_{high}, G	1000	700

Table III-2. Comparison of two YBCO samples. First row: $B_k(T\rightarrow 0)$. Second and third rows: width of the magnetization loop Δm for T = 55 K at H = 1000 Oe and H = 40 kOe, respectively. These values were probed at the same distance of about 130 μm from the edge to ensure that the ratio between Δm for the two samples represents a ratio between persistent currents.

We find that, consistently, the hysteresis loop is wider in the sample Y1 than in the sample E1: both Δm_{low} and Δm_{high} are larger for Y1 than for E1. This fact indicates that the pinning in Y1 is stronger. To estimate the ratio between disorder parameters γ, characterizing pinning strength, for Y1 and E1, we assume here that at low fields vortices are pinned in a single vortex (SV) regime. Because in this regime $j \propto j_c \propto \gamma^{2/3}$ [8], and, in general, $j \propto \Delta m$, we obtain $\frac{\gamma(Y1)}{\gamma(E1)} \simeq \left[\frac{\Delta m(Y1)}{\Delta m(E1)}\right]^{3/2}$. Calculation then yields $\frac{\gamma(Y1)}{\gamma(E1)} \approx 2$ under an assumption that at H = 1000 Oe, the creep is governed by SV regime, that is, taking $\Delta m = \Delta m_{low}$.

We are also able to extract the relationship between depinning temperatures T_{dp} for samples Y1 and E1, which is determined by $T_{dp} \propto \gamma^{1/3}$ [8], yielding $\frac{T_{dp}(Y1)}{T_{dp}(E1)} \approx 1.25$.

Finally, from Table III-2 we extract $\frac{B_k(Y1)}{B_k(E1)} \approx 0.64$. This experimentally obtained ratio will be compared with a theoretically predicted one in Section III.2.3.1.

III.1.2.8 Summary of the experimental results for YBCO

Magnetization *vs.* field (*m vs. H*) in YBCO crystals reveals as sharp onset of the second peak, as in BSCCO and NCCO. We also observe, for the first time, a pronounced kink in *m vs. H* curves of YBCO. This kink's location on the (*B,T*) phase diagram of YBCO coincides with a no less pronounced kink in magnetization *vs.* temperature (*m vs. T*) curves; the latter is observed in a range of fields that is exactly the range where B_k is observed. The kink field B_k is also signified by a minimum in the relaxation rate. It is not moving with time, in contrast to another characteristic

field B_p, the field of the second peak. We also find that magnetization loops measured at different temperatures may be "scaled," either for fields lower than B_k or for fields higher than B_k, supporting the existence of different vortex phases below and above B_k. All these results point to a vortex solid-solid phase transition in YBCO occurring at the kink field B_k, rather than the onset field B_{on}.

The kink in m *vs.* T curves of YBCO is observed in the range of fields where B_k is found. However, in contrast to NCCO, the location of this kink in the (B,T) phase diagram *does coincide* with the location of B_k in *m vs H* curves. This is explained by a different behavior of the solid-solid transition line: It decreases in NCCO and increases in YBCO.

III.1.3 $Bi_{1.6}Pb_{0.4}Sr_2CaCu_2O_{8+\delta}$

Our next step was to investigate a system with high T_c, as, for example, in BSCCO, but with a somewhat reduced anisotropy. For this purpose we analyzed the "fishtail" data obtained for BSCCO after Pb-doping, known to reduce the anisotropy without affecting much T_c. In this section, raw data measured for $Bi_{1.6}Pb_{0.4}Sr_2CaCu_2O_{8+\delta}$ (Pb-BSCCO) are presented. These data were measured in our laboratory by M. Baziljevich and Y. Abulafia (for more details, see Ref. DG17 in the Appendix). We performed the analysis presented in Section III.2.4 of this thesis.

III.1.3.1 Local magnetization curves in Pb-BSCCO

Figure III-14 shows typical magnetization loops $m=B_4-B_{8,9}$ measured for the Pb-doped sample, plotted against the local induction B_4.

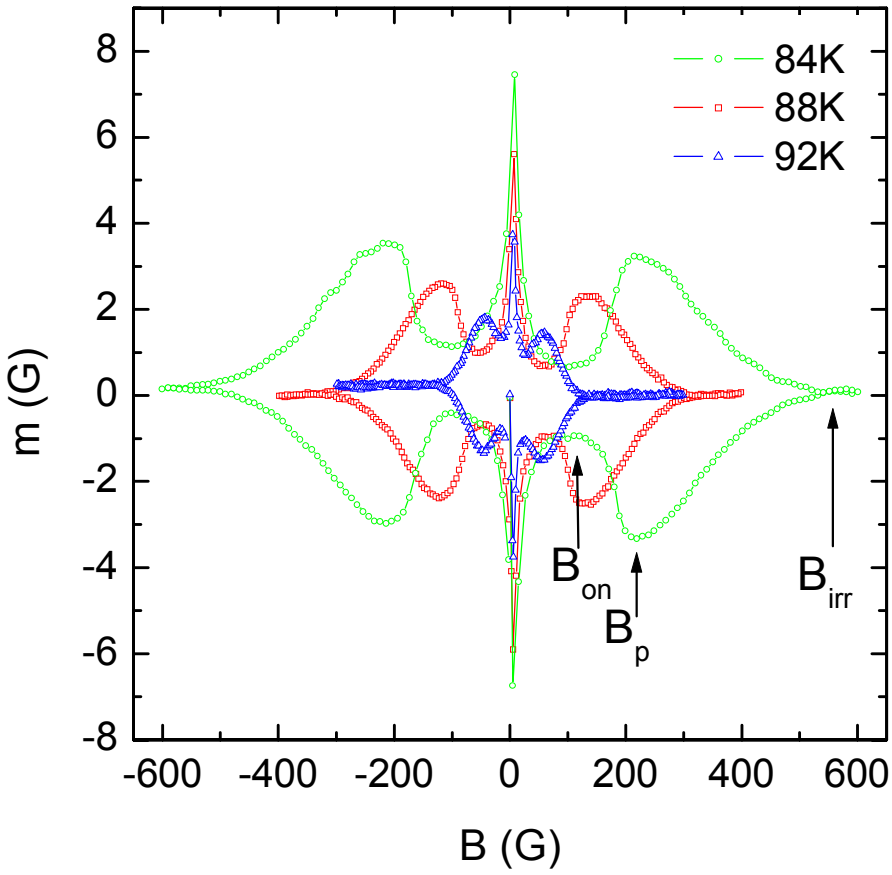

Figure III-14. Magnetization loops $m=B_4-B_{8,9}$ plotted against the local induction B_4, for the Pb-BSCCO crystal at 84, 88 and 92 K.

Probe 4 is located close to the sample center, whereas $B_{8,9}$ is the average signal of probes 8 and 9, which are located close to the neutral line position. At the neutral line, B is approximately equal to the applied field H. The three loops in Figure III-14 were obtained at 84, 88, and 92 K, illustrating the particular temperature dependence of the magnetization in this temperature range near T_c. The sample exhibits a distinct second peak, that is, a strong increase in the magnitude of the magnetization in an intermediate field range. Experimentally, one may define three characteristic fields, which are indicated in the figure: B_{on}, B_{sp}, B_{irr}. The temperature dependence of these characteristic fields forms a phase-diagram in the B-T plane.

The phase diagram obtained for the Pb-doped sample in the temperature range 15-92 K is presented in Figure III-15.

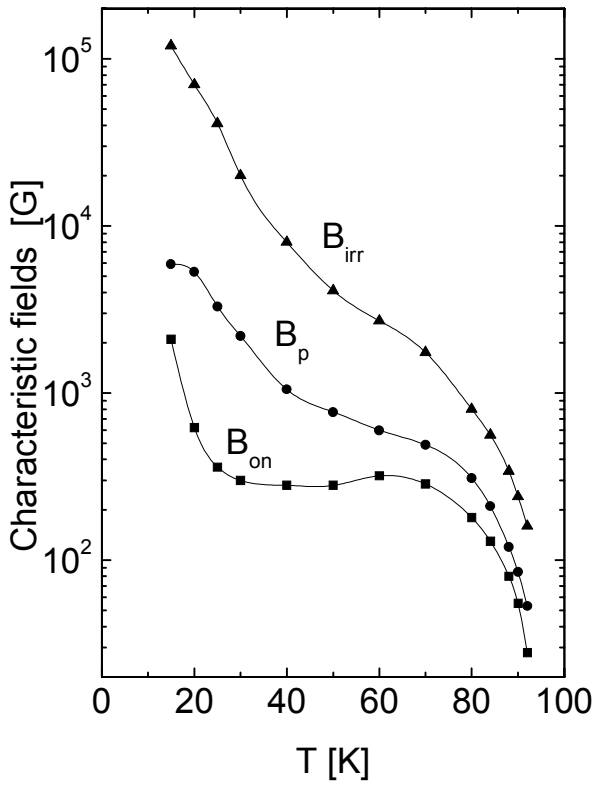

Figure III-15. Magnetic phase diagram defined by the fields B_{on}, B_p, and B_{irr}, determined for the Pb-BSCCO sample.

All the fields (B_{on}, B_{sp}, and B_{irr}) are found to exist over this whole temperature interval. Between 25 and 50 K, the value of B_{on} is approximately constant. The value then slightly increases and after 70 K decreases rapidly, together with the other characteristic fields, as T approaches T_c. Below 25 K, B_{on} rapidly approaches the value of B_{sp}. This occurs because the magnitude of the full penetration field becomes comparable to the characteristic field of the second peak, eventually masking the fishtail effect at the lower temperatures.

III.1.3.2 Local relaxation measurements in Pb-BSCCO

Relaxation measurements in Pb-BSCCO, as in NCCO, show (see Ref. DG17 in the Appendix) that the phase transition cannot be located at the peak, because its position is determined by dynamics. The onset position, however, is more likely to describe the real location of the phase transition. It is also evident from these measurements that after the second peak the relaxation is dominated by plastic creep, similar to what happens in NCCO.

III.1.3.3 Summary of the experimental results for Pb-BSCCO

Local *m vs. H* measurements in Pb-BSCCO reveal a sharp onset B_{on} of the second peak, as in YBCO and NCCO. The range of fields in which B_{on} is observed is close to that of NCCO. However, its temperature dependence is non-monotonic, rather, a reminder of that of B_k in YBCO (see Figure III-10). Results of relaxation measurements indicate that B_{on}, and not B_p, is a field of the phase transition in Pb-BSCCO. They also indicate that after the second peak, the relaxation is dominated by plastic creep similar to the scenario in NCCO.

III.2 Theoretical analyses of the vortex phase transition lines

In this section, we analyze the experimentally measured phase transition lines in the light of the model of disorder-induced transition. [14-16, 18, 19] We coin a common name, B_{ss}, for B_{on} in NCCO and Pb-BSCCO and B_k in YBCO. This name describes a field of the solid-solid transition. We show below that the behavior of $B_{ss}(T)$ in all three systems can be explained on the basis of this model, despite the qualitatively different behavior of $B_{ss}(T)$ observed in these systems.

III.2.1 Derivation of $B_{ss}(T)$

In the context of the disorder-induced transition model [14-16, 18, 19] mentioned above, in the region in which the thermal energy may be neglected, B_{on} is determined by equating the elastic energy

$$E_{el} = \varepsilon\varepsilon_0 c_L^2 a_0 \tag{III.6}$$

with the pinning energy $E_{pin} = U_{dp}(L_0 / L_c^0)^{1/5}$. In these expressions $\varepsilon_0 = (\Phi_0 / 4\pi\lambda)^2$, is the vortex line tension, c_L = 0.1 − 0.3, the Lindenmann number,

$$U_{dp} = (\gamma\varepsilon^2\varepsilon_0\xi^4)^{1/3} \tag{III.7}$$

is the single vortex depinning energy, $L_0 \approx 2\varepsilon a$ the characteristic length for the longitudinal fluctuations induced by elastic interactions, $L_c^0 = (\varepsilon^4\varepsilon_0^2\xi^2 / \gamma)^{1/3}$ the size of the coherently pinned segment of the vortex, γ the disorder parameter, and (in the 3D case) $s<L_c<L_0$. The equation

$$E_{el} = E_{pin} \tag{III.8}$$

then yields

$$B_{ss} = B_0[U_0 / U_{dp}]^3 \tag{III.9}$$

where $B_0 = c_L^2\Phi_0 / \xi^2$ and $U_0 = c_L\varepsilon\varepsilon_0\xi / 2^{11/6}$, and finally

$$B_{ss} = 2^{-11/2}\frac{c_L^5\Phi_0^3\varepsilon}{16\pi^2\lambda^2\xi^3\gamma} \tag{III.10}$$

Thus, the temperature dependence of B_{ss} has its origin in the temperature dependence of ξ, λ, and γ. Although the temperature dependence of ξ and λ is universal, that of γ depends on the pinning mechanism. Pinning may be caused by spatial fluctuations of T_c ("δT_c-pinning") or of the charge carrier mean free path l ("δl-pinning") near a lattice defect. Spatial variations of T_c lead to spatial modulation of the linear and quadratic terms in the Ginzburg-Landau (GL) free energy functional, whereas

variations of the mean free path affect the gradient of the order parameter in the GL functional. (For further discussion, see Ref. [8], p. 1141). Our fitting procedure demonstrates that the temperature dependence of $B_{ss}(T)$ determines, unequivocally, which one of these two pinning mechanisms dominates, as these two pinning mechanisms give rise to qualitatively different behavior of $B_{ss}(T)$: For δT_c-pinning $\gamma \propto 1/\lambda^4$ and

$$B_{ss}(T) = B_{ss}(0)\left[\xi(T)/\xi(0)\right]^{-3} = B_{ss}(0)\left[1-(T/T_c)^4\right]^{3/2} \qquad \text{(III.11)}$$

that is, B_{ss} decreases monotonically with T, whereas for δl-pinning $\gamma \propto 1/(\lambda\xi)^4$, and

$$B_{ss}(T) = B_{ss}(0)\xi(T)/\xi(0) = B_{ss}(0)\left(1-(T/T_c)^4\right)^{-1/2} \qquad \text{(III.12)}$$

that is, B_{ss} increases with T.

We show below the success of this theoretical model in explaining the data obtained in the previous sections.

III.2.2 $Nd_{1.85}Ce_{0.15}CuO_{4-\delta}$

It can be shown that that the condition for the 3D case ($s<L_c<L_0$) is fulfilled in NCCO (where $s \approx 0.6nm$) in most of the temperature range, as may be verified by substituting ε = 1/30 [71] ξ = 8 nm [82, 83], λ = 100 nm ([5]) and $j_c = \frac{c}{\Phi_0}\left[\frac{\gamma^2}{\varepsilon_0\xi}\right]^{1/3} \approx 10^6 A/cm^2$ (estimated from the width of the hysteresis magnetization loop) in the above expressions for L_c and L_0, yielding $L_c \approx 3$ nm and $L_0 \approx 30$ nm. (L_0 was calculated for B = 200 G ~ B_{ss}.)

[5] The penetration depth λ was estimated from our magnetic measurements of the lower critical field and is consistent with Ref. [84].

A one-parameter fit of B_{ss} for $Nd_{1.85}Ce_{0.15}CuO_{4-\delta}$ to Eq. (III.11) yields $B_{ss}(0)$=270 G. The fit is shown in Figure III-3 (solid line).

The agreement between the calculated and measured data is apparent. Returning to Eq. (III.9) when $T = 0$ is substituted we extract the value of $T_{dp} \equiv U_{dp}(0) \approx 60K > T_c$, confirming that thermal depinning is insignificant in the NCCO experiment.

The above analysis allows comparison of the three energy scales, E_{el}, E_{pin} and E_{th}, in the NCCO system. These energies are shown in Figure III-16 as a function of temperature and field.

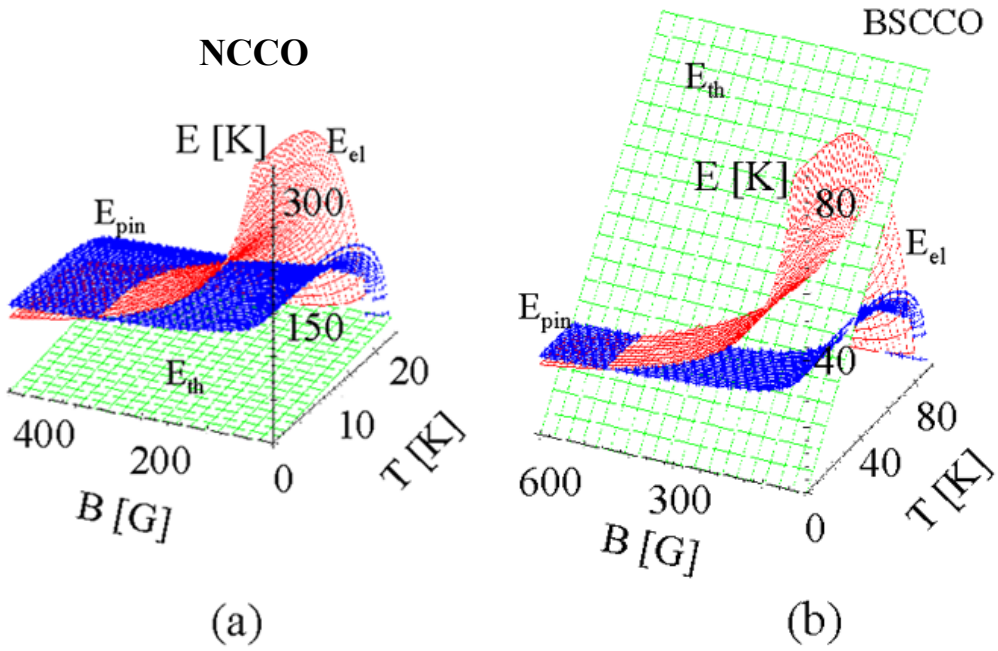

Figure III-16. Elastic (E_{el}), pinning (E_{pin}) and thermal (E_{th}) energies as a function of temperature and field (a) for NCCO and (b) for BSCCO. E_{th} is negligible in most of the temperature range in NCCO but only at low temperatures in BSCCO. In these temperature ranges, $B_{on}(T)$ is the projection of the crossing line E_{el}=E_{pin} on the B-T plane. In BSCCO, the melting line is the projection of the crossing line E_{el}=E_{th} on the B-T plane.

The figure demonstrates that both E_{el} and E_{pin} are decreasing functions of temperature and field, but the decrease of the elastic energy is faster, causing $E_{el}(B,T)$ and

$E_{pin}(B,T)$ surfaces to cross each other. The projection of this crossing line on the B-T plane is the $B_{on}(T)$ line.

Note that the thermal energy is well below E_{el} and E_{pin} for most of the temperature range. The situation is different for BSCCO ([6]), as shown in Figure III-16b, using the parameters T_c = 90 K, $\varepsilon = 1/100$, $B_{on}(0)$=450 G. As apparent from the figure, in BSCCO E_{th} plays an important role, and one can identify both $B_{on}(T)$ and the melting line $B_m(T)$. Note that the crossing line of E_{el} and E_{pin} can be viewed as $B_{on}(T)$ only at low temperatures where the contribution of E_{th} can be neglected. Figure III-16b indicates that in this region $B_{on}(T)$ is temperature independent.

III.2.3 $YBa_2Cu_3O_{7-\delta}$

The $B_{ss}(T)$ curve of $YBa_2Cu_3O_{7-\delta}$, Figure III-10, is markedly different from the corresponding curves obtained in $Bi_2Sr_2CaCu_2O_{8+\delta}$ and $Nd_{1.85}Ce_{0.15}CuO_{4-\delta}$ crystals (see Figure I-1 and Figure III-3). While $B_{ss}(T)$ is approximately constant in $Bi_2Sr_2CaCu_2O_{8+\delta}$ and decreases monotonically with temperature in $Nd_{1.85}Ce_{0.15}CuO_{4-\delta}$, it is a non-monotonic function of temperature in the untwinned $YBa_2Cu_3O_{7-\delta}$. In the following, we explain these pronounced differences within the framework of the disorder-induced transition theory [14-16, 18, 19].

In $Bi_2Sr_2CaCu_2O_{8+\delta}$, B_{ss} persists up to only 40 K, well below T_c. In this temperature range ($T<<T_c$) all the superconductor parameters are almost temperature independent. As a result, the line defined by $E_{el} = E_{pin}$ is approximately temperature independent. In $Nd_{1.85}Ce_{0.15}CuO_{4-\delta}$ ($T_c \approx$ 23 K) and $YBa_2Cu_3O_{7-\delta}$ ($T_c \approx$ 93 K), B_{ss}

[6] Note that, due to higher anisotropy in BSCCO, a more accurate analysis that would take into account 2D and 3D pinning regimes (see analyses for Pb-BSCCO in Section III.2.4) is needed. Figure III-16b serves here for purpose of qualitative comparison only.

persists up to at least T/T_c = 0.93 and 0.86, respectively, and, therefore, the temperature dependence of the superconductor parameters affects $E_{pin}(T)$ and $E_{el}(T)$ and, consequently, $B_{ss}(T)$. As discussed below, $B_{ss}(T)$ depends strongly on the specific microscopic pinning mechanism – different mechanisms may cause either an increase or a decrease of B_{ss} with temperature. As a matter of fact, the specific behavior of $B_{ss}(T)$ may serve as a probe for the microscopic pinning mechanism. Thus, both the decrease of $B_{ss}(T)$ in $Nd_{1.85}Ce_{0.15}CuO_{4-\delta}$ up to the close vicinity of T_c, and the weak increase of B_{ss} up to 66 K in $YBa_2Cu_3O_{7-\delta}$ find a natural explanation as a disordered-induced phase transition, taking into account the different origin for the pinning mechanism in these particular samples. Quantitative fits of the experimental data for the three samples show good agreement with the theoretical predictions. A detailed explanation of the fit procedure is outlined in the following paragraphs.

Near the transition, for temperatures below the depinning temperature T_{dp} (defined below), the increase of B_{ss} with temperature observed in $YBa_2Cu_3O_{7-\delta}$ indicates a δl-pinning mechanism, supporting the conclusions of Griessen *et al.* [85, 86]. A one-parameter fit of Eq. (III.12) fits the B_{ss} data for $YBa_2Cu_3O_{7-\delta}$ up to T = 66 K well, as shown by the solid line in Figure III-10, yielding $B_{ss}(0)$ = 11 kG. Above 66 K, $B_{ss}(T)$ exhibits a dramatic increase, which may be attributed to a strong decrease of the pinning energy E_{pin}, suggesting that for our $YBa_2Cu_3O_{7-\delta}$ sample, the depinning temperature T_{dp} = 66 K. This value of T_{dp} will be further justified below. To fit the data above T_{dp}, we note that at 66 K, at the solid-solid transition field, $E_{el} = E_{pin} \approx 80$ K are both comparable to kT, and, thus, one must take into account the contribution of the thermal energy. This may be accomplished by introducing the strong thermal smearing of the pinning disorder through an exponential increase of the Larkin length

$$L_c = (T_{dp} / T) L_c^0 \exp(c((T / T_{dp})^3 - 1)) \qquad \text{(III.13)}$$

for $T > T_{dp}$, where c is a number of order 1 [8, 15]. Introducing this expression of L_c in $E_{pin} = U_{dp}(L_0 / L_c)^{1/5}$, and equating E_{pin} to E_{el} yields the solid line in Figure III-10 between 66 and 75 K, using the *same* parameters as above, that is, T_{dp} = 66 K and $B_{ss}(0)$ = 11 kG. This approach is valid only in the vicinity of T_{dp}. Our calculations show that above 75 K, $L_c > L_0$ and the pinning energy is now given by $E_{pin} \cong \sqrt{\gamma \xi^2 L_0}$ [16], that is, no longer dependent on L_c. Therefore, the fast decrease of E_{pin} with temperature is moderated, and the increase of the superconducting parameters with temperature causes B_{ss} to decrease.

We note that in some samples, for example, doped and electron irradiated $Bi_2Sr_2CaCu_2O_{8+\delta}$ [70, 87, 88], B_{ss} may also increase with temperature, suggesting a δl-pinning mechanism in these samples.

III.2.3.1 Quantitative test of the model: comparison between two samples

The quantitative analysis in the model presented above, is complicated by a presence of unknown parameter c_L. This is why $B_{ss}(0)$ may be determined only through a fit of experimental data. The way to avoid this difficulty in testing theoretical predictions for the influence of pinning strength on the solid-solid transition is to calculate ratios between measurable quantities, such as $B_{ss}(0)$ and $T_{dp,}$ for two different samples with similar properties, except the slightly different disorder strength.

If the disorder-induced transition is correct, then we expect that in the sample with higher pinning, the B_{ss} will be lower. This should be governed by the expression

$$B_{ss}(0) \propto T_{dp}^{-3} \propto \gamma^{-1} \qquad (3.14)$$

This is indeed realized when comparing samples Y1 and E1 (see experimentally obtained values in III.1.2.7). We obtain $\frac{B_{ss}(Y1)}{B_{ss}(E1)} \simeq 0.5$, as compared with $\frac{B_k(Y1)}{B_k(E1)} \approx 0.64$, showing a discrepancy as small as 20%, strongly supporting the model. We can also check the assumption we made that the temperature at which a strong increase in B_{ss} takes place (see Figure III-10) is the depinning temperature T_{dp}. Depinning temperature must grow with an increase of pinning and, therefore, to decrease with increase of B_{ss}. This is governed again by Eq. (3.14). To check our assumption about T_{dp}, we extracted those temperatures from the $B_{ss}(T)$ curves (see Table III-3).

	Sample Y1	***Sample E1***
T_{dp}, ***K***	75	66

Table III-3. Comparison of T_{dp} for samples Y1 and E1.

The relation for T_{dp} coming from Table III-3 is then $\frac{T_{dp}(Y1)}{T_{dp}(E1)} \approx 1.14$, as compared with 1.25 obtained from Table III-2. This discrepancy, as small as 7%, supports our assignment of T_{dp} to a point of strong increase in B_{ss}.

III.2.4 $Bi_{1.6}Pb_{0.4}Sr_2CaCu_2O_{8+\delta}$

In this material, to equate E_{pin} with E_{el} it is important to take into account three possible regimes for the pinning energy. These regimes are defined by the three length-scales in the problem: the interlayer spacing s, the characteristic size of the longitudinal fluctuations in a cage L_0, and the size of a coherently pinned segment of the vortex. For a *2-D* case ($L_c < s < L_0$) [16]

$$E_{pin} \simeq U_p \left(\frac{L_0}{s} \right)^{1/5} \qquad \text{(III.15)}$$

For a *3-D* case ($s < L_c$) [15, 16] if ($L_c < L_0$) it becomes

$$E_{pin} \simeq U_p \left(\frac{L_0}{L_c} \right)^{1/5} \tag{III.16}$$

whereas, for the case $s < L_0 < L_c$ [16]

$$E_{pin} \simeq \sqrt{\gamma L_0} \tag{III.17}$$

where $U_p = \pi\sqrt{\gamma s}$ is one pancake pinning energy. Equation (III.8), in which E_{pin} is determined by (III.15), (III.16), or (III.17) and E_{el} is determined by (III.6), yields the temperature dependence of the solid-solid phase transition line $B_{ss}(T)$ in each of these three regimes.

The curve $B_{ss}(T)$ for Pb-BSCCO is identified by the full squares in Figure III-15. We now consider the $B_{ss}(T)$ dependence in the temperature range $25 < T < T_c$, where it is not influenced by the interference with the "first peak" (see III.1.3). The line $B_{ss}(T)$ is composed of three regimes: (i) B_{ss} initially decreases with T; (ii) B_{ss} then slightly increases with T, exhibiting a maximum; and, finally, (iii) B_{ss} decreases again up to T_c. It can be shown that these three regimes are directly related to the three E_{pin} regimes outlined above. First note that L_0 is temperature independent and, for fields of order B_{ss} (several hundred Gauss), L_0 is larger than the interlayer spacing s = 1.54 nm. (For example, for B=300 G, $L_0 \approx 7.6nm$). Substituting the value of the anisotropy, $\varepsilon = 1/68$, obtained in Ref. DG17 in the Appendix, and reasonable values for $\xi = 1-10nm$ and $\lambda = 100-200nm$, it follows that $L_c << 1$ nm at low temperatures. It is, therefore, possible to conclude that, at low temperatures, we are in the limit of 2D-pinning. Then, substituting Eqs. (III.15) and (III.6) into Eq. (III.8), one obtains, for the δT_c-pinning case:

$$B_{on}(T) \propto \xi^{-5/2} = B_{on}(0)\left[1-\left(T/T\right)^4\right]^{5/4} \tag{III.18}$$

The fit of this expression to the experimental data for $25 < T < 48$ K is shown in Figure III-17.

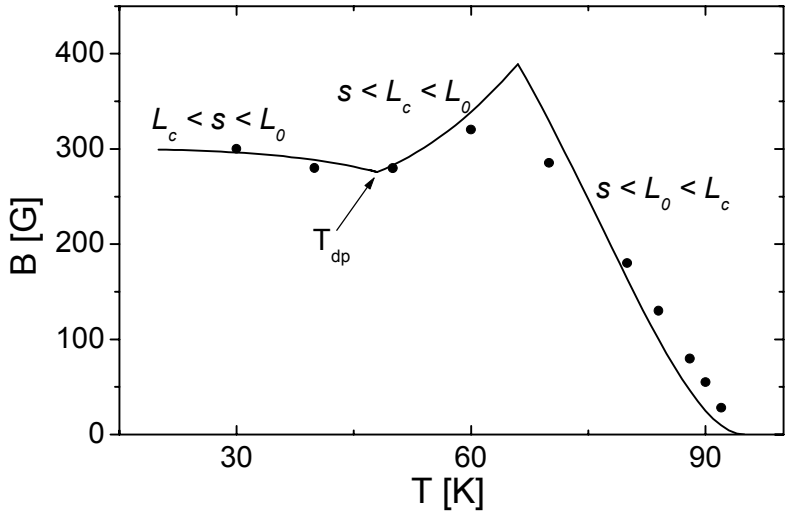

Figure III-17. Second peak onset field B_{on} versus temperature for the Pb-BSCCO crystal (circles) shown together with a theoretical curve $E_{el} = E_{pin}$ for different pinning regimes (solid lines).

Around 48 K, B_{ss} starts increasing with temperature. For none of the parameters in Eq. (III.19) can the temperature dependence change in such a way that B_{ss} will start increasing. Therefore, it seems reasonable to conclude that at around 48 K, there is a crossover to a regime where L_c, exceeds the value of s. A mechanism, which may explain such an abrupt increase in L_c is the temperature smearing of the pinning when the transverse thermal fluctuations of the flux lines become larger than ξ. This occurs at the single vortex depinning temperature. Our experimental results suggest that for Pb-BSCCO, $T_{dp} \approx 48$K. Above this temperature, the Larkin pinning length starts growing exponentially, as given by Eq. (III.13), as a result of a thermal smearing of the quenched disorder. Indeed, our calculations show that in the vicinity of $T \approx 48$ K, $L_c \approx 1$ nm and becomes of order s. This growth causes a crossover to a regime where s

$< L_c < L_0$ and $B_{on}(T)$ is then determined by substituting Eqs. (III.16) and (III.6) into Eq. (III.8). A fit of $B_{ss}(T)$ in the temperature range $48 < T < 66$ K yields the line described in Figure III-17. In this regime, B_{ss} is predicted to increase with temperature. The decrease of B_{ss} with temperature above $T \approx 66$ K implies that at this temperature L_c exceeds the value of L_0. Indeed, our calculations show that, in the vicinity of 66 K, $L_c \approx L_0 \approx 5$ nm, implying the validity of Eq. (III.17) for E_{pin}. A fit of the B_{ss} data for T > 66 K, based on Eq. (III.17), is also shown in Figure III-17.

III.3 Summary and conclusions

In this chapter we identified a vortex solid-solid transition in NCCO, Pb-BSCCO, and untwinned YBCO crystals.

We find that the temperature dependence of the transition field B_{ss} in these crystals differs markedly. Nevertheless, we were able to explain the different behaviors when using the same model, the model of disorder-induced transition, based on the competition between E_{pin} and E_{el}. We applied this model in different vortex regimes and introduced different pinning mechanisms. We showed that, at temperatures lower than T_{dp}, the temperature dependence of B_{ss} originates from the temperature dependence of correlation length ξ.

In contrast to NCCO, for the $B_{ss}(T)$ lines of Pb-BSCCO and YBCO, thermal fluctuations must be explained for temperatures larger than the single vortex depinning temperature. At $T > T_{dp}$, the Larkin length starts to grow exponentially, thus accelerating the decrease of pinning energy. This is reflected in $B_{ss}(T)$ line as a sudden increase at $T = T_{dp}$.

We find also that, from the behavior of the solid-solid transition line at low temperatures ($T < T_{dp}$) one may infer the microscopic origin of the pinning: the

decreasing $B_{ss}(T)$ line implies δT_c-pinning mechanism, and increasing $B_{ss}(T)$ implies δl-pinning. We find, using this method, that NCCO and Pb-BSCCO have δT_c-pinning and YBCO has δl-pinning.

In addition, to describe a temperature dependence of B_{ss} in Pb-BSCCO, transitions among three different pinning regimes must be considered: ($L_c < s < L_0$), ($s < L_c < L_0$) and ($s < L_0 < L_c$). These regimes are crossed in Pb-BSCCO, due to its relatively high anisotropy and critical temperature.

We also test the applicability of the disorder-induced transition in YBCO by testing its predictions with regard to the values of the $B_{ss}(0)$ and T_{dp}. Although these values cannot be obtained directly, because the Lindenmann criterion c_L is unknown, it is possible to test the theoretical prediction for the ratio of B_{ss} and T_{dp} for two crystals with different pinning. We find an experimental value of 1.25, as compared with a theoretically predicted value of 1.14 for T_{dp}, and for B_{ss}, we find an experimental value of 0.64, as compared with a predicted value of 0.5. This indicates a very good agreement between theory and experiment.

The materials chosen for this study (NCCO, Pb-doped BSCCO, and YBCO) have different values of superconducting critical temperature T_c, anisotropy ε, and other superconducting parameters. Nevertheless, we associated the vortex solid-solid transition in these materials with the disorder-induced transition. It is, therefore, expected that the same phenomenon observed in other HTS and LTS crystals is also associated with the disorder-induced transition. This work provides tools for analyzing the behavior of the solid-solid transition in other materials. An additional important result of the proposed analysis is the ability to extract other valuable information, such as the microscopic pinning mechanism, from the behavior of the solid-solid transition line.

IV Nucleation and growth of the vortex solid phases

In the previous chapter, we described the thermodynamic solid vortex phases and the transition between them. In this chapter, we focus on *the process of formation* of the thermodynamic phases, that is, on the transient vortex states preceding the establishment of the equilibrium: thermodynamic states. For the purpose of tracing this transient state, we developed a high-temporal resolution magneto-optical system that enables the imaging of the time evolution of the induction distribution in the tens-of-milliseconds time scale. Our measurements revealed the dynamic coexistence of a quasi-ordered vortex phase and a transient-disordered vortex phase. The growth process of the solid phases could be traced for the time. In the following, we present the experimental results and propose qualitative interpretation. A quantitative analysis, based on the time-dependent Landau-Khalatnikov equation, is presented in the next chapter.

IV.1 Experimental

The study was performed on two BSCCO single crystals, referred to as S1 (0.66 x 0.24 x 0.03 mm^3, $T_c \approx 80$ K) and S2 (1.5 x 0.68 x 0.03 mm^3, $T_c \approx 88$ K), which were grown by T. Tamegai, using the traveling solvent floating zone method [89]. In the temperature range of the experiments described below, B_{ss} is estimated, from static magnetization loops, to be at approximately 400 G for both samples. The normal component of the magnetic induction, B, was detected on the sample's surface, employing magneto-optically active ferrimagnetic iron-garnet films with in-plane magnetization (see Chapter II). Polarized light passing through the indicator changes

its angle of polarization as a function of the local magnetic induction. Measurements were performed immediately after a sudden change in the external magnetic field H_a (change-time ≈ 50 ms) applied parallel to the c-axis and perpendicular to the sample's surface. More than 100 two-dimensional images were then captured by a CCD video camera at minimal time intervals of 40 ms. From these images, one-dimensional profiles (induction *vs.* position) across the sample width were extracted. These profiles are usually obtained by averaging several neighboring profiles.

Two basic types of experiments were performed:

1. *Field-Step-Up (FSU) experiment*

In this kind of experiment (up-pointing arrows in Figure IV-1), the sample is suddenly exposed (field rise-time ~ 50 ms) to a magnetic field H_a, and the time evolution of the flux distribution is monitored.

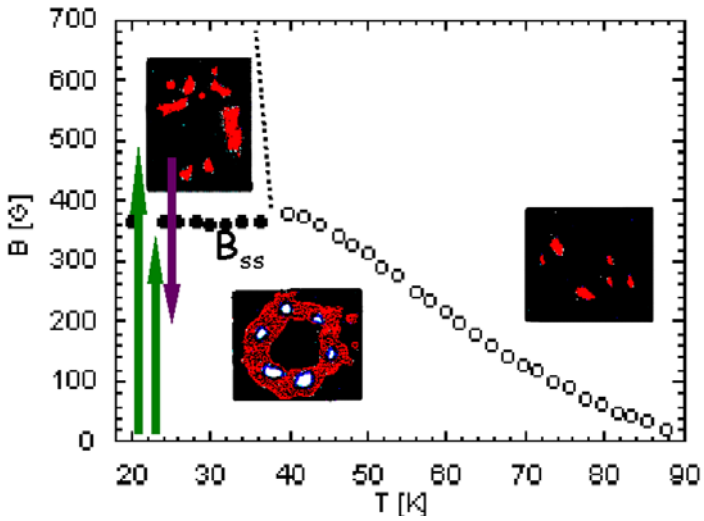

Figure IV-1. Schematic description of FSU and FSD experiments.

2. *Field-Step-Down (FSD) experiment*

In this kind of experiment (down-pointing arrow in Figure IV-1), the magnetic field is first raised to well above B_{ss}, and, then, after long enough waiting time (to

allow for establishment of the high-field phase), the field is decreased sharply to a value $H_a < B_{ss}$, at which value the flux distribution is monitored.

IV.2 Field-step-up experiments

IV.2.1 Imaging of magnetic relaxation from first flux entry to equilibrium ($B_a << B_{ss}$)

Figure IV-2 shows the time evolution of the magnetic induction profiles at T = 20 K, after a step increase (rise time ≈ 50 ms) of the external magnetic field from zero to 400 G. The time elapse between subsequent profiles is 100 ms.

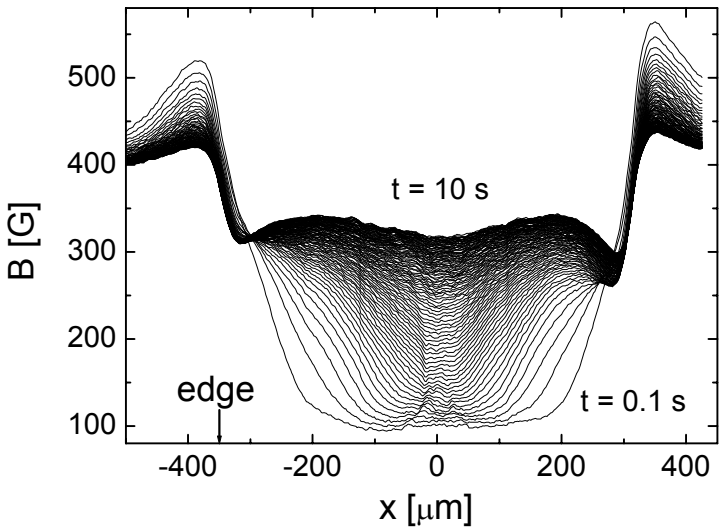

Figure IV-2. Magnetic induction profile evolution after sudden application of magnetic field in the field range of the ordered phase. Sample center is at x = 0.

As indicated by the profiles, the induction near the sample edge ($B_a \approx$ 300 G), is well below B_{ss}. Initially, Bean-type profiles are observed, gradually evolving into equilibrium dome-shaped profiles. The sharp induction step at the edges is due to surface currents j_s [90]. Assuming, in addition to j_s, a uniform bulk current density j_b

(see schematic currents distribution on Figure IV-3), the profiles of Figure IV-2 may be fitted to the Biot-Savart law.

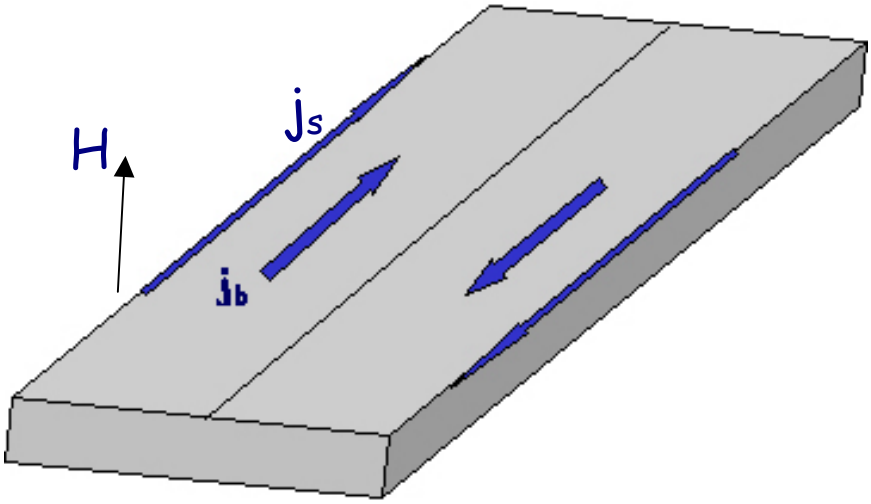

Figure IV-3. Schematic electrical current density distribution under assumption of uniform bulk current.

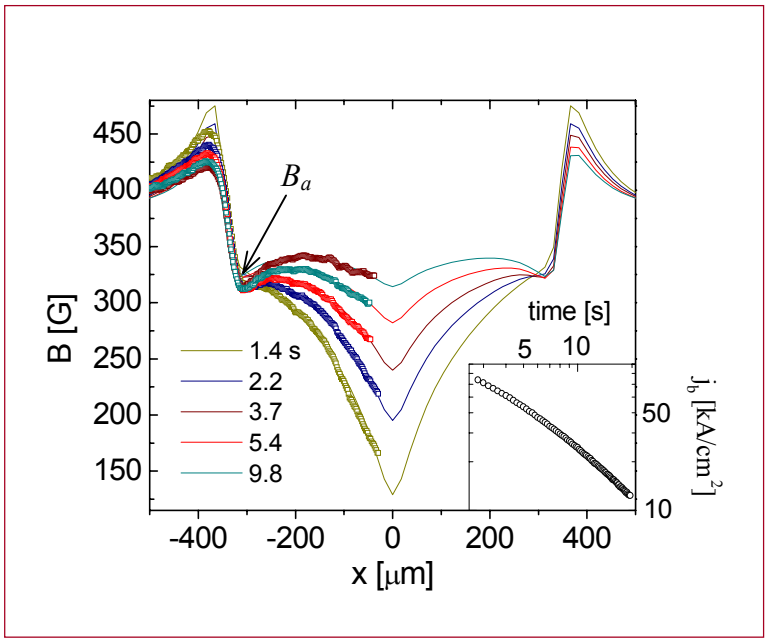

Figure IV-4. Time evolution of the magnetic induction profiles for field H_a = 380 Oe (B_a = 320 G), for sample S2 ($B_{ss} \gtrsim$ 400 G). Profiles shown are measured at t = 1.4, 2.2, 3.7, 5.4, and 9.8 s. Solid lines are theoretical fits with bulk current density j_b and surface current density j_s as parameters. Inset: Log-log plot of j_b *vs* time.

Such a fit is shown in Figure IV-4. In the long time limit, a dome-shaped profile, characteristic of surface and geometrical barriers in thin samples [73], is observed. Inasmuch as $B < B_{ss}$ throughout the sample, the dome-shaped profile implies the establishment of an ordered stable state with vanishing bulk current density j_b. The time dependence of j_b (as deduced from fits of the profiles employing the Biot-Savart law) is shown in the log-log plot in the inset. It exhibits unconventional non-logarithmic creep behavior.

IV.2.2 Dynamic coexistence of two phases ($B_a \sim B_{ss}$)

The data of Figure IV-4 show no evidence for the coexistence of different vortex phases in different parts of the sample. An evidence for such a situation is observed when B_a is closer to B_{ss}. Figure IV-5 shows the time evolution of the magnetic induction profiles in sample S2 at T = 20 K, after a step increase of the external magnetic field from zero to 470 Oe.

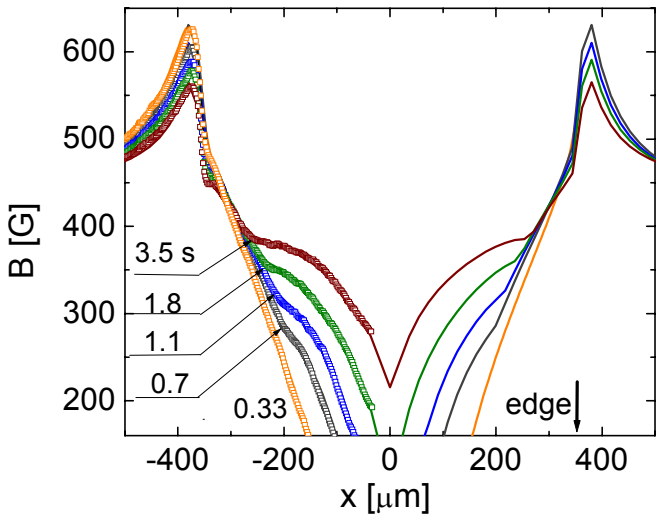

Figure IV-5. Time evolution of the magnetic induction profiles for field H_a = 470 Oe (B_a = 450 G) for sample S2 ($B_{ss} \gtrsim$ 400 G). Profiles shown are measured at indicated times. Solid lines are theoretical fits, with j_s, j_b, j_h, and x_f as fitting parameters. Arrows point to the location x_f of the breaks in the profiles, deduced from the fits.

A striking feature in Figure IV-5 is the development of a sharp change in the slope (break) of the induction profiles at $x = x_f$, (marked by arrows) and at corresponding induction $B = B_f$. Figure IV-5 exhibits the following properties of this break:

1) The induction B_f corresponding to the break is much below $B_{ss} \gtrsim 400$ G.
2) The induction B_f grows with time.
3) The point x_f moves progressively with time toward the sample edges at $|x|=w/2$.

Let us now try to explain the origin of this break. In the following, we show that remarkable changes in the bulk current density and in the magnetic relaxation characteristics occur at the point x_f. We first note that, in contrast to the profiles shown in Figure IV-4, the profiles of Figure IV-5 cannot be reasonably fitted to the Biot-Savart law using a uniform bulk current density. However, assuming two different values, j_h and j_l, for the bulk current density on both sides of x_f (see schematic current distribution on Figure IV-6), one obtains excellent fit, as shown by the solid lines in Figure IV-4. Using the Biot-Savart law, the normal component of the induction is expressed as a function of a surface current density j_s, and bulk current density $j(x)$, which is equal to j_l for $|x| < x_f$, j_h for $x_f < |x| < w/2$ and zero for $|x| > w/2$. Fitting this expression to induction profiles measured at different times yields the time dependence of j_s, j_l, j_h, and x_f.

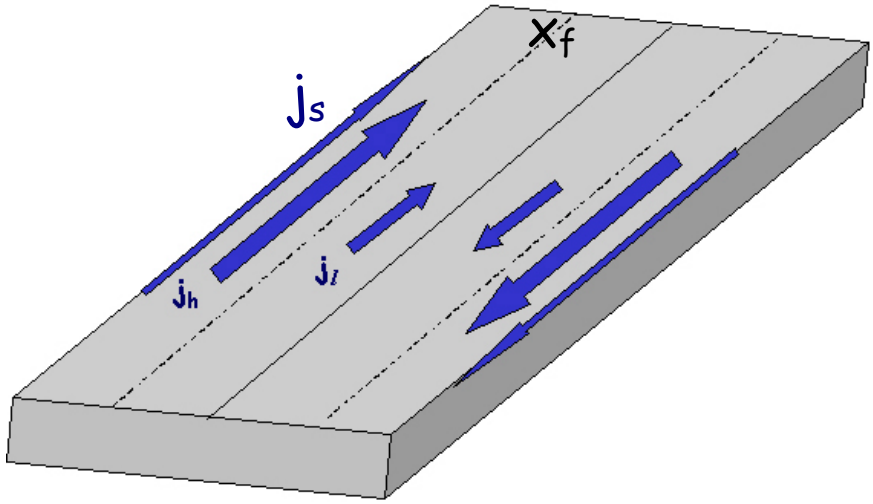

Figure IV-6. Schematic electrical current density distribution in the presence of break at x_f.

The log-log plot in Figure IV-7 shows that the bulk current density j_h, corresponding to the part of the profile near the edges, exhibits a power-law decay with time (fit yields $j_h \propto t^{-0.31}$), whereas $j_l(t)$ exhibits deviations from a power-law; similar deviations were observed in j_b (see inset to Figure IV-4).

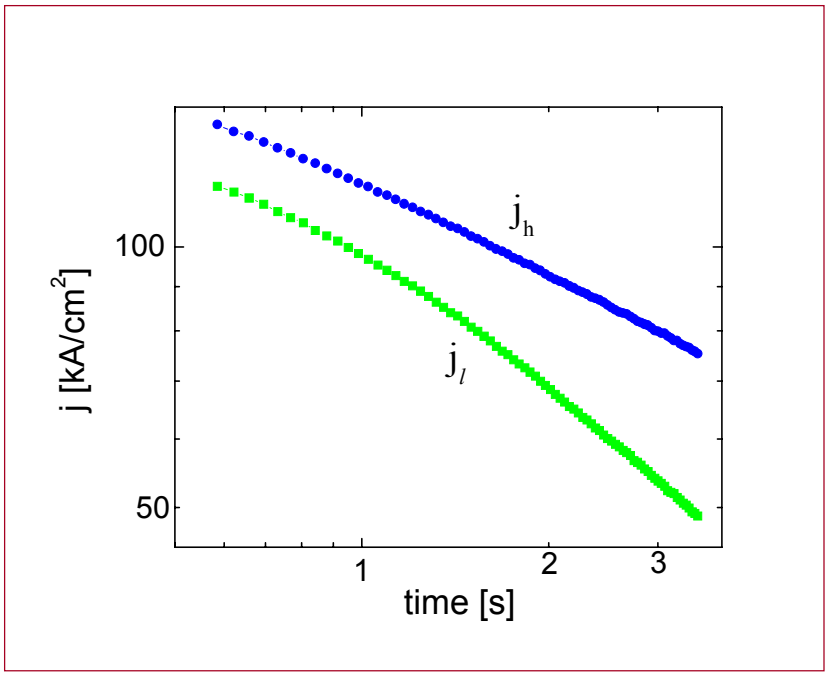

Figure IV-7. Log-log plot of $j_h(t)$ and $j_l(t)$.

The power-law decay observed for $j_h(t)$ implies logarithmic divergence of the activation energy for flux creep, as the current density approaches zero [8, 67]. This behavior is characteristic of the disordered (glassy) vortex state with plastic creep [91-93].

The existence of two different bulk currents on both sides of x_f, the different time-dependence of the currents, and the movement of x_f with time imply *dynamic coexistence* of low- and high-j phases on both sides of x_f.

In an effort to understand the nature of these phases, we extracted the E-j characteristics for both phases (Figure IV-8), by spatially integrating $\partial B_z / \partial t$ in Eq. (III.1). The best fits to a power-law $E \propto j^n$ yield n = 1.9 and n = 3 for j_l and j_h, respectively.

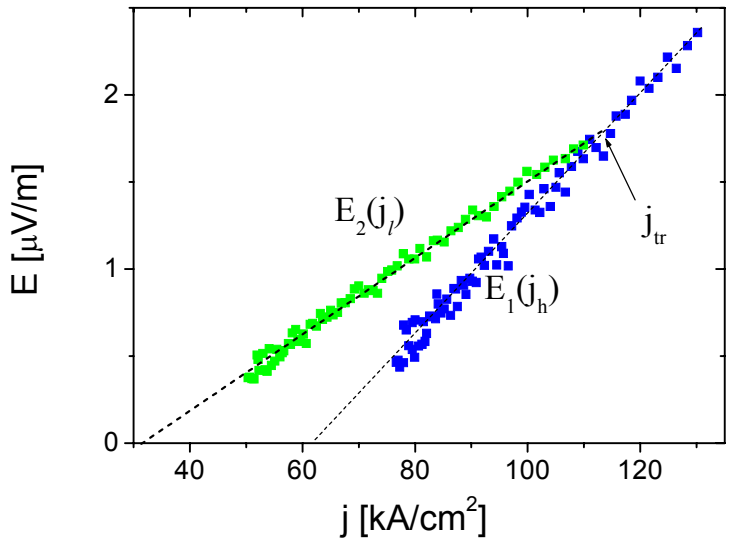

Figure IV-8. Local current-voltage characteristics for disordered phase – $E(j_h)$ taken at x = –290 μm (see Figure IV-5) and ordered phase – $E(j_l)$ taken at x= –130 μm. Dashed lines represent linear fits.

To extract values for critical current density, we note that in our experimental time-window both curves behave rather linearly, enabling extrapolation toward E = 0,

as shown by dashed lines in Figure IV-8, which yield $j_c^h \simeq 62\ kA/cm^2$ and $j_c^l \simeq 31\ kA/cm^2$ for T = 20 K. Thus, the value of critical current density in the high-j phase is approximately *twice* the value for the low-j phase.

We turn now to a discussion of the origin of the intersection point between the $E(j_l)$ and $E(j_h)$ curve at the j_{tr} point. For currents higher than j_{tr} (short times – the break still has not appeared), there is only a single curve describing the $E(j)$ characteristics of both phases; in other words, there is only a single *transient* phase from which the low-j and high-j phase evolve.

Below are attempts to reach conclusions concerning the nature of this transient phase from the form of the $E(j)$ curves. As demonstrated in Figure IV-8, at current densities lower than j_{tr}, the $E(j_l)$ curve breaks and starts to have smaller slope, and the $E(j_h)$ curve is a direct continuation of the transient $E(j)$ curve[7]. This implies that the high-j phase and the transient phase have similar natures, and the low-j phase has a principally *different* nature. One can, therefore, claim that, after the sudden application of a magnetic field, a transient high-j vortex phase is created. The appearance of a break at x_f signifies the nucleation of another low-j phase in the inner part of the sample, and the motion of x_f signifies the low-j phase enhancement.

IV.2.3 Two-dimensional images

On the one-dimensional profiles (Figure IV-5), the point x_f is moving toward the sample edge; therefore, on a 2-D image, x_f must be a point on the *border* between the expanding low-j phase and the retreating high-j phase. To construct the *borderline* between the two phases, we utilize their different relaxation characteristics. We

[7] As a result, for the same current, the electric field E is higher in low-j phase than in the high-j phase, resulting in a developing break in the induction profile.

subtract consecutive 2D induction images and plot the difference. In the low-*j* state, the decay is relatively fast and the differnces are relatively large (bright in our gray scale). The slow decay of the high-*j* state results in a relatively small difference (dark color). Figure IV-9 illustrates a result of such a procedure, showing a clear border between the two phases. This border can be viewed as the front of the growing low-*j* phase. As shown below, in Section IV.4, the growth rate of the ordered phase depends on the local induction. The equi-induction lines are curved in a thin rectangular sample [94]. As a result, the shape of the front of the growing phase, shown in Figure IV-9, is curved.

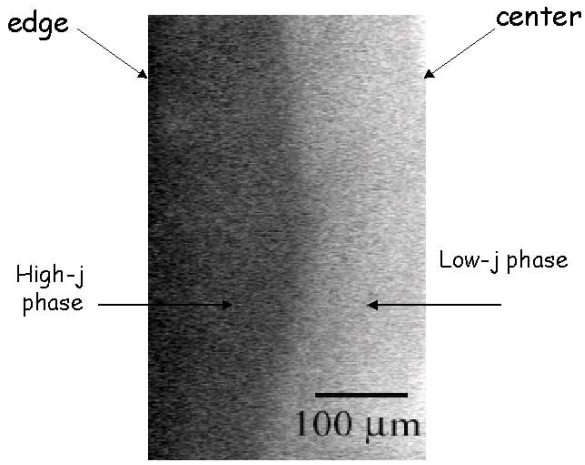

Figure IV-9. Illustration of the border between the two vortex phases, constructed by taking the difference of two consecutive images.

IV.2.4 Non-monotonic motion of the front ($B_a \gtrsim B_{ss}$)

The following describes an experiment done at higher temperature (T = 23 K) on sample S1. Here, due to faster dynamics, we were able to observe another mode of break motion characteristic to applied fields higher than B_{ss}.

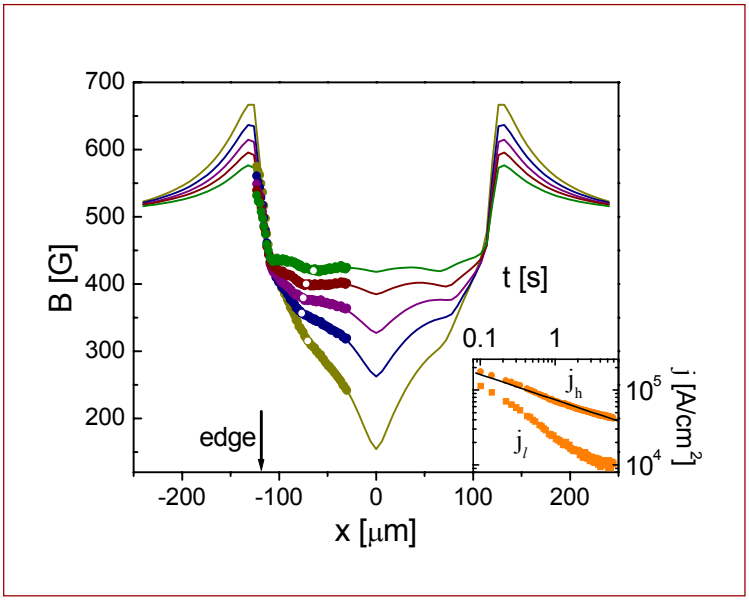

Figure IV-10. Time evolution of the magnetic induction profiles for field H_a = 510 Oe (B_a = 430 G > B_{ss} ≈ 400 G), for sample S1. Profiles shown are measured at t = 0.14, 0.3, 0.66, 1.3, and 5.94 s. Bold circles denote the location x_f of the breaks in the profiles. Solid lines are theoretical fits. Lower inset: Log-log plot of $j_h(t)$ and $j_l(t)$. Solid line: Fit of power law for $j_h(t)$, with an exponent -0.34.

In Figure IV-10, we show the time evolution of the magnetic induction profiles after a step increase of H_a from zero to 510 Oe, corresponding to $B_a > B_{ss}$. Sharp changes in the slope of the profiles (at break points marked by bold circles) are evident. Similar to the previous case, the relaxation on both sides of the break point is governed by different laws, as illustrated in the log-log plot in the inset to Figure IV-10. In Figure IV-10, the intriguing observation is that the motion of the break point is non-monotonic. Initially, it moves toward the edges; however, at some point it changes direction and starts moving backwards, toward the sample center. During this non-monotonic motion, the induction B_f at x_f increases continuously. In Figure IV-11 we summarize the different modes of motion of x_f for sample S1 as plots of B_f *vs* x_f for different values of B_a/B_{ss}. Similar results are also observed in sample S2.

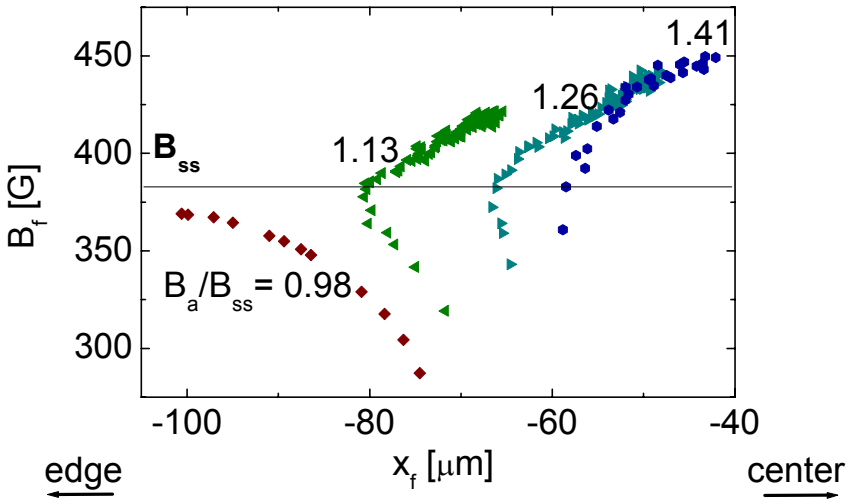

Figure IV-11. The time evolution of B_f vs. x_f for sample S1 at the indicated values of B_a/B_{ss}. x_f is measured from the center.

As already mentioned, the break in the induction profile at x_f (which marks changes in the bulk current density and in the relaxation characteristics) indicates a dynamic coexistence of two distinct vortex phases on both sides of x_f. The identification of these states and the explanation for the different modes of motion of x_f become apparent in considering the following model.

IV.3 Interpretation

The premise of the proposed model is that the *sudden* injection of vortices into the sample, through its non-homogeneous edges, creates a transient-disordered state of the vortex matter. A similar metastable disordered vortex phase, injected by transport current, was assumed by Paltiel *et al*. [95] to explain a number of puzzling observations in $NbSe_2$. This metastable disordered state has been ascribed to surface imperfections and/or surface barriers, which impede the "smooth" entrance of the injected fluxons [95].

On the basis of this premise, all of the observations described above have a simple interpretation. Subsequent to the flux injection and the creation of the transient-disordered state, an ordered vortex state starts to nucleate near the sample center, where the field is minimum. The growth of this state, as dictated by the thermodynamic conditions, leads to the coexistence of two states with different characteristics: an ordered state in the sample interior and a disordered state near the edges. The observed break in the profile at x_f marks the border between these two phases. Consistent with this picture, we observe larger persistent currents and slower relaxation near the edges, indicating a disordered state.

The monotonic motion of x_f toward the edges (Figure IV-5 and the left-hand curve in Figure IV-11) is now well understood. In this case, B_f is smaller than B_{ss}, and the front of the ordered state at x_f progressively moves toward the sample edges, creating an ordered state throughout the entire sample, as dictated by the thermodynamic conditions. When the front reaches the sample edge, the break disappears, indicating that the entire sample is in an ordered state. The non-monotonic behavior of x_f for $B_a > B_{ss}$ (Figure IV-10 and the three right-hand curves in Figure IV-11) can be explained in a similar way. Initially, B_f is smaller than B_{ss}, and, therefore, the ordered state expands toward the edges. However, as B_f approaches B_{ss}, this expansion comes to a halt, as dictated by thermodynamics. Evidently, in the region ($|x| < x_f$) occupied by the ordered phase, the induction increases continuously, due to magnetic relaxation. As a result, the ordered phase starts to retreat, and the disordered phase gradually penetrates into the sample. This is manifested by the movement of the break point x_f toward the sample center. When the break reaches the sample center, it disappears, indicating that the entire sample is in a disordered state. It is important to note that the data of Figure IV-10 and Figure IV-11 indicate that an

ordered state may persist temporarily above B_{ss}, as it takes time for the disordered state to take over. During this time, as the flux creep process continues, the number of vortices in the system increases and, inevitably, the induction B_f at the border between the two phases increases.

IV.4 Growth rate

Inasmuch as it is now clear that the observed phenomena are related to phase dynamics, we show here the results obtained for a key parameter of the front motion – the growth rate $v_f = (dx_f/dt)$.

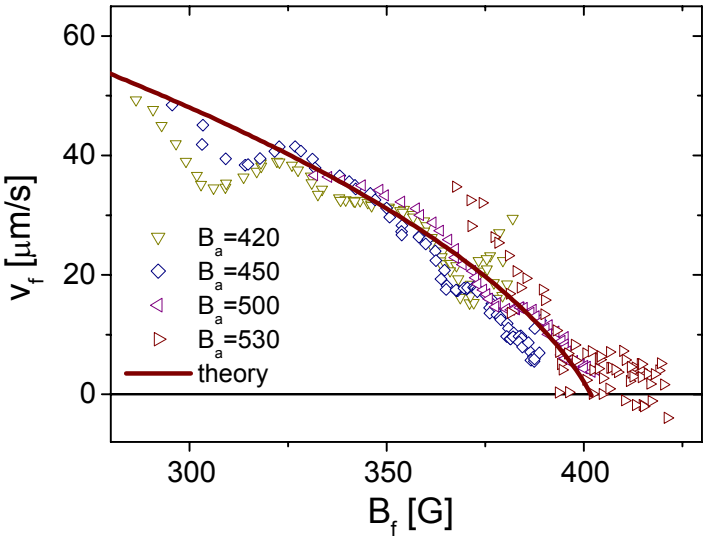

Figure IV-12. v_f *vs.* B_f for indicated applied fields B_a describing the growth of the ordered state. The solid line is an analytical curve obtained in Chapter V.

In Figure IV-12, we show the velocity v_f as a function of the induction B_f at the front, accumulated from different experiments in sample S2, corresponding to the indicated ratios B_a/B_{ss}. Figure IV-12 shows that the velocity decreases monotonically to zero as B_f increases. Moreover, Figure IV-12 demonstrates that the various $v_f(B_f)$ curves converge as B_f increases, indicating that the growth rate of the ordered phase is limited by the induction increase. As B_f approaches B_{ss}, we expect the velocity to

vanish ($B_f \approx 400$ G in Figure IV-12). On the basis of this interpretation, it is possible to understand the absence of traces of the transient-disordered state in the data of Figure IV-2. Inasmuch as B_a in this figure is well below B_{ss}, the lifetime of the transient state is shorter than our time resolution. To observe the transient state, the field must be raised to values closer to B_{ss}.

The growth rate of the thermodynamic disordered state can be characterized by the velocity of the front x_f after the "turning point" in B_f *vs* x_f curves, where the movement of x_f changes direction (i.e., x_f starts moving toward the sample center; see the three right curves in Figure IV-11). Unlike the situation for $B_f < B_{ss}$, where the increase of B_f toward B_{ss} is the main factor limiting the growth of the ordered state, for $B_f > B_{ss}$, the induction increase is in favor of the growth of the disordered state.

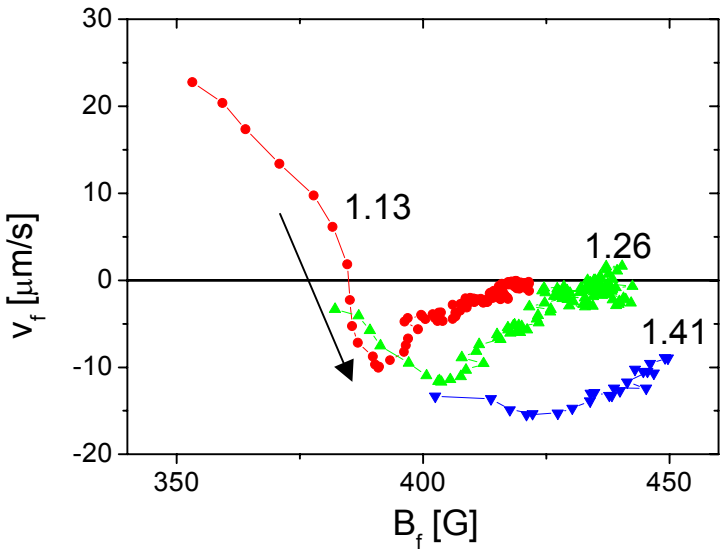

Figure IV-13. v_f *vs.* B_f for the indicated ratios B_a/B_{ss}. Arrow indicates direction of time.

This is the case immediately after v_f changes its sign (B_f crosses B_{ss}); see Figure IV-13. However, a bit later the growth rate of the disordered state starts to decrease,

with time halting the v_f *vs.* B_f curves convergence. Instead, plots of v_f *vs.* $(dB/dt)|_{x=x_f}$ do converge as shown in Figure IV-14.

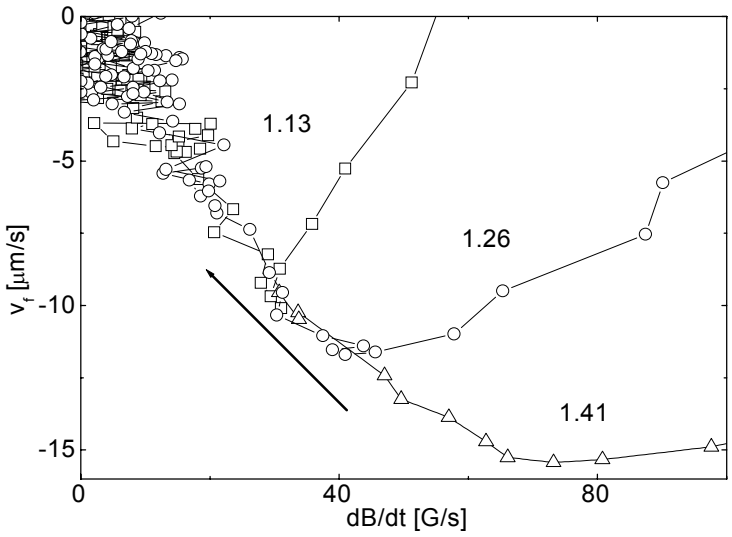

Figure IV-14. v_f ***vs.*** $dB/dt|_{x=xf}$ **for the indicated ratios** B_a/B_{ss}**. Arrow indicates direction of time.**

The possible explanation for this phenomenon is the following. When local B in the ordered phase crosses some characteristic induction B^{**} ([8]), the order-disorder transformation starts to take place in the bulk. In this case, the break is no longer signifying the border between two phases but, rather, the "memory" of this border, and its dynamic is governed by the flux creep.

IV.5 Field-Step-down experiments

In a typical experiment of this type, shown in Figure IV-15, we apply a field of 660 G (significantly larger than B_{ss}) to sample S2 and wait for a long enough time

[8] B^{**} is the upper limit of metastability and, in general, is larger than B_{ss}. For a formal definition of B^{**}, see section V.3.

interval until a thermodynamic disordered state is established in the whole sample. This is manifested by the absence of breaks in the profiles. When this stage is reached, the field is reduced abruptly to 340 Oe (below B_{ss}). As shown in Figure IV-15 by bold circles, in this experiment (as in the FSU experiment), the measured induction profiles exhibit a break point x_f. However, in this case, the break point proceeds from the sample edge toward the sample *center*.

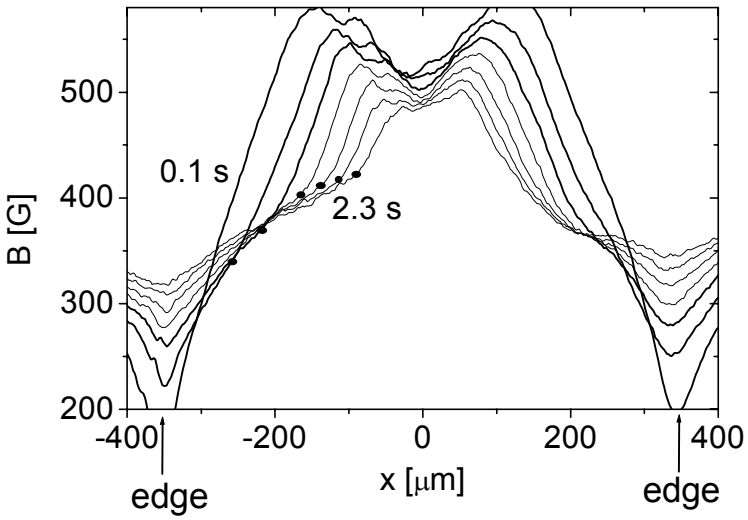

Figure IV-15. Time evolution of the magnetic induction profiles at T = 20 K, after a step decrease of the external magnetic field, from 660 to 340 Oe at t = 0.1, 0.26, 0.46, 0.7, 1.06, 1.54, and 2.3 s. Bold circles indicate the breaks in the profiles.

The results of the FSD experiments can be interpreted in a way similar to the results of the FSU experiments. When the field is reduced, the induction profile is partially inverted, causing part of the profile, near the edges, to drop below B_{ss}. The induction is minimum at the edges; thus, the ordered phase nucleates at the edges and propagates toward the sample center. At the same time, due to magnetic relaxation, the central part of the profile decreases below B_{ss}, allowing the growth of the ordered state throughout the entire sample. Figure IV-16 shows the time dependence of the location of the break x_f for two different external field values, 340 and 240 Oe.

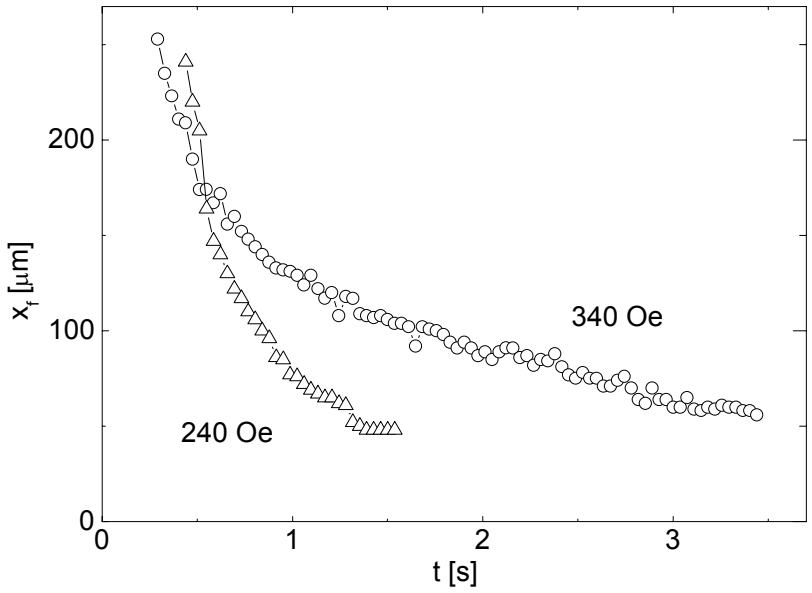

Figure IV-16. Time dependence of the break point x_f for H_a = 340 and 240 Oe.

In the time window of our experiment, we are able to follow the break motion from its appearance (nucleation of the ordered phase) until its end (entire phase is in the ordered phase). The important observation here is that when the external field is lower, this process takes less time, in agreement with the conclusions of section IV.4: growth rate increases with the decrease of induction.

Important information can be extracted also from Figure IV-17, where time dependence of local induction on the front for FSD experiments is shown, compared with the time dependence of B_f, obtained in FSU experiments.

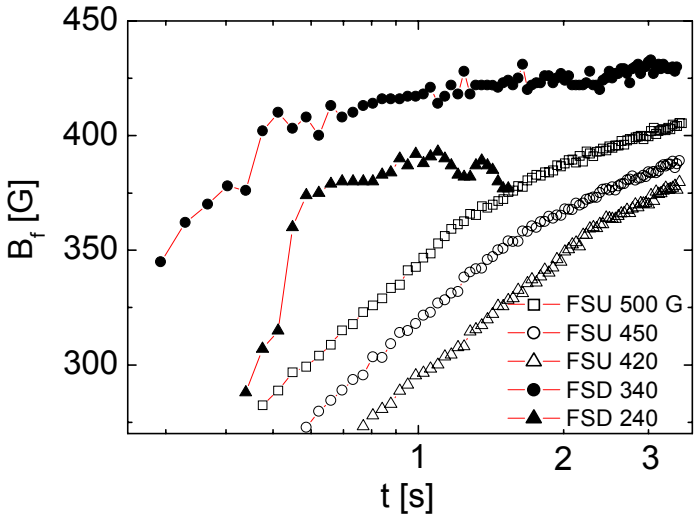

Figure IV-17. Dependence of B_f on time (linear-log scale) for different field steps in FSU (open symbols) and FSD experiments.

The two experiments described above exhibit the growth of the ordered state under different relaxation processes. Nevertheless, in both experiments, B_f increases with time. However, this growth is qualitatively different. Apparently, in FSU experiments, B_f gradually approaches the value of the edge induction, which is determined by external field. In FSD experiments, however, B_f approaches the induction at the center, the value of which decreases continuously with time, due to magnetic relaxation. Thus, the final value of B_f depends on the time of arrival of x_f to the center. In other words, faster relaxation of the induction at the center implies lower saturation values for B_f. That is what we observed for two FSD experiments, the $B_f(t)$ data of which is presented in Figure IV-18. For H_a = 240 Oe (bold triangles), there is a short period of sharp growth of B_f, after which B_f is stabilized around the value of 360 G, which is determined by a competition between break motion and fast flux relaxation. Less then 2 s after quench, the ordered phase invades the entire sample space. In the second experiment, where the external field was reduced to a

higher value of 340 Oe (bold circles), B_f is stabilized, after a short period of sharp growth, near the approximately constant value of about 420 Oe, near B_{ss}.

We also compare, in Figure IV-18, the growth rate $v_f = (dx_f/dt)$, that is, the velocity of the front of the ordered state at x_f for FSU (open symbols) and FSD experiments. Two features are apparent in Figure IV-18. The first is quite expected: The growth velocity decreases with time in all cases. The second observation is the large difference in the growth rate measured in short times in FSU and FSD experiments.

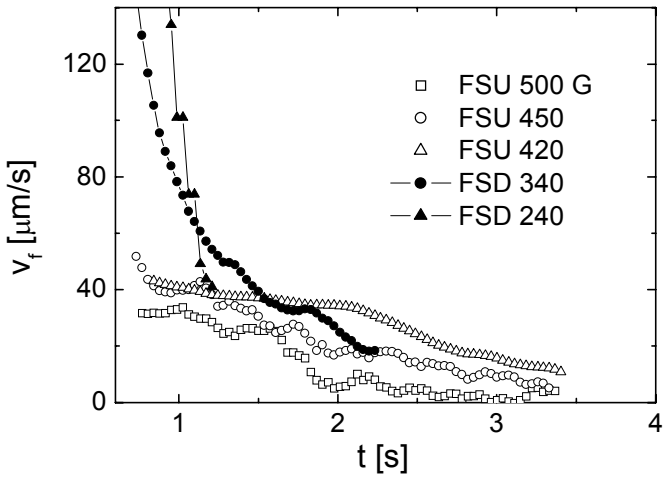

Figure IV-18. Dependence of v_f on time as measured in different FSU (open symbols) and FSD experiments.

In interpreting the latter observation, we note that the initial values of v_f must have received a contribution from the different relaxation conditions in FSU and FSD experiments. In FSU experiments, vortices enter into the sample continuously, causing the induction throughout the entire sample to increase. Thus, B_f can increase, even if $v_f = 0$. In contrast, in the FSD experiments, vortices exit continuously, causing the induction throughout the entire sample to decrease. Thus, B_f cannot increase

unless x_f is moving rapidly toward the center. Deeper understanding of the mechanism of influence of vortex relaxation on the growth rate requires further investigation.

IV.6 Summary and conclusions

Our high temporal resolution magneto-optical system reveals that both the ordered and the disordered thermodynamic vortex states are preceded by the *transient-disordered* vortex state injected into a superconducting sample as a result of an abrupt exposure of the sample to a magnetic field. In the presence of a gradient of the magnetic field (which is usually time-dependent), after sudden application of the magnetic field $B_a \gtrsim B_{ss}$ (FSU experiments), this state is followed by a *local* nucleation of the ordered phase near the sample center (or entering flux front), where the induction is minimal (its value may be much lower than B_{ss}). This causes a *dynamic coexistence* of two vortex phases, possessing different relaxation characteristics $E(j)$, and the appearance of a sharp break in the profile of the magnetic induction. Also, we find that the critical current and the exponent n in $E \propto j^n$ in the ordered phase are much lower than in the disordered phase, resulting in a lower momentary persistent current and faster relaxation in an ordered phase.

The border between the two phases (i.e., the front of the ordered phase) starts moving with a velocity that depends on the local induction, B_f, at the front, and vanishes at B_{ss}. If the applied field B_a is lower than B_{ss}, the ordered phase grows until the whole sample is invaded, and an equilibrium-ordered state is established in the thermodynamic limit. A markedly different behavior is observed for $B_a \gtrsim B_{ss}$. In this case, the initial expansion of the ordered state ceases, and the growth of the thermodynamic disordered state, assisted by the flux entrance, takes over. This is marked by a sharp change in the direction of motion of the boundary between these

two phases. The field at the boundary (when this change of direction occurs) is identified as the thermodynamic transition field B_{ss}.

We find that the velocity of growth of the disordered state first increases as B_f increases (and correspondingly $|B_f - B_{ss}|$ increases) in agreement with the behavior of the velocity of growth of the ordered phase. However, at the later stage, the velocity of the break in the induction starts to decrease (as the creep rate decreases), which is probably the sign of front corruption.

In the experiments where the field is abruptly decreased (FSD) from above to below B_{ss}, the ordered phase nucleates near the sample edge, where the field is minimal, and grows toward the sample center, consistent with the interpretation presented above.

In summary, we described experiments that allow, for the first time, direct observation of nucleation and growth of the vortex solid phases in BSCCO and provided interpretation and insight into the parameters that govern this process.

V Theoretical analysis of nucleation and growth of vortex solid phases

In this chapter, we propose a theoretical approach to explain the nucleation and growth of the quasi-ordered vortex solid phase described in the previous Chapter. Our analysis is based on the Landau-Khalatnikov (LK) time-dependent equation [96]:

$$\frac{\partial \Psi}{\partial t} = -\Gamma \frac{\delta F}{\delta \Psi} \tag{V.1}$$

where Ψ and F are the order parameter and the free energy of the system, and Γ is the Landau-Khalatnikov damping coefficient. In the following, we define the order parameter and the free energy for the vortex system and solve Eq. (V.1) for $B_a \lesssim B_{ss}$. Dynamic coexistence of a stable ordered phase and unstable disordered phase, with a sharp interface between them, is demonstrated. The transformation to the equilibrium state proceeds from the sample center to its edge, by movement of this interface. Our theoretical analysis dictates specific conditions for the creation of a propagating interface and provides the time and spatial scales for this process.

V.1 Order parameter

We define the order parameter of the vortex system in a manner analogous to the definition of the order parameter in order-disorder transitions in atomic solids. [97] In the latter case, the order parameter ρ_q is a set of Fourier components of the atomic density, taken at reciprocal lattice vectors $q = G$. In particular, for an ordered lattice phase, ρ_q = const $\neq 0$ at $q = G$, and for a disordered state $\rho_q = 0$ for all $q \neq 0$. It should be noted that, although the order parameter is an infinite series, in reality it can be replaced by few components (at small G), because the Fourier-image of the effective atomic potential is a strongly decreasing function of q at high G values.

Extending this approach to the vortex order-disorder phase transition, we first note that in small-angle neutron-scattering experiments in BSCCO, [10] Bragg peaks are observed at low temperatures and low fields mainly in the first Brillouin zone; these peaks are smeared for fields larger than B_{ss}. Thus, only one component, ρ_{G_1}, is sufficient to completely describe the order parameter (ρ_{G_1} is now a value of the Fourier component of the *vortex* density at the minimal vector of the reciprocal lattice). To describe the kinetics of the phase transition, we allow the order parameter to be temporally and spatially dependent, $\Psi(r,t) = \rho_{G_1}(r,t)$, assuming that $\Psi(r)$ varies slowly over the inter-vortex distance. The scalar real order parameter $\Psi(r,t)$, so defined, distinguishes between two thermodynamic solid phases of the vortex matter: $\Psi = 0$ for the disordered state and $\Psi = \Psi_0 \neq 0$ for the ordered state.

V.2 Free energy density functional

In the Ginzburg-Landau formalism, the phase transition between the ordered and disordered phases may be described by a free energy density functional F:

$$F = \frac{1}{2} D\left(\nabla\Psi\right)^2 - \frac{1}{2}\alpha\Psi^2 - \frac{1}{3}\beta\Psi^3 + \frac{1}{4}\gamma\Psi^4 \qquad \text{(V.2)}$$

where α, β, γ and D are the Landau coefficients. These coefficients depend on the vortex-vortex and vortex-pinning interactions, and their evaluation requires a microscopic theory that does not yet exist. Note that Eq. (V.2) does not describe the whole free energy of the vortex system, but only the part that is varying through the phase transition, that is, Ψ-dependent.

Inasmuch as the order-disorder vortex phase transition in BSCCO is field driven, we express the parameter α as a function of B:

$$\alpha = \alpha_0(1 - B/B^*) \qquad \text{(V.3)}$$

where B^* is a characteristic field related to the transition field $B_{ss} = B^*\left(1+\frac{2}{9\mu}\right)$ where $\mu = \frac{\alpha_0\gamma}{\beta^2}$. Note that for a second order transition (β = 0), $B_{ss} = B^*$. For a first order phase transition, metastable states of the system are found between B^* and $B^{**} = B^*\left(1+\frac{1}{4\mu}\right)$. For $B < B^*$, the disordered state is unstable, but the ordered state, characterized by

$$\Psi = \Psi_0 = \frac{\beta}{2\gamma}\left[1+\sqrt{1+4\mu\left(1-\frac{B}{B^*}\right)}\right] \qquad \text{(V.4)}$$

is stable. For $B > B^{**}$ the ordered state is unstable, and the disordered state with Ψ = 0 is thermodynamically favorable. All the above results are deduced from the conventional Landau theory for phase transitions [98] by replacing temperature with the induction B. Schematic F(Ψ) dependence for different B is demonstrated in Figure V-1.

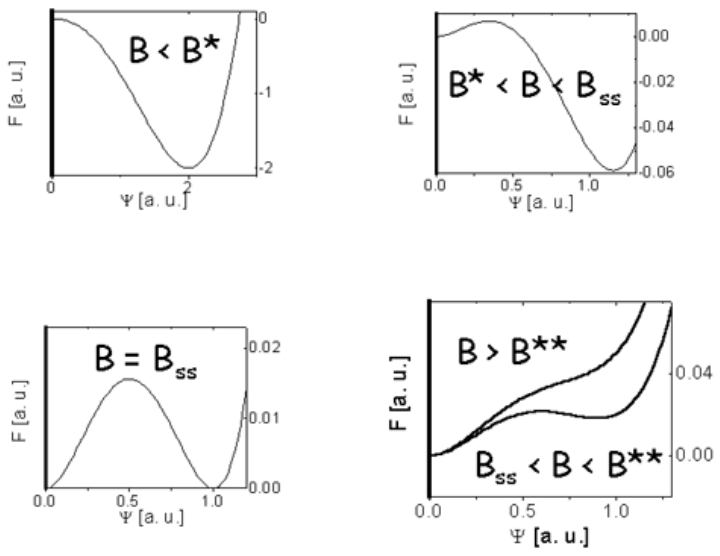

Figure V-1. F(Ψ) dependence for different values of uniform magnetic induction.

V.3 Initial conditions

In solving Eq. (V.1), we assume an initial non-equilibrium disordered vortex state ($\Psi = 0$) caused by the rapid injection of the vortices through non-uniform surface barriers (see Section IV.3). We show that Eq. (V.1) can describe the nucleation and growth of the vortex ordered phase ($\Psi = \Psi_0$).

V.4 Constant gradient

We solve Eq. (V.1) for assuming induction distribution with a constant gradient $\frac{\tilde{B}}{d}$, that is, $B = B_a - \tilde{B}\left(1 - \left|\frac{x}{d}\right|\right)$, typical for hard type-II superconductors, [48, 67], where d is half-width of the sample (see Figure V-2). In this case, Eq. (V.1) can be solved analytically for both the nucleation and growth processes[9].

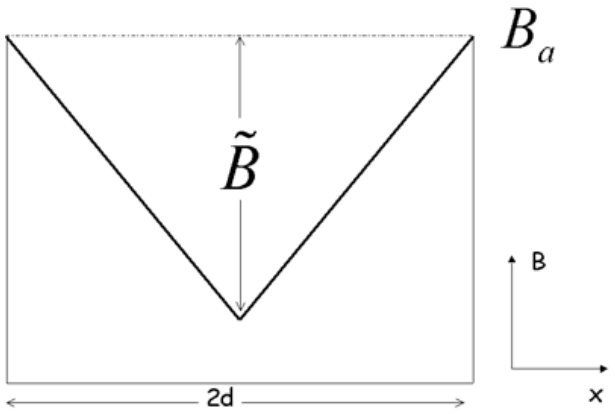

Figure V-2. Schematic drawing of the magnetic induction distribution used in the model.

[9] Without a field gradient, nucleation will occur at random locations and the growth will proceed without the creation of a front, see Refs. [99-101]

V.5 Nucleation process

A solution for the nucleation process, that is, the *initial* growth of the order parameter (Ψ close to zero), is obtained by neglecting nonlinear terms in Eq. (V.1).

$$\frac{1}{\Gamma}\frac{\partial \Psi}{\partial t} = D\frac{\partial^2 \Psi}{\partial x^2} + \alpha_0\left(1 - \frac{B_a - \tilde{B}}{B^*} - \frac{\tilde{B}}{B^* d}x\right)\Psi \tag{V.5}$$

The boundary condition dictated by symmetry is $\left.\frac{d\Psi(x,t)}{dx}\right|_{x=0} = 0$; we also require $\Psi(x,t)$ to be a non-diverging function. The solution of Eq. (V.5) is then:

$$\Psi = \sum_{n=0}^{\infty} A_n e^{\Lambda_n t} Ai\left(\frac{|x|}{x_s} - \zeta_n\right) \tag{V.6}$$

where

$$\Lambda_n = \Gamma\alpha_0\left[1 - \frac{B_a - \tilde{B}}{B^*} - \zeta_n\left(\frac{a_D}{\mu}\right)^{\frac{1}{3}}\left(\frac{\tilde{B}}{B^*}\right)^{\frac{2}{3}}\right], \tag{V.7}$$

Ai is the Airy function, ζ_n = 0.685, 3.9, 7.06, ... are the solutions of $J_{2/3}(\zeta_n) = J_{-2/3}(\zeta_n)$, where J_ν is the Bessel function, and

$$x_s = \left(\frac{DdB^*}{\alpha_0\tilde{B}}\right)^{\frac{1}{3}} = d\left[\frac{a_D B^*}{\mu\tilde{B}}\right]^{\frac{1}{3}} \tag{V.8}$$

Here, $a_D = \frac{D\gamma}{\beta^2 d^2}$ is a dimensionless exchange coefficient. Note that ζ is a constant of order n, growing with increasing n.

It is evident from Eq. (V.6) that only terms with $\Lambda_n > 0$ play a role in the nucleation process. For $B_a - \tilde{B} > B^*$, that is, the entire sample is in a metastable or a stable (but not unstable) state, all Λ_n are negative, implying that the nucleation

process cannot take place. For $B_a = \tilde{B}$, the induction at the center of the sample is zero, and the rate of the nucleation process is maximum. Relation (V.7) shows that the exponent with n = 0 yields the fastest nucleation rate, thus governing the nucleation process. Therefore, this process may be described approximately by the first term in Eq. (V.5). In this approximation, dashed lines in Figure V-3 describe the development of the order parameter during the nucleation process.

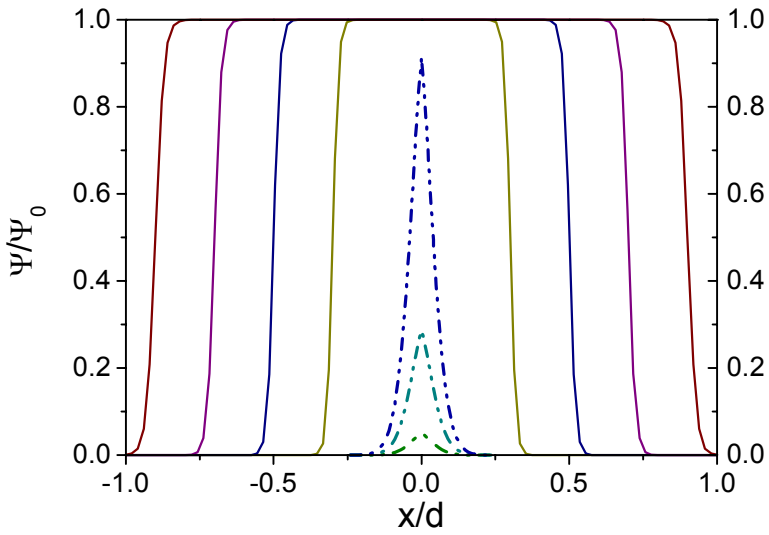

Figure V-3. Nucleation and growth of the order parameter. The nucleation process is demonstrated by the dashed curves, calculated from Eq. (V.6), for $A_n=A_0\delta_{n,0}$ at times $\Lambda_n t$=8.12, 9.86, and 11.02. The solid lines, describing the growth process, are calculated from Eq. (V.11) at different locations x_f/d=0.3, 0.5, 0.7, and 0.9.

Note that the analytical solution (V.5) describes only the first stages of the nucleation process, in which the non-linear terms in Eq. (V.1) may be neglected. This solution ceases to apply when the value of Ψ approaches Ψ_0, that is, after a time period of order Λ_0^{-1}. The width of the ordered domain is then given, approximately, by $w \sim x_s\left(1+\zeta_n\right) \sim x_s$. The condition for appearance of *localized* domain in the sample center may be then obtained from the inequality $x_s << d$ or:

$$\frac{\tilde{B}}{B^*} >> \frac{a_D}{\mu} \quad \Rightarrow \quad \frac{j}{B_{ss}} >> \frac{D}{d^3\left(\alpha_0 + \frac{2}{9}\frac{\beta^2}{\gamma}\right)} \tag{V.9}$$

where $j = \frac{\tilde{B}}{d}$ is a gradient of magnetic induction. If this condition is not satisfied, then homogeneous transformation of the unstable phase takes place. Otherwise, a sharp front will develop, separating between the nucleating ordered phase and the initial unstable disordered phase, as described above. Thus, when the induction gradient is large enough, compared with the B_{ss} value, we expect the appearance of a sharp interface between the growing stable (ordered) phase and the retreating unstable (disordered) phase. There is another important conclusion from Eq. (V.9): If the sample size is reduced, then the growth of the ordered phase is expected to have a crossover from the front-like to homogeneous mechanism.

V.6 Growth process

In describing the *growth* process, that is, the movement of the interface between the ordered and disordered phases, non-linear terms in Eq. (V.1) must be taken into account. We express the linearly varying function $B(x)$ as: $B = B_f + \left(\frac{\tilde{B}}{d}\right)\left[x - x_f\right]$, where $B_f = \left(B_a - \tilde{B}\right) + x_f \tilde{B}/d$ is the induction at the front located at x_f. Equation (V.3) then yields $\frac{\alpha}{\alpha_0} = 1 - \frac{B_f + \frac{\tilde{B}}{d}\left(x - x_f\right)}{B^*}$, and therefore Eq. (V.1) can be written in the reference frame of an observer moving with the front, by introducing a new variable $\xi = x - x_f(t)$ and defining $x_f(t) = x_0 + \int_0^\infty v_f\left(t'\right)dt'$, where

v_f is the time-dependent front velocity and x_0 is a constant. With the new set of independent variables (ξ, B_f), Eq. (V.1) becomes:

$$\frac{v_f}{\Gamma}\left(-\frac{\partial\Psi}{\partial\xi}+\frac{\tilde{B}}{d}\frac{\partial\Psi}{\partial B_f}\right)=D\frac{\partial^2\Psi}{\partial\xi^2}+\alpha_0\left(1-\frac{B_f\left\{x_f(t)\right\}}{B^*}-\frac{\tilde{B}}{B^*d}\xi\right)\Psi+\beta\Psi^2-\gamma\Psi^3 \tag{V.10}$$

One can solve this equation analytically, provided the front width $\Delta << \frac{dB_f}{B^*}$.

In this case, the terms $\frac{v_f}{\Gamma}\frac{\tilde{B}}{d}\frac{\partial\Psi}{\partial B_f}$ and $-\alpha_0\left(\frac{\tilde{B}\xi}{dB^*}\right)\Psi$ may be neglected[10]. The solution of Eq. (V.10) is then [103]:

$$\Psi=\frac{\Psi_0}{1+\exp\left(\frac{x-x_f}{\Delta}\right)} \tag{V.11}$$

where the front width is defined by:

$$\Delta^2=\frac{\Delta_0^2}{2\mu\left(1-B_f/B^*\right)+1+\sqrt{1+4\mu\left(1-B_f/B^*\right)}} \tag{V.12}$$

The front velocity $v_f = dx_f/dt$ is:

$$v_f=v_0\frac{6\mu\left(1-B_f/B^*\right)+1+\sqrt{1+4\mu\left(1-B_f/B^*\right)}}{\sqrt{2\mu\left(1-B_f/B^*\right)+1+\sqrt{1+4\mu\left(1-B_f/B^*\right)}}} \tag{V.13}$$

Here

$$\begin{aligned} v_0&=\Gamma\sqrt{D\beta^2/4\gamma}=\Gamma\alpha_0 d\sqrt{a_D}/2\mu \\ \Delta_0^2&=4D\gamma/\beta^2=4d^2a_D \end{aligned} \tag{V.14}$$

---

[10] These terms are small in the vicinity of the front and therefore unimportant for the calculation of the front properties. For a similar treatment see, e.g., Ref. [102].

and $B_f \equiv B_f(t)$. The solid lines in Figure V-3 show Ψ, Eq. (V.11), for different locations of the front x_f. The evolution of Ψ describes the propagation of the ordered phase.

We discuss here the front velocity v_f (Eq. (V.13)) and the front width Δ, Eq. (V.12). We first note that v_f and Δ do not depend *explicitly* on time or applied field, but they do depend on B_f, the *local* induction at the front. Several important conclusions may be drawn from these equations:

1) As B_f approaches B_{ss} the velocity approaches zero. (The $v_f(B_f)$ dependence is described by the solid line in Figure IV-12.)

2) The motion of the front toward the sample edge is accompanied by an increase of the induction B_f at the front, resulting in a decrease of the velocity with time.

3) The front width Δ decreases with the increase of β, implying that for a "stronger" first-order transition, the front is steeper. Also from Eq. (V.12), it is obvious that the exchange coefficient D causes the front to be smeared. In addition, increasing D and/or the damping coefficient Γ results in an acceleration of the front motion (see Eq. (V.13)).

V.7 Solution of the general case (with flux creep)

Thus far we have demonstrated dynamic coexistence of ordered and transient-disordered vortex phases, with a sharp interface between them, assuming time-independent induction distribution with a constant gradient. In high-temperature superconductors, however, the induction distribution varies significantly with time, due to flux creep. [67] In addition, one may expect different flux creep laws for the different vortex phases. As a result, a break is expected to appear in the induction

profiles. Thus, as we show below, the nucleation of the ordered vortex phase is manifested by the appearance of a break in the induction profiles; the growth of this ordered phase is manifested by movement of the break toward the sample edge (see Chapter IV). The location of the break in the induction profiles is expected to coincide with the location of the moving front of the order parameter.

To demonstrate this scenario, we solved the LK equation (V.1) numerically, allowing for flux creep.

If the inhomogeneous phase transition is considered in the framework of the local driving parameter (magnetic induction) model, where the magnetic induction obeys the Maxwell's equations:

$$\nabla \times \vec{B} = \frac{4\pi}{c}\vec{j} \tag{V.15}$$

and

$$\nabla \times \vec{E} = -\frac{1}{c}\frac{d\vec{B}}{dt} \tag{V.16}$$

The electric field E is induced by the moving vortices; the electric field *vs.* current density dependence ($E(j)$) is assumed to be the unique electrodynamic characteristic describing the distinct vortex phase. It is natural to generalize this dependence to the case of coexisting vortex phases by introducing the $E(j,\Psi/\Psi_0)$ function, which should have the following asymptotes: $E(j,\Psi/\Psi_0=0) = E_1(j)$ and $E(j,\Psi/\Psi_0=1) = E_2(j)$. Without affecting generality, we define the function $E(j,\Psi/\Psi_0)$ to match the asymptotic behavior in the following way:

$$E(j,\Psi) = E_1(j)\left[1-\left(\frac{\Psi}{\Psi_0}\right)^{\nu}\right] + E_2(j)\left(\frac{\Psi}{\Psi_0}\right)^{\nu} \tag{V.17}$$

where ν is a constant of order 1.

We note that the precise form of this function is not essential and has a minor effect on the final result, provided the interface between the two phases is narrow enough.

As before, we assume an initial disordered phase throughout the entire sample, $\Psi(t=0,x) = 0$.

Equations (V.1), (V.3), (V.15), (V.16), and (V.17), in one dimension, define a full set of partial differential equations with four variables: $\Psi(x,t)$, $B(x,t)$, $E(x,t)$ and $j(x,t)$.

To solve this set of equations numerically, we define dimensionless parameters: $b=B/B^*$, $j'=4\pi Jd/(cB^*)$, $x' = x/d$, $t' = t\beta^2\Gamma/\gamma$, and $\Psi' = \frac{\Psi}{\Psi_0(B^{**})} = \frac{2\Psi\gamma}{\beta}$. Eq. (V.1) then becomes:

$$\frac{\partial\Psi'}{\partial t'} = a_D \frac{\partial^2\Psi'}{\partial x'^2} + \mu\left[1-b(x')\right]\Psi' + \frac{1}{2}\Psi'^2 - \frac{1}{3}\Psi'^3 + f'(x',t') \qquad \text{(V.18)}$$

where f and $f' = \frac{2f\gamma}{\beta\alpha_0}$ are a real and dimensionless noise that must be introduced in the numerical solution.

The values of the (dimensionless) parameters used in the numerical calculations are based on experimental measurements. In particular, from the fit of Eq. (V.13) to the experimental data of $v_f(B_f)$ in Figure IV-12, we estimate $\mu = 1.5$; thus, $B_{ss}/B^* = 1.148$ and $B^{**}/B^* = 1.166$ ([11]). A value of 10^{-4} for $a_D = \left[\frac{2\mu v_0}{\Gamma\alpha_0 d}\right]^2$ (see Eq.

[11] Note that this value of μ corresponds to a first-order transition, namely a coefficient before the cubic term in the free energy functional does not vanish ($\beta \neq 0$). As a result $B^* < B_{ss} < B^{**}$, thus

(V.14)) is estimated from the experimental value $v_0 \approx 20\mu m/s$ obtained from the same fit. A value of $\Lambda_0 \sim \Gamma\alpha_0 \approx 10s^{-1}$ is estimated from the time elapsed between switching on the external field and the appearance of a break in the induction profile. A typical value of $d \simeq 300\mu m$ for the sample half width was used. Based on the analysis of magnetic relaxation (see section IV.2.2), we take $E \propto j^n$ with n = 1.9 and n = 3 for ordered and disordered phases, respectively. In addition, a noise level of $f'_{\max} = 10^{-4}$ is assumed.

The system of equations completed by boundary and initial conditions has been solved numerically utilizing an Euler method. The unit space interval was divided into 200 segments, and a time step of 2.5×10^{-3} (in dimensionless units) was used, providing stability for the numerical procedure.

The results of the numerical solution for $B_a/B^* = 1.1$ are shown in Figure V-4. Figure V-4a shows the spatial dependence of the order parameter at different times. The nucleation appears at the sample center at a dimensionless time $t' \sim 10$ after the field is switched on, forming a sharp front that propagates toward the sample edge. Note that the nucleus in Figure V-4a is much wider than that obtained for a constant gradient, see Figure V-3. This is because, at the initial stages of the nucleation (in the case of relaxing magnetic profile), the front of the entering vortices has not reached the sample center before the nucleation has started. The motion of this front toward the sample center, due to magnetic relaxation, continues simultaneously with nucleation process. As a result, the nucleus is smeared between the point at which the nucleation starts and the sample center.

---

allowing for supercooling and superheating effects. The possibility for superheating provides an explanation for the observation of values of B_f larger than B_{ss} (see Section IV.2.4).

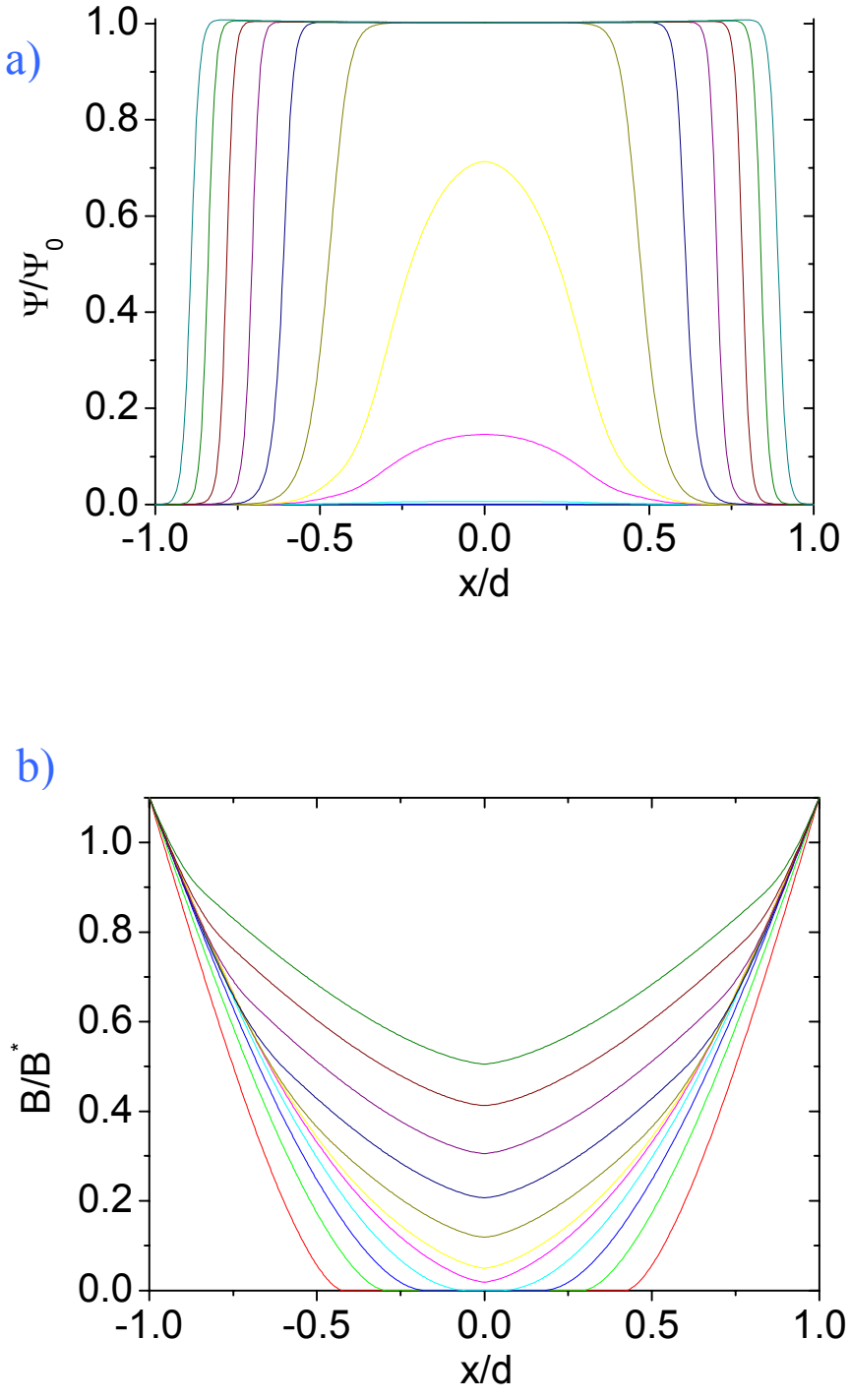

Figure V-4. Order parameter (a) and induction (b) profiles for $E_1(J) = k_1 J \,|\, J \,|^{n_1 - 1}$ and $E_1(J) = k_2 J \,|\, J \,|^{n_2 - 1}$, where n_1=3 and n_2=1.9 (see Section IV.2.2). The profiles are shown for dimensionless times $t' = 2$ (corresponding to maximal gradient), 4, 6, 8, 10, 11, 13, 16, 20, 25, 30.

Consequently, the front of the ordered state and the break in the magnetic induction will appear not in the sample center, but near the point at which nucleation has started. This is in agreement with the experimental result shown in IV.2.2, Figure IV-5. Figure V-4b shows the time evolution of the induction profiles during the nucleation and growth processes. A sharp break in the profiles appears at the location of the front of the order parameter, after the nucleation is completed. As expected, the break in the induction profile and the front of the order parameter move together toward the sample edge[12].

It is important to note that, in a number of early profiles, the sharp break (the interface) in Figure V-4b is found outside the region of phase metastability (i. e. $B_f < B^*$), namely, the moving interface separates unstable (not metastable) and stable vortex phases.

The theoretical predictions described above are confirmed experimentally in BSCCO crystals (see Chapter IV). In particular, a break in the induction profile was recorded following a sudden application of external field of intensity close to the order-disorder transition field B_{ss}. This break moves toward the sample edge at a velocity that depends only on B_f, the value of the induction at the break. Thus, the dependence of v_f on B_f is not affected by magnetic relaxation. The measured velocity, depicted in Figure IV-13, is a function of the induction for different applied fields.

---

[12] The numerical solution does not exhibit breaks in the profiles if the magnetic relaxation is too fast (e.g., $J \sim exp(-t/t_0)$ while $t_0 << 1/\Lambda_0$) or if the critical current is too low ($j_{01} \sim j_{02} \lesssim a_D/\mu$). This is because the requirement for a relatively large gradient, mandatory for the front development, Eq. (V.9), is not satisfied in these cases. Thus, in $YBa_2Cu_3O_{7-\delta}$, for which $\tilde{B} << B_{ss} \sim B^*$, a homogeneous phase transformation is expected rather than front propagation.

The analytical curve, Eq. (V.13), depicted by a solid line in this figure, is in good agreement with the experimental results. The results of $v_f(B_f)$, obtained in the numerical calculations for different applied fields B_a (as well as for different magnetic relaxation rates), are shown in Figure V-5.

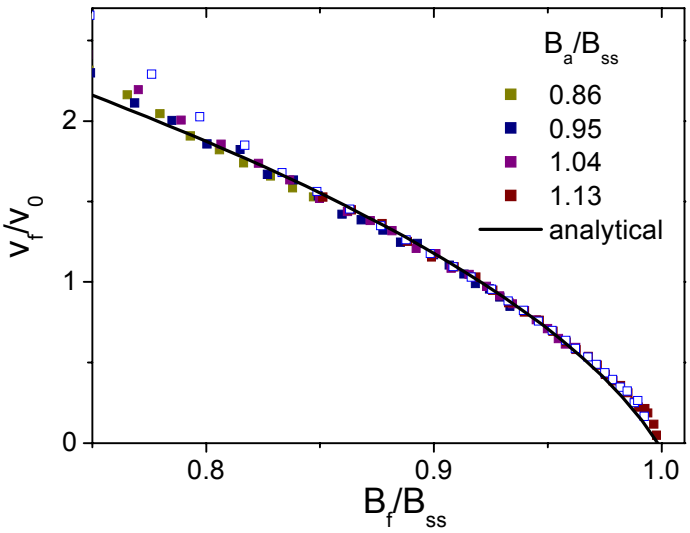

Figure V-5. $v_f(B_f)$ curves from numerical calculations for different applied fields (symbols), together with the analytical solution (solid curve).

These curves converge after short transient period of time corresponding to a nucleation and front establishment, with the analytical curve obtained without taking into account magnetic relaxation.

Note that two velocities govern the vortex dynamics in the process of the phase transformation: the interface velocity v_f, and the flux velocity, v_F, due to creep. The latter may erode the interface if the ratio $\varepsilon = \Delta / v_F \tau_{ord}$ is small. (Here Δ is the interface thickness and $\tau_{ord} \sim 1/\Gamma\alpha_0$ is the accommodation time for the bundle of vortices that found themselves in a phase with another symmetry, adapting to a new environment.) It immediately reads that our theory is correct under condition

$v_F << 4\mu v_f$, implying that in the vicinity of $B_f \sim B_{ss}$ (where $v_f \to 0$), our theory is not valid. We estimate the width of this vicinity by substituting a typical fluxon velocity, of 10 μm/s. We thus conclude that our theory may be applied in the whole induction range, except a very narrow range in the vicinity of B_{ss}, for which $v_f \lesssim 2$ μm/s (see Figure IV-12).

Another important observation is that, as in the experiment, the break appears not exactly in the center (see Figure IV-5). This happens because the nucleation of the ordered phase starts when the vortices have not yet penetrated the sample fully. Then the nucleation starts near the momentary position of the propagating flux front.

V.8 Dynamic fishtail

In this Section, we show that our theoretical approach based on the LK dynamic equation is also capable of explaining the intriguing issue of the time dependence of the second peak anomaly. [30, 67, 104]

Figure V-6 (taken from Ref. [104]) demonstrates that the location and form of the features related to the second peak anomaly may vary with time. This led to the concept of the dynamic "fishtail," relating the anomaly to a complicated relaxation characteristic associated with a collective creep [8, 105] (see Introduction to Chapter III). However, recent measurements of sharp "fishtail" [11] and other works, including ours (see Chapter III), supported the possibility of the phase transition scenario. This requires a new explanation for the fact that the features of the magnetization curve related to this transition are time dependent.

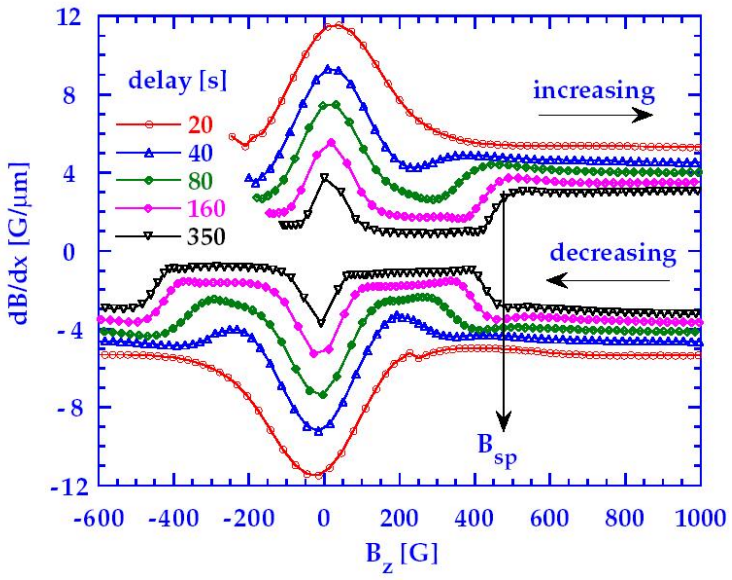

Figure V-6. Magnetization hysteresis loop for different time windows measured in BSCCO taken from Ref. [104]. It is evident that there is no "fishtail" anomaly at short time windows. Moreover, after it appears the onset of the second peak moves with time toward higher fields.

Our theoretical approach gives a natural explanation to the dynamics of the features of the second peak anomaly. We performed a numerical calculation similar to that of Figure V-4 for different applied fields (H) and extracted the global magnetic moment, as well as the local gradient of magnetic induction (proportional to local current density). The results are shown in Figure V-7.

Similar to the experimental results of Figure V-6, the onset of the second peak anomaly is not observed at short times. In the framework of our model, this is expected, because at short times, immediately after field application, a transient-disordered phase appears. This transient-disordered state is initially the only phase present in the whole range of fields.

At later times, the ordered state starts to nucleate near the center of the sample. This nucleation occurs earlier for lower induction values (Eq. (V.7)), explaining why the dip in the magnetization curves starts to develop at lower fields

and then moves toward higher fields, causing a movement of the onset of the second peak.

Note that in the local curves of *dB/dx vs B* (Figure V-6 and Figure V-7b) the sharp growth of the absolute value of *dB/dx* occurs when the front of the growing ordered phase passes through the location probed. This growth is smoother in the experimental curve (Figure V-6), because the gradient is calculated as the difference between two values of local induction measured at different Hall probe array elements (see Chapter II). Therefore, the gradient is averaged on the length scale of this macroscopic distance.

At long times, B_{on} approaches B_{ss}. This is because the growth of the ordered phase is prohibited for local induction values larger than B_{ss}. It is important to distinguish between measurements where the external field is raised sharply and then the system is allowed to relax, and measurements with constant sweep rate. In the latter, if the rate is decreased, B_{on} may increase up to B^{**}.

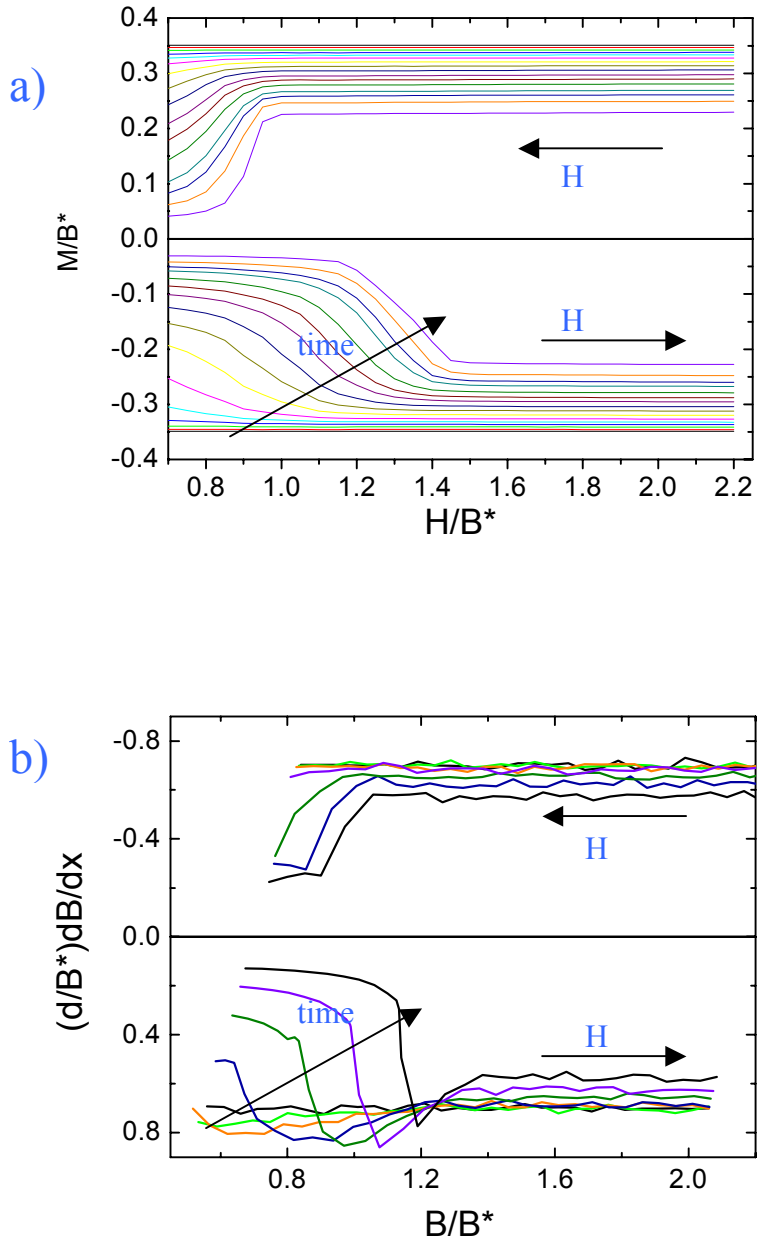

Figure V-7. Numerical calculation of a) global *M*(*H*) curve and b) local *dB/dx* curve at *x/d*=0.8, for different time windows. Arrows signify the direction of time and external field in the experiment.

V.9 Summary and conclusions

In this chapter, we introduced a novel approach to analyzing vortex dynamics associated with the solid-solid vortex phase transition. We demonstrated that the

Landau-Khalatnikov dynamic equation provides a description of the nucleation and growth processes of the vortex quasi-ordered phase. We derived analytical expressions for the parameters, describing these processes for induction distribution with a constant gradient. Our analytical expression for the front velocity fits well the experimental results with a non-zero value of a coefficient before the cubic term in the free energy functional. The non-zero value of this coefficient suggests the vortex solid-solid phase transition is of a first-order nature.

We also showed that, for a high enough gradient (for instance, BSCCO at relatively low temperatures) of the induction, the vortex ordered phase is nucleated locally near the sample center (or near the entering flux front), where the induction is minimal and propagates in a front-like manner, even if the induction corresponds to a non-stable region of the phase diagram. For relatively low gradients (e. g., in YBCO or in BSCCO at high temperatures), the development of the ordered phase is homogeneous, rather than front like. We also predicted that reduction of the sample size would cause a crossover from a front-like to a homogeneous growth.

An interesting by-product of this work is the explanation of the "dynamic fishtail". We showed that the onset of the second peak is a direct consequence of the coexistence of different vortex solid phases, and the dynamics of the onset is dictated by the dynamics of the vortex ordered phase formation. The onset in the infinite time limit is approaching B_{ss}.

VI Summary and conclusions

This work describes a comprehensive study of the vortex solid-solid transition in high-temperature superconductors. We investigated the nature of the solid vortex phases, the phase transition between them, and the process of their formation. The main achievements of this work are summarized below.

Hall-probe measurements of the anomalous second magnetization peak ("fishtail") in $Nd_{1.85}Ce_{0.15}CuO_{4-\delta}$ (NCCO), detwinned $YBa_2Cu_3O_{7-\delta}$ (YBCO), and $Bi_{1.6}Pb_{0.4}Sr_2CaCu_2O_{8+\delta}$ (Pb-BSCCO) - materials with strongly different values of critical temperature T_c and anisotropy ε - indicate the existence of a solid-solid vortex phase transition similar to that observed earlier in $Bi_2Sr_2CaCu_2O_{8+\delta}$ (BSCCO). We identified the transition induction B_{ss} in these materials by employing local magnetic measurements of induction *vs.* field, temperature, and time. In YBCO, for example, the transition was assigned to a pronounced kink in the magnetization *(m vs. H)* curves, observed for the first time in this work. The location of this kink in the (*B,T*) phase diagram of YBCO coincides with a kink in magnetization *vs.* temperature (*m vs. T*) curves and a minimum in the relaxation rate. The transition induction is not moving with time, in contrast to the behavior observed for another characteristic field, B_p, the field of the second peak.

Although the temperature dependence of the transition lines $B_{ss}(T)$ in different materials is qualitatively different, we succeeded in describing these dependences by the same model: the model of disorder-induced transition. We showed that the factors responsible for these qualitative differences are: the critical temperature T_c, pinning parameter γ, anisotropy ε, penetration depth λ, coherence length ξ, interlayer distance s, and the pinning mechanism (δl or δT_c).

We found, in particular, that in the temperature range in which the thermal energy is small, compared with pinning and elastic energies, B_{ss} dependence on temperature is implicit – $B_{ss}(T) = B_{ss}(\xi(T))$ – and $B_{ss}(\xi)$ dependence is unique for a given type of pinning. In NCCO, for example, for which T_c is lower than the depinning temperature T_{dp}, $B_{ss}(T)$ decreases monotonously in the whole temperature range, up to T_c. In YBCO and Pb-BSCCO, in which T_c is higher than T_{dp}, $B_{ss}(T)$ increases drastically, starting from $T = T_{dp}$, due to the sharp weakening of the pinning energy. The type of pinning mechanism determines the dependence of B_{ss} on ξ. This is especially important for $T < T_{dp}$, where the strong increase in B_{ss} caused by thermal depinning does not interfere. If the pinning is of δT_c-type then, for $T < T_{dp}$, $B_{ss}(T)$ is a decreasing function of temperature. If the pinning is of δl-type, B_{ss} increases with temperature. This gives an effective tool for determination of pinning mechanism in HTS materials. In particular, we identified δT_c-pinning in NCCO and Pb-BSCCO, and δl-pinning in YBCO.

To summarize this part of the work, we showed how to implement the disorder-induced transition model in analyzing the temperature dependence of the solid-solid transition in HTS materials. We also showed that it is possible to utilize the behavior of the transition line to extract valuable information, such as the type of microscopic pinning mechanism. Our approach has been adopted by other authors in analyzing the vortex solid-solid transition in other HTS, associating the second peak anomaly with a vortex disorder-induced transition. We, therefore, conclude that the disorder-induced transition is a general phenomenon responsible for the second peak anomaly in most of the HTS.

In the second part of this work we performed a pioneering study of the process of formation of the solid vortex phases, above and below the vortex solid-solid

transition line B_{ss}. Our experiments allowed, for the first time, observation of the *transient-disordered* vortex state in BSCCO. This state is created after a sudden application of magnetic field, due to rapid injection of vortices through the surface. Using our high temporal resolution magneto-optical system, we observed the nucleation of the ordered phase and followed the growth of the equilibrium ordered and disordered vortex phases. We characterized these processes both experimentally and theoretically. In particular, we found that the velocity of the front of the growing ordered phase depends on the local induction at the front and goes to zero as the value of this induction approaches B_{ss}. This finding allows a precise determination of B_{ss}.

To describe the observed process of nucleation and growth of the solid vortex phases, we developed a theoretical approach, based on the Landau-Khalatnikov (LK) dynamic equation. We showed that this process can be described by the dynamics of a scalar order parameter, conjugate to the magnetic characteristics of the vortex matter. On the basis of this analysis, we derived analytical expressions for the parameters describing the nucleation and growth of the ordered vortex phase.

Our analysis also provides conditions for front-like growth of the equilibrium vortex phase. We found that, for a high enough induction gradient, the vortex ordered phase is nucleated locally near the sample center, where the induction is minimal, and propagates in a front-like manner. For a relatively small gradient, the growth of the ordered phase is homogeneous. We also predicted that reduction of the sample size would cause a crossover from a front-like to a homogeneous growth. In addition, our analysis is capable of explaining the experimentally measured time evolution of the onset of the second peak. We found that the "dynamic fishtail" behavior is a direct consequence of coexistence of different vortex solid phases, and the dynamics of the

onset is dictated by the dynamics of the vortex ordered phase formation. The onset in the infinite time limit approaches the B_{ss} value.

The success of this theoretical analysis, based on the LK dynamic equation for the order parameter, provides additional evidence for the phase transition origin of the "fishtail" in BSCCO. Moreover, our analytical expression for the front velocity fits well the experimental results for the field dependence of the front velocity with a non-zero cubic term in the free energy functional, thus indicating the *first-order nature* of the solid-solid phase transition.

The results presented here provide insight into the nature of the solid vortex phases and the process of their formation. At the same time, this work opens a door for future studies, such as investigation of the influence of different correlated and uncorrelated disorders on the solid-solid transition, conditions for the appearance of the transient-disordered state, influence of transport current on the process of nucleation and growth, and effects of temperature and geometry on nucleation and growth of equilibrium vortex phases.

Appendix. List of publications – D. Giller

DG1. Investigation of flux creep in high-T_c superconductors using Hall-sensor array.

Y. Abulafia, **D. Giller**, Y. Wolfus, A. Shaulov, Y. Yeshurun, D. Majer, E. Zeldov, J. L. Peng, and R. L. Greene,

J. Appl. Phys. **81**, 4944 (1997).

DG2. Extraction of current density distribution from local magnetic measurements.

Y. Abulafia, Y. Wolfus, A. Shaulov, R. Prozorov, **D. Giller**, Y. Yeshurun,

Physica C **282-287**, 2225 (1997).

DG3. Local magnetic relaxation in $Nd_{1.85}Ce_{0.15}CuO_{4-\delta}$ crystals.

D. Giller, Y. Abulafia, R. Prozorov, Y. Wolfus, A. Shaulov, Y. Yeshurun, D. Majer, E. Zeldov, J. L. Peng, R. L. Greene,

Physica C **282-287**, 2209 (1997).

DG4. Disorder-induced transition to entangled vortex solid in Nd-Ce-Cu-O crystal.

D. Giller, A. Shaulov, R. Prozorov, Y. Abulafia, Y. Wolfus, L. Burlachkov, Y. Yeshurun, E. Zeldov, V. M. Vinokur, J. L. Peng, and R. L. Greene,

Phys. Rev. Lett. **79**, 2542 (1997).

DG5. Local voltage-current characteristics in high-Tc superconductors.

D. Giller, Y. Abulafia, R. Prozorov, Y. Wolfus, A. Shaulov, and Y. Yeshurun,

Phys. Rev. B (Rapid Communication) **57**, R14080 (1998).

DG6. Collective flux creep: beyond the logarithmic solution.

L. Burlachkov, **D. Giller**, and R. Prozorov,

Phys. Rev. B **58**, 15067 (1998).

DG7. Self-organization of vortices in type-II superconductors during magnetic relaxation.

R. Prozorov and **D. Giller**,

Phys. Rev. B **59**, 14687 (1999).

DG8. Vortex solid-solid phase transition in untwinned $YBa_2Cu_3O_{7-\delta}$ crystal.

D. Giller, A. Shaulov, Y. Yeshurun, J. Giapintzakis,

Phys. Rev. B **60,** 106 (1999).

DG9. Distribution of induction, electric field, and current density, in thin $YBa_2Cu_3O_{7-\delta}$ films carrying transport current.

E. Sheriff, **D. Giller**, Y. Radziner, A. Shaulov, Y. Schlesinger, and Y. Yeshurun,

J. Low Temp. Phys. **117**, 693 (1999).

DG10. Anomalies in the temperature dependence of the local magnetization in Y-Ba-Cu-O and Nd-Ce-Cu-O crystals.

D. Giller, A. Shaulov, and Y. Yeshurun,

J. Low Temp. Phys. **117**, 1417 (1999).

DG11. Local magnetic characterization of superconductors based on magneto-optics and hall-probe array techniques.

Y. Yeshurun, A. Shaulov, and **D. Giller,**

In Proceedings to FIM99 conference, Stockholm, August 12-15, 1999.

DG12. High temporal resolution magneto-optical study of the vortex solid-solid transition in $Bi_2Sr_2CaCu_2O_8$ crystal.

D. Giller, W. Wolfus, A. Shaulov, and Y. Yeshurun,

Physica B **284-8**, 699 (2000).

DG13. Disorder-induced vortex phase transition in untwinned $YBa_2Cu_3O_{7-\delta}$ crystal.

D. Giller, J. Giapintzakis, A. Shaulov, and Y. Yeshurun,

Physica B **284-8**, 697 (2000).

DG14. Determination of the microscopic pinning mechanism in high-temperature superconductors.

D. Giller, A. Shaulov, and Y. Yeshurun,

Physica B **284-8**, 687 (2000).

DG15. Transient vortex states in $Bi_2Sr_2CaCu_2O_{8+\delta}$ crystals.

D. Giller, A. Shaulov, T. Tamegai, and Y. Yeshurun,

Phys. Rev. Lett. **84**, 3698 (2000).

DG16. Metastable vortex states in $YBa_2Cu_3O_{7-\delta}$ crystal.

Y. Radzyner, S. B. Roy, **D. Giller**, Y. Wolfus, A. Shaulov, P. Chaddah, and Y. Yeshurun.

Phys. Rev. B **61**, 14362 (2000).

DG17. Vortex solid-solid transition in $Bi_{1.6}Pb_{0.4}Sr_2CaCu_2O_{8+\delta}$.

M. Baziljevich, **D. Giller**, M. McElfresh, Y. Abulafia, Y. Radzyner, J. Schneck, T. H. Johansen, and Y. Yeshurun.

Phys. Rev. B **62**, 4058 (2000).

DG18. Nucleation and growth of the quasi-ordered vortex phase in Bi_2 $Sr_2CaCu_2O_{8+\delta}$.

D. Giller, A. Shaulov, L. Dorosinskii, T. Tamegai, and Y. Yeshurun,

Physica C **341-348**, 987 (2000).

DG19 Magneto-optical imaging of transient vortex states in $Bi_2Sr_2CaCu_2O_{8+\delta}$ crystals.

D. Giller, A. Shaulov, L. Dorosinskii, T. Tamegai, and Y. Yeshurun,

Physica C **341-348**, 1089 (2000).

DG20. Crystallization of the ordered vortex phase in high-temperature superconductors.

D. Giller, B. Ya. Shapiro, I. Shapiro, A. Shaulov, and Y. Yeshurun,

Phys. Rev. B (Rapid Communication) 63, 220502 (2001).

DG21. Magneto-optical imaging of transient vortex states in superconductors.

D. Giller, B. Kalisky, A. Shaulov, T. Tamegai, Y. Yeshurun,

J. Appl. Phys. 89, 7481 (2001).

DG22. Possibility of Kauzmann points in the vortex matter phase diagram of single crystal $YBa_2Cu_3O_{7-\delta}$.

S. B. Roy, Y. Radzyner, **D. Giller**, Y. Wolfus, A. Shaulov, P. Chaddah, and Y. Yeshurun,

Phys. Rev. B, submitted.

References

1. J. G. Bednorz and K. A. Muller, Z. Phys. B **64,** 189 (1986).
2. M. K. Wu, J. R. Ashburn, C. J. Torng, P. H. Hor, R. L. Meng, L. Gao, Z. J. Huang, Y. Q. Wang, and C. W. Chu, Phys. Rev. Lett. **58,** 901 (1987).
3. Y. Hidaka and M. Suzuki, Nature **338,** 635 (1989).
4. A. Schilling, M. Cantoni, J. D. Guo, and H. R. Ott, Nature **363,** 56 (1993).
5. A. A. Abrikosov, Zh. Eksp. Teor. Fiz. **32,** 1442 (1957).
6. W. H. Kleiner, L. M. Roth, and S. H. Autler, Phys. Rev. A **133,** 1226 (1964).
7. U. Essmann, *Visualization of the mixed state of Type II superconductors*, in Proceedings of "Elektrotechnicky Casopis" (Czechoslovakia, 1970).
8. G. Blatter, M. V. Feigelman, V. B. Geshkenbein, A. I. Larkin, and V. M. Vinokur, Rev. Mod. Phys. **66,** 1125 (1994).
9. E. H. Brandt, Rep. Prog. Phys. **58,** 1465 (1995).
10. R. Cubitt, E. M. Forgan, G. Yang, S. L. Lee, D. M. Paul, H. A. Mook, M. Yethiraj, P. H. Kes, T. W. Li, A. A. Menovsky, Z. Tarnawski, and K. Mortensen, Nature **365,** 407 (1993).
11. B. Khaykovich, E. Zeldov, D. Majer, T. W. Li, P. H. Kes, and M. Konczykowski, Phys. Rev. Lett. **76,** 2555 (1996).
12. R. Liang, D. A. Bonn, and W. N. Hardy, Phys. Rev. Lett. **76,** 835 (1995).
13. A. Schilling, R. A. Fisher, N. E. Phillips, U. Welp, D. Dasgupta, W. K. Kwok, and G. W. Crabtree, Nature **382,** 791 (1996).
14. T. Giamarchi and P. L. Doussal, Phys. Rev. Lett. **72,** 1530 (1994).
15. D. Ertas and D. R. Nelson, Physica C **272,** 79 (1996).
16. V. Vinokur, B. Khaykovich, E. Zeldov, M. Konczykowski, R. A. Doyle, and P. H. Kes, Physica C **295,** 209 (1998).
17. A. E. Koshelev and V. Vinokur, Phys. Rev. B **57,** 8026 (1998).
18. T. Giamarchi and P. L. Doussal, Phys. Rev. B **55,** 6577 (1997).
19. J. Kierfeld, Physica C **300,** 171 (1998).
20. M. Daeumling, J. M. Seuntjens, and D. C. Larbalestier, Nature **346,** 332 (1990).
21. L. Klein, E. R. Yacoby, Y. Yeshurun, A. Erb, G. Muller-Vogt, V. Breit, and H. Wuehl, Phys. Rev. B **49,** 4403 (1994).
22. L. Krusin-Elbaum, L. Civale, V. M. Vinokur, and F. Holtzberg, Phys. Rev. Lett **69,** 2280 (1992).
23. Y. V. Bugoslavsky, A. L. Ivanov, A. A. Minakov, and S. I. Vasyurin, Physica C **233,** 67 (1994).

24. V. N. Kopylov, A. E. Koshelev, I. F. Schegolev, and T. G. Togonidze, Physica C **170,** 291 (1990).

25. V. Hardy, A. Wahl, A. Ruyter, A. Maignan, C. Martin, L. Coudrier, J. Provost, and C. Simon, Physica C (Netherlands) **232,** 347 (1994).

26. A. Maignan, S. N. Putilin, V. Hardy, C. Simon, and B. Raveau, Physica C (Netherlands) **266,** 173 (1996).

27. S. B. Roy and P. Chaddah, Physica C **279,** 1 (1997).

28. S. Bhattacharya and M. J. Higgins, Phys. Rev. Lett. **70,** 2617 (1993).

29. R. Yoshizaki *et al*., Physica C **225,** 299 (1994).

30. Y. Yeshurun, N. Bontemps, L. Burlachkov, and A. Kapitulnik, Phys. Rev. B **49,** 1548 (1994).

31. B. Rosenstein and A. Knigavko, Phys. Rev. Lett. **83,** 844 (1999).

32. T. Tamegai, Y. Iye, I. Oguro, and K. Kishio, Physica C **213,** 33 (1993).

33. M. Konczykowski, F. Holtzberg, and P. Leja, Supercond. Sci. Tech. **4,** S33 (1991).

34. A. M. Chang, H. D. Hallen, L. Harriott, H. F. Hess, H. L. Kao, J. Kwo, R. E. Miller, R. Wolfe, J. van der Ziel, and T. Y. Chang, Appl. Phys. Lett. **61,** 1974 (1992).

35. D. A. Brawner and N. P. Ong, J. Appl. Phys. **73,** 3890 (1993).

36. Y. Abulafia, A. Shaulov, Y. Wolfus, R. Prozorov, L. Burlachkov, Y. Yeshurun, D. Majer, E. Zeldov, and V. M. Vinokur, Phys. Rev. Lett. **75,** 2404 (1995).

37. E. Zeldov, D. Majer, M. Konczykowski, A. I. Lrkin, V. M. Vinokur, V. B. Geshkenbein, N. Chikumoto, and H. Shtrikman, Europh. Lett. **30,** 367 (1995).

38. Y. Abulafia, A. Shaulov, Y. Wolfus, R. Prozorov, L. Burlachkov, Y. Yeshurun, D. Majer, E. Zeldov, and V. M. Vinokur, *Investigation of flux creep in superconductors using Hall-probe array*, in Proceedings of "Coherence in High-Tc Superconductors" (Tel-Aviv, Israel, 1995).

39. V. K. Vlasko-Vlasov, M. V. Indenbom, V. I. Nikitenko, Y. A. Osip'yan, A. A. Polyanskii, and R. Prozorov, Superconductivity - Physics, Chemistry, Technique (SPCT) **3,** S50 (1990).

40. V. K. Vlasko-Vlasov, M. V. Indenbom, V. I. Nikitenko, A. A. Polyanskii, R. Prozorov, I. V. Grekhov, L. A. Delimova, I. A. Liniichuk, A. V. Antonov, and M. Y. Gusev, Superconductivity - Physics, Chemistry, Technique (SPCT) **5,** 1582 (1992).

41. V. K. Vlasko-Vlasov, L. A. Dorosinskii, M. V. Indenbom, V. I. Nikitenko, A. A. Polyanskii, and R. Prozorov, Superconductivity - Physics, Chemistry, Technique (SPCT) **6,** 555 (1993).

42. M. V. Indenbom, A. Forkl, B. Ludescher, H. Kronmuller, H. U. Habermeier, B. Leibold, G. DAnna, T. W. Li, P. H. Kes, and A. A. Menovsky, Physica C **226,** 325 (1995).

43. M. V. Indenbom, C. J. van der Beek, V. Berseth, W. Benoit, G. D Anna, A. Erb, E. Walker, and R. Flukiger, Nature **385,** 702 (1997).

44. M. R. Koblischka and R. J. Wijngaarden, Supercond. Sci. Technol. **8,** 199 (1995).

45. T. Schuster, H. Kuhn, M. V. Indenbom, M. Leghissa, M. Kraus, and M. Konczykowski, Phys. Rev. B **51,** 16358 (1995).

46. Y. Abulafia, *Mapping and characterization of local magnetic properties of high-temperature superconductors,* Ph. D. Thesis (Bar-Ilan University, Ramat-Gan, 1997).

47. A. M. Campbell and J. E. Evetts, *Critical currents in superconductors* (Taylor & Francis Ltd., London, 1972).

48. C. P. Bean, Phys. Rev. Lett. **8,** 250 (1962).

49. H. Ullmaier, *Irreversible properties of type-II superconductors* (Springer-Verlag, Berlin, Heidelberg, New York, 1975).

50. C. P. Bean, Reviews of Modern Physics **36,** 31 (1964).

51. M. Konczykowski, L. Burlachkov, Y. Yeshurun, and F. Holtzberg, Phys. Rev. B **43,** 13707 (1991).

52. M. Konczykowski, L. Burlachkov, Y. Yeshurun, and F. Holtzberg, Physica C **194,** 155 (1992).

53. N. Chikumoto, M. Konczykowski, N. Motohira, and A. P. Malozemoff, Phys. Rev. Lett. **69,** 1260 (1992).

54. D. A. Brawner, A. Schilling, H. R. Ott, R. J. Haug, K. Ploog, and K. von Klitzing, Phys. Rev. Lett. **71,** 785 (1993).

55. S. T. Stoddart, S. J. Bending, A. K. Geim, and M. Henini, Phys. Rev. Lett. **71,** 3854 (1993).

56. T. Tamegai, L. Krusin-Elbaum, P. Santhanam, M. J. Brady, W. T. Masselink, C. Feild, and F. Holtzberg, Phys. Rev. B **45,** 2589 (1992).

57. E. Zeldov, D. Majer, M. Konczykowski, V. B. Geshkenbein, V. M. Vinokur, and H. Shtrikman, Nature **375,** 373 (1995).

58. D. Majer, E. Zeldov, and M. Konczykowski, Phys. Rev. Lett. **75,** 1166 (1995).

59. B. Placais, P. Mathieu, Y. Simon, E. B. Sonin, and K. B. Traito, Phys. Rev. B **54,** 13083 (1996).

60. Y. Abulafia, D. Giller, Y. Wolfus, A. Shaulov, Y. Yeshurun, D. Majer, E. Zeldov, J. L. Peng, and R. L. Greene, J. Appl. Phys. **81,** 4944 (1997).

61. D. Giller, Y. Abulafia, R. Prozorov, Y. Wolfus, A. Shaulov, and Y. Yeshurun, Phys. Rev. B **57,** 14080R (1998).

62. A. A. Polyanskii, X. Y. Cai, D. M. Feldmann, and D. C. Larbalestier, *Visualization of Magnetic Flux in Magnetic Materials and High Temperature Superconductors using the Faraday Effect in Ferrimagnetic Garnet Films*, in Proceedings of "NATO Advanced Research Workshop" (Sozopol, Bulgaria, 1999).

63. V. K. Vlasko-Vlasov *et al.*, in *Physics and Materials Science of Vortex States, Flux Pinning and Dynamics*, edited by R. Kossowski and *et al.*, NATO ASI, Ser. E, Vol. 356 (Kluwer, Kordrecht, 1999), p. 205.

64. R. P. Huebener, *Magnetic flux structures in superconductors* (Springer-Verlag, Berlin, Heidelberg, New-York, 1979).

65. A. A. Polyanskii, V. K. Vlasko-Vlasov, M. V. Indenbom, and V. I. Nikitenko, Sov. Tech. Phys. Lett. **15,** 872 (1989).

66. M. Baziljevich, *Investigation of magnetic flux behavior in $YBa_2Cu_3O_{7-\delta}$ thin films and single crystals using magneto-optic imaging,* Ph. D. Thesis (University of Oslo, Oslo, 1996).

67. Y. Yeshurun, A. P. Malozemoff, and A. Shaulov, Rev. Mod. Phys. **68,** 911 (1996).

68. S. Ooi, T. Shibauchi, and T. Tamegai, Physica C **302,** 339 (1998).

69. S. L. Lee, P. Zimmermann, H. Keller, M. Warden, I. M. Savic, R. Schauwecker, D. Zech, R. Cubitt, E. M. Forgan, P. H. Kes, T. W. Li, A. A. Menovsky, and Z. Tarnawski, Phys. Rev. Lett. **71,** 3862 (1993).

70. B. Khaykovich, M. Konczykowski, E. Zeldov, R. A. Doyle, D. Majer, P. H. Kes, and T. W. Li, Physical Review B-Condensed Matter **56,** R517 (1997).

71. T. W. Clinton *et al*., Physica C **235-240,** 1375 (1994).

72. N. Yamamoto, T. Ishida, K. Okuda, K. Kurahashi, and K. Yamada, Physica C **357,** 298 (2001).

73. E. Zeldov, A. I. Larkin, V. B. Geshkenbein, M. Konczykowski, D. Majer, B. Khaikovich, V. M. Vinokur, and H. Shtrikman, Phys. Rev. Lett. **73,** 1428 (1994).

74. Y. Abulafia, A. Shaulov, Y. Wolfus, R. Prozorov, L. Burlachkov, Y. Yeshurun, D. Majer, E. Zeldov, H. Wuhl, V. B. Geshkenbein, and V. M. Vinokur, Phys. Rev. Lett. **77,** 1596 (1996).

75. K. Deligiannis, P. A. J. de Groot, M. Oussena, S. Pinfold, R. Langan, R. Gagnon, and L. Taillefer, Phys. Rev. Lett. **79,** 2121 (1997).

76. T. Nishizaki, T. Naito, and N. Kobayashi, Phys. Rev. B **58**, 11169 (1998).

77. J. P. Rice and D. M. Ginsberg, J. Cryst. Growth **109,** 432 (1991).

78. A. Schilling, R. A. Fisher, N. E. Phillips, U. Welp, W. K. Kwok, and G. W. Crabtree, Phys. Rev. Let. **78,** 4833 (1997).

79. H. Safar, P. L. Gammel, D. A. Huse, D. J. Bishop, W.C. Lee, and D. M. Ginsberg, Phys. Rev. Lett. **70,** 3800 (1993).

80. H. Safar, P. L. Gammel, D. A. Huse, G. B. Alers, D. J. Bishop, W. C. Lee, J. Giapintzakis, and D. M. Ginsberg, Phys. Rev. B **52,** 6211 (1995).

81. M. Willemin, A. Schilling, H. Keller, C. Rossel, J. Hofer, U. Welp, W. K. Kwok, R. J. Olsson, and G. W. Crabtree, Phys. Rev. Lett. **81,** 4236 (1998).

82. A. I. Ponomarev *et al.*, JETP Lett. **62,** 517 (1995).

83. D. H. Wu *et al*., Phys. Rev. Lett. **70,** 85 (1993).

84. C. Yeh *et al.*, Phys. Rev. B **48,** 9861 (1993).

85. R. Griessen, W. Hai-hu, A. J. J. van Dalen , B. Dam, J. Rector, H. G. Schnack, S. Libbrecht, E. Osquiguil, and Y. Bruynseraede, Phys. Rev. Lett. **72,** 1910 (1994).

86. A. J. J. van Dalen, R. Griessen, S. Libbrecht, Y. Bruynseraede, and E. Osquiguil, Phys. Rev. B **54,** 1366 (1996).

87. M. F. Goffman, J. A. Herbsommer, F. de la Cruz, T. W. Li, and P. H. Kes, Phys. Rev. B **57,** 3663 (1998).

88. D. T. Fuchs, E. Zeldov, T. Tamegai, S. Ooi, M. Rappaport, and H. Shtrikman, Rhys. Rev. Lett. **80,** 4971 (1998).

89. N. Motohira, K. Kuwahara, T. Hasegawa, K. Kishio, and K. Kitazawa, J. Ceram. Soc. Japan **97,** 1009 (1989).

90. M. V. Indenbom, H. Kronmuller, T. W. Li, P. H. Kes, and A. A. Menovsky, Physica C **222,** 203 (1994).

91. M. P. A. Fisher, Phys. Rev. Lett. **62,** 1415 (1989).

92. D. Giller, Y. Abulafia, R. Prozorov, Y. Wolfus, A. Shaulov, Y. Yeshurun, D. Majer, E. Zeldov, J. L. Peng, and R. L. Greene, Physica C **282-287,** 2209 (1997).

93. A. E. Khalil, Phys. Lett. A **246,** 353 (1998).

94. E. H. Brandt, Phys. Rev. B **52,** 15442 (1995).

95. Y. Paltiel, E. Zeldov, Y. N. Myasoedov, H. Shtrikman, S. Bhattacharya, M. J. Higgins, Z. L. Xiao, E. Y. Andrei, P. L. Gammel, and D. J. Bishop, Nature **403,** 398 (2000).

96. L. D. Landau and I. M. Khalatnikov, Dokl. Akad. Nauk SSSR **96,** 469 (1954).

97. R. M. White and T. H. Geballe, *Long range order in solids* (Academic Press, New-York, 1979).

98. P. M. Chaikin and T. C. Lubensky, *Principles of condensed matter physics* (Cambridge University Press, UK, 1997).

99. W. van Saarloos, Phys. Rev. A **37,** 211 (1988).

100. W. van Saarloos, Physics Reports **301,** 9 (1998).

101. W. van Saarloos, Phys. Rev. A **39,** 6367 (1989).

102. P. C. Fife, J. Chem. Phys. **64,** 554 (1976).

103. E. Ben Jacob *et al.*, Physica D **14,** 348 (1985).

104. M. Konczykowski, C. J. van der Beek, S. Colson, M. V. Indenbom, P. H. Kes, Y. Paltiel, and E. Zeldov, Physica C **341,** 1317 (2000).

105. L. Burlachkov, D. Giller, and R. Prozorov, Phys. Rev. B **58**, 15067 (1998).

לסיכום, התוצאות שמובאות בתיזה זאת נותנות היבט חדש על טבען של הפאזות המוצקות של מערבולות ועל מנגנון היווצרותן של פאזות אלה במוליכי על בטמפרטורות גבוהות. במקביל העבודה פותחת אופקים חדשים למחקר עתידי כגון: השפעת הסוגים השונים של אי-סדר על המעבר, איפיון התנאים להיווצרותו של מצב לא מסודר ארעי, השפעת זרם על תהליך הגירעון והגידול של הפאזות המוצקות, ובחינה ניסיונית של התחזיות לגבי הגירעון והגידול בחומרים שונים, טמפרטורות שונות וגאומטריות שונות של דגמים.

ביצענו גם ניסיונות בהם השדה מורד באופן חד מערך שמעל ל-B_{ss} אל ערך שמתחתיו. בניסיונות אלה הפאזה המסודרת מופיעה ליד קצה הדגם מכיוון שבניסיונות אלה שם האינדוקציה היא מינימלית. הפאזה המסודרת גדלה ומתפשטת לכוון מרכז הדגם.

כדי להסביר תוצאות חלוציות אלה פיתחנו תיאוריה המתבססת על משוואת לנדאו-חלטניקוב (LK) לדינמיקה של פרמטר סדר סקלרי. התאוריה שפיתחנו משחזרת את התוצאות הניסיוניות, מנבאת תנאים להיווצרות ויציבות החזית, מתארת את תהליך הגירעון מבחינת מיקומו, סקלות הזמן והמרחב ומתארת את תהליך הגידול – מהירות החזית ורוחבה.

המודל נפתר אנליטית עבור מקרה של גרדיינט שדה קבוע ונומרית עבור מקרה כללי הלוקח בחשבון רלקסציה של מערבולות. מצאנו כי התהליך מתואר היטב ע״י המודל. פיתחנו ביטויים אנליטיים עבור פרמטרים שמתארים את תהליכי הגירעון והגידול של הפאזה המסודרת. הראינו כי עבור יחס הגרדיינט של האינדוקציה ל-B_{ss} גבוה מספיק (כמו ב-BSCCO בטמפרטורות נמוכות), הפאזה המסודרת מופיעה ליד מרכז הדגם (או ליד החזית של מערבולות נכנסות) במקום בו האינדוקציה מינימלית ומתקדמת בצורת חזית אפילו אם ערך האינדוקציה מתאים לאזור הלא יציב (מחוץ לאזור המטאסטבילי) של עקומת האנרגיה החופשית. אם, לעומת זאת, היחס בין הגרדיינט ל-B_{ss} הוא נמוך מספיק (כמו ב-YBCO או ב-BSCCO בטמפרטורות גבוהות) אז הגידול של המצב המסודר הוא הומוגני. אנו גם מנבאים כי הקטנה של גודל הדגם תגרום למעבר מגידול בצורת חזית לגידול הומוגני.

הראינו גם כי החישוב הנומרי שלנו עבור התפתחותן בזמן של עקומות המגנטיזציה מתאר היטב את העקומות הניסיוניות. נתנו הסבר, המבוסס על התיאוריה, לתופעה של ה-״fishtail״ הדינמי: תחילת הגידול (onset) של המגנטיזציה לקראת השיא השני היא השלכה ישירה של קיום שתי הפאזות המוצקות השונות, בעת שדינמיקה של תחילת גידול זו מוכתבת על-ידי דינמיקה של היווצרות הפאזה המסודרת. תחילת הגידול מתקרבת ל-B_{ss} בגבול התרמודינמי.

ההצלחה של משוואת LK בהסבר התוצאות הניסיוניות שלנו מהווה עדות נוספת חזקה לכך, שמקורו של השיא השני האנומלי הוא במעבר פאזה במצב המערבולות ב-BSCCO. יתר על כן, הביטוי האנליטי עבור המהירות של החזית מתאים לתוצאות ניסיוניות של תלות המהירות באינדוקציה אם הערך של המקדם של האיבר הקובי באנרגיה החופשית איננו מתאפס. ממצא זה תומך בטענות על הסדר הראשון של מעבר הפאזה.

מידע נוסף בעל ערך כגון מידע על מנגנון הלכידה. בעקבות עבודה זאת, אומצה גישה דומה על ידי מחברים אחרים לצורך ניתוח של אנומלית השיא השני בחומרים אחרים שלא נחקרו על-ידינו. בדומה למסקנותינו, מחברים אלה הגיעו למסקנה כי האנומליה נגרמת על-ידי מעבר בין הפאזות המוצקות המושרה על-ידי אי-סדר. אנו מסיקים, איפא, כי מעבר הפאזה המושרה על ידי אי-סדר הוא מעבר כללי במוליכי על בטמפרטורות גבוהות והוא הגורם העיקרי לאנומלית השיא השני.

בחלק השני של העבודה אנו מתארים ניסיונות דינמיים שאפשרו, בפעם הראשונה, צפייה ישירה בתהליך ההיווצרות של פאזות המערבולות המוצקות ב-BSCCO, הכולל גירעון וגידול של פאזות אלה. לצורך עבודה זו פיתחנו מערכת מגנטו-אופטית ייחודית בעלת רזולוציה גבוהה בזמן (מסדר גודל של 40 ms) אשר איפשרה לנו לגלות כי קודם לפאזות המוצקות התרמודינמיות, המסודרת והלא מסודרת, נוצרת פאזה לא מסודרת ארעית שמוזרקת לתוך מוליך על כתוצאה מחשיפה פתאומית שלו לשדה החיצוני. לאחר הפעלה של שדה מגנטי חיצוני $B_a \gtrsim B_{ss}$ בנוכחות גרדיינט של שדה מגנטי (שהוא בדרך כלל תלוי בזמן), מופיע מצב ארעי זה, ולאחר פרק זמן קצר מופיע גרעין של פאזה מסודרת ליד מרכז הדגם, שם האינדוקציה מינימלית. הגרעין מתחיל לגדול ולהתקדם בצורה של חזית, כך שנוצר מצב של דו-קיום דינמי בין שתי פאזות מוצקות – מסודרת ולא מסודרת. איפיינו כמותית את התכונות הדינמיות של הפאזות האלה ומצאנו כי הפאזה הלא מסודרת בעלת עוצמת לכידה חזקה הרבה יותר מאשר הפאזה המסודרת. בין היתר אייפינו את $E(j)$ עבור שתי הפאזות, ואת הזרם הקריטי j_c דו-הקיום של שתי הפאזות גורם להיווצרות שבר חד בפרופילים $B(x)$ של האינדוקציה המגנטית. הגבול בין שתי הפאזות (החזית של המצב המסודר) נע במהירות התלויה באינדוקציה B_f שבנקודת הגבול ומתאפסת כאשר $B_f = B_{ss}$. אם השדה המופעל B_a נמוך משדה המעבר B_{ss} אזי הפאזה המסודרת גדלה עד שכל הדגם נכבש על-ידה, והפאזה המסודרת מתעצבת בגבול התרמודינמי. התנהגות שונה מתרחשת עבור $B_a \gtrsim B_{ss}$. במקרה זה ההתרחבות של הפאזה המסודרת נעצרת בנקודה בה האינדוקציה על החזית שווה ל-B_{ss} והגידול של הפאזה הלא מסודרת התרמודינמית ממשיך עד שמצב תרמודינמי זה מתייצב בכל הדגם. דבר זה מתאפיין בשינוי חד בכוון תנועתו של השבר בפרופיל האינדוקציה המגנטית. תופעה זו מאפשרת קביעה מדויקת של ערך השדה B_{ss}.

מצאנו, בנוסף, כי התנהגותו של קו מעבר בין הפאזות המוצקות בטמפרטורות נמוכות ($T < T_{dp}$) מושפעת ממנגנון הלכידה: אם מנגנון הלכידה הוא מסוג δT_c, אז $B_{ss}(T)$ היא פונקציה יורדת, ואם, לעומת זאת, מנגנון הלכידה הוא מסוג δl, אז $B_{ss}(T)$ היא פונקציה עולה. מכאן שההתנהגות של $B_{ss}(T)$ יכולה לשמש לקביעה של סוג מנגנון הלכידה. תוך שימוש בשיטה זו מצאנו כי מנגנון הלכידה ב-NCCO ו-Pb-BSCCO הוא δT_c, בעוד שב-YBCO מנגנון הלכידה הוא δl.

כמו כן, מצאנו כי על מנת לתאר את התלות של B_{ss} בטמפרטורה ב-Pb-BSCCO, חייבים להביא בחשבון מעברים בין שלושה אופני לכידה שונים המוגדרים על ידי היחס בין שלוש סקלות האורך האופייניות: ($L_c < s < L_0$), ($s < L_c < L$), ($s < L_0 < L_c$), כאשר s הוא המרחק בין שכבות מוליכות-העל בחומר, L_c הוא אורך אופייני של קטע לכוד של מערבולת, ו-L_0 הוא אורך אופייני לפלוקטואציות של פלקסון הנובעות מהאינטרקציות האלסטיות. מעברים בין אופנים אלה ב-Pb-BSCCO מתרחשים עקב האניזוטרופיה והטמפרטורה הקריטית הגבוהות יחסית.

בנוסף, בחנו לעומק את ישימות המודל ב-YBCO ע"י בדיקת התחזית שלו לגבי הערכים של $B_{ss}(0)$ ו- T_{dp}. למרות שלא ניתן לקבל ערכים של גדלים אלה באופן ישיר מכיוון שהם תלויים בפרמטר בלתי ידוע – הקריטריון של לינדמן c_L – ניתן לבדוק התחזית עבור יחס בין ערכים של גדלים אלה עבור שני דגמים עם חוזק לכידה שונה. השווינו בין שני דגמים מאותו גידול גבישי ומצאנו ערך ניסיוני של 1.25 מול ערך תיאורטי של 1.14 עבור היחס ב-T_{dp} וערך ניסיוני של 0.64 מול ערך תיאורטי של 0.5 עבור היחס ב- B_{ss}. תוצאות אלה נותנות, איפא, חיזוק נוסף לישימות של המודל.

לסיכום חלק זה של העבודה ניתן להגיד כי במסגרת העבודה האנומליה של ה"שיא השני" נחקרה במגוון של חומרים מוליכי על בטמפרטורות גבוהות. החומרים שנבחרו (NCCO, YBCO, Pb-BSCCO) היו בעלי טמפרטורה קריטית ואניזוטרופיה בתחומים שונים. מדידות m $vs.$ H, m $vs.$ T, ו-m $vs.$ t בכל החומרים שנחקרו תומכות בקיומו של מעבר הפאזה בין שתי הפאזות המוצקות. למרות שהתלות בטמפרטורה של קווי מעבר הפאזה בחומרים השונים שונה איכותית, הצלחנו לתאר אותה בעזרת אותו מודל, מודל של מעבר המושרה ע"י אי-סדר.

עבודה זאת הראתה כיצד ניתן לישם את מודל המעבר המושרה על ידי אי-סדר לניתוח של התנהגות קווי המעבר בין הפאזות המוצקות בחומרים שונים וכיצד ניתן לנצל ניתוח זה לקבלת

ביצענו גם מדידות של מגנטיזציה כתלות בזמן ($m\ vs.\ t$). מדידות אלה תומכות גם הן בקיומו של מעבר הפאזה. המידע החשוב הנוסף שלמדנו ממדידות אלה נוגע לטיבו של שדה B_p: בכל החומרים ניתן ליחס שדה זה למעבר במנגנון ה"זחילה" של מערבולות ממנגנון אלסטי למנגנון פלסטי. מעבר זה מציין הופעה של חוסר סדר הקשור להופעת דיסלוקציות במבנה המערבולות שמתגבר ככל שהשדה עולה.

בדומה ל-YBCO, השבר בעקומות $m\ vs.\ T$ מופיע גם ב-NCCO בתחום השדות בהם נמצא B_{on}. אולם בניגוד ל-YBCO עבורו השבר ב-$m\ vs.\ T$ חופף ל-שבר ב- $m\ vs.\ H$, עבור NCCO מיקומו של שבר זה בדיאגרמת הפאזות (B,T) לא חופף למיקומו של B_{on}. הבדל זה מוסבר בעבודה זו כנובע מהתנהגות שונה של קו המעבר בין הפזות המוצקות: יורד עם טמפרטורה ב-NCCO ועולה עם טמפרטורה ב-YBCO.

בניתוח התאורטי של התוצאות מצאנו כי למרות ההבדלים האיכותיים בתלות של שדה מעבר הפאזה B_{ss} בטמפרטורה ב-NCCO, YBCO ו- Pb-BSCCO, תלות זו יכולה להיות מתוארת ע"י אותו מודל - מודל של מעבר המושרה ע"י אי-סדר. המודל הזה מתאר את דיאגרמת הפאזות של מערבולות מגנטיות כנוצרת מתחרות בין שלוש סקלות אנרגיה: אנרגיה אלסטית, אנרגית לכידה, ואנרגיה תרמית. המעבר בין הפאזה המוצקה המסודרת לבין הפאזה הנוזלית מתרחש כאשר האנרגיה האלסטית משתווה לאנרגיה התרמית בעוד שהמעבר בין שתי הפאזות המוצקות מתרחש כאשר האנרגיה האלסטית משתווה לאנרגית הלכידה. הראינו כי על מנת להסביר את ההתנהגויות השונות של $B_{ss}(T)$ המודל הזה צריך להיות מיושם באופנים שונים לחומרים שונים. ב-NCCO, לדוגמא, אנו מוצאים כי בגלל הטמפרטורה הקריטית הנמוכה שלו ניתן להתמקד בתחרות בין האנרגיה האלסטית לאנרגית לכידה בלבד תוך הזנחת האנרגיה התרמית ברוב תחום הטמפרטורות (עובדה זאת גורמת, בין היתר, לאי-קיומו של מעבר פאזה בין הפאזה המסודרת לפאזה הנוזלית ב-NCCO). אם כן התלות של B_{ss} בטמפרטורה נקבעת ע"י התלות בטמפרטורה של אורך הקורלאציה ξ. בניגוד ל-NCCO, לחישוב עקומות $B_{ss}(T)$ של Pb-BSCCO ו- YBCO יש לקחת בחשבון פלוקטואציות תרמיות בטמפרטורות הגבוהות מטמפרטורה של שחרור מלכידה T_{dp}. עבור $T > T_{dp}$, אורך הקורלאציה של לרקין גדל מעריכית עם הטמפרטורה מה שגורם להאצה בירידה של אנרגית הלכידה. עובדה זו משתקפת בהתנהגותו של קו $B_{ss}(T)$ בתור גידול פתאומי המתחיל ב- $T = T_{dp}$.

בביצוע שני חלקי המחקר השתמשנו בשתי טכניקות מדידה מגנטיות לוקאליות המבוססות על מדידות של אפקט Hall במערך של חיישנים זעירים ועל מדידות של אפקט פארדיי במערכת מגנטו-אופטית. טכניקות אלה מאפשרות מיפוי של התפלגות האינדוקציה המגנטית על פני הדגם ברזולוציה מרחבית של מיקרונים. לטכניקות אלה יתרון מובהק במדידות של המצב הבלתי-הדיר של מוליכי-על בו האינדוקציה המגנטית לא אחידה. השימוש במערכי חיישני Hall מתאים למדידות בהן יש דרישה לרגישות גבוהה ועבודה בשדות גבוהים. השתמשנו בהם בחלק הראשון של התיזה לצורך חקירת מעבר הפאזה בחומרים השונים ואפיון דינמי של הפאזות קרוב לשווי משקל.

העוצמה של הטכניקה המגנטו-אופטית מתגלה בחקירת תהליך היווצרותן של הפאזות המוצקות. בחקירה זו השתמשנו במערכת מגנטו-אופטית שנבנתה במסגרת עבודה זו. יתרונה של המערכת הם כושר ההפרדה הגבוה בזמן ובמרחב המאפשר גילוי ומעקב אחר דו-קיום דינאמי בין שתי פאזות. תוצאות חלוציות אלה נתנו לנו מוטיבציה לפיתוח של תיאוריה חדשה המתבססת על פתרונות אנליטיים ונומריים של משוואת לנדאו-חלטניקוב המתארת את דינמיקת פרמטר הסדר.

המדידות של מגנטיזציה כתלות בשדה (m $vs.$ H) ב-$Nd_{1.85}Ce_{0.15}CuO_{4-d}$ (NCCO), $YBa_2Cu_3O_{7-d}$ (YBCO), ו-$Bi_{1.6}Pb_{0.4}Sr_2CaCu_2O_{8+d}$ (Pb-BSCCO) מגלות גידול אנומלי של העקומות בדומה לשיא השני ב-BSCCO באינדוקציה לוקאלית B_{on}. מדידות אלה מגלות גם, לראשונה, שבר בולט בעקומות מגנטיזציה (m $vs.$ H) ב-YBCO. המיקום של שבר זה, $B_k(T)$, על דיאגרמת הפאזות (B,T) של YBCO חופף למיקומו של שבר חד אחר בעקומות המגנטיזציה כתלות בטמפרטורה (m $vs.$ T) - השבר בעקומות m $vs.$ T מתגלה בדיוק בתחום השדות בו נמצא B_k. השדה B_k אינו זז עם הזמן בניגוד לשדה אופייני אחר B_p, השדה של השיא השני. B_k מאופיין גם כן במינימום של קצב הרלקסציה של מערבולות. מצאנו בנוסף כי ניתן לכייל את עקומות המגנטיזציה שנמדדו בטמפרטורות שונות ע"י גורמי כיול מתאימים, אולם לשדות הנמוכים מ-B_k ולשדות הגבוהים ממנו דרוש כיול שונה. גם עובדה זו תומכת בקיום שתי פאזות שונות מתחת ומעל לשדה זה. התכונות של השדה B_k שנמנו לעיל הן הסיבה לכך שבעבודה זו זיהינו שדה זה בתור המעבר בין הפאזות המוצקות ב-YBCO.

תקציר

התחום של מוליכות-על שנחשב כמעט סגור, נפתח מחדש לאחר הגילוי של מוליכי-על בטמפרטורות גבוהות. אחד הנושאים המעניינים ביותר של התחום המחודש הזה הוא דיאגרמת הפזות העשירה של מבנה המערבולות המגנטיות. הערך היותר קטן של אורך הקורלאציה ξ בהשוואה למוליכי-העל הקונבנציונליים, והערך היותר גדול של אורך החדירה λ ושל האניזוטרופיה $1/\varepsilon$, גורמים למערך המערבולות להיות רך יותר ופחות לכוד במוליכי-על בטמפרטורות גבוהות, וכתוצאה מכך לדיאגרמת פזות מורכבת. כדוגמא ניתן לראות את דיאגרמת הפזות המגנטית של $Bi_2Sr_2CaCu_2O_{8+\delta}$ (BSCCO). תוצאות של מדידות מגנטיות, מדידות mSR ומדידות של פיזור נויטרונים בחומר זה מראות כי קיימות לפחות שלוש פזות של מערבולות מגנטיות: פאזה מוצקה מסודרת (או כמעט מסודרת), פאזה מוצקה *לא* מסודרת ופאזה נוזלית. להבדיל ממעבר פאזה בין מוצק מסודר לנוזל אשר מתאפיין במדידות מגנטיות ע"י קפיצה חדה במגנטיזציה ההדירה, המעבר בין הפאזה המוצקה המסודרת לפאזה המוצקה הלא מסודרת מתאפיין בהתרחבות חדה של עקומת המגנטיזציה *הלא*-הדירה. התרחבות אנומלית זו נקראת "השיא השני" או "fishtail". התנהגות דומה נצפתה גם במדידות של חומרים אחרים. אך הצורה השונה, החדות והמיקום השונים של השיא השני הביאו להסברים שונים שלו בחומרים השונים.

בחלק הראשון של תיזה זו נעשה ניסיון למצוא מקור משותף להופעת השיא השני בחומרים השונים. מדדנו את אנומלית השיא השני ב-$YBa_2Cu_3O_{7-d}$, $Nd_{1.85}Ce_{0.15}CuO_{4-d}$, ו-$Bi_{1.6}Pb_{0.4}Sr_2CaCu_2O_{8+d}$. נבחנה האפשרות להסביר את האנומליה בתור מעבר פאזה שבין הפאזה המסודרת לפזה הלא מסודרת בדומה לזה שמתרחש ב-BSCCO. על מנת להגשים מטרה זו בחנו עדויות לקיום מעבר הפאזה בחומרים השונים וקבענו את מיקומו האפשרי. מצאנו תאור כמותי של קו מעבר הפאזה, $B_{ss}(T)$, בחומרים השונים בעזרת המודל של המעבר המושרה ע"י אי-סדר ודנו בהבדלים בצורות קווי המעבר על ידי ההבדלים בערכים של הפרמטרים המאפיינים את מוליך העל בחומרים השונים.

בחלק השני של התיזה מתואר מחקר חלוצי, ניסיוני ותאורטי, של תהליך היווצרות הפאזות המוצקות.

<u>תוכן העניינים</u>

עבודה זאת נעשתה בהדרכתו של

פרופסור יוסף ישורון

מן המחלקה לפיסיקה של אוניברסיטת בר-אילן

מעבר פאזה המושרה על ידי אי-סדר במערכת מערבולות מגנטיות במוליכי-על בטמפרטורות גבוהות

חיבור לשם קבלת תואר "דוקטור לפילוסופיה"

מאת

דמיטרי גילר

המחלקה לפיסיקה

הוגש לסינט של אוניברסיטת בר-אילן

רמת-גן אדר, ה'תשס"ב